UNIVERSITY OF OKLAHOMA

GRADUATE COLLEGE

METAL OXIDE NANOPARTICLES: WETTABILITY MODIFICATION FOR EMULSION STABILIZATION AND ELECTROSTATICALLY INDUCED GELATION

A DISSERTATION

SUBMITTED TO THE GRADUATE FACULTY

in partial fulfillment of the requirements for the

Degree of

DOCTOR OF PHILOSOPHY

By

JAVEN S. WESTON
Norman, Oklahoma
2015

Downloaded from SHAREOK. Persistent Handle URL: https://hdl.handle.net/11244/14586

METAL OXIDE NANOPARTICLES: WETTABILITY MODIFICATION FOR EMULSION STABILIZATION AND ELECTROSTATICALLY INDUCED GELATION

A DISSERTATION APPROVED FOR THE
SCHOOL OF CHEMICAL, BIOLOGICAL AND MATERIALS ENGINEERING

BY

_____
Dr. Jeffrey H. Harwell, Chair

_____
Dr. Daniel E. Resasco

_____
Dr. Brian P. Grady

_____
Dr. Steven P. Crossley

_____
Dr. Bor-Jier (Ben) Shiau

© Copyright by JAVEN S. WESTON 2015
All Rights Reserved.

The author would like to dedicate this work to all of the family and friends who supported him. My mother and father gave me the confidence and freedom to pursue my dreams. My brothers gave me my first managerial experience and kept me grounded. My grandparents gave me four extraordinary examples of how to live. My committee gave me their expertise and their time above and beyond any reasonable expectation. My friends gave me the laughter I needed to get through long nights in the lab. And, my wife gave me everything I could have ever asked for and more than I deserved. Thank you all.

ACKNOWLEDGEMENTS

The author thanks the Department of Energy (DOE/EPSCOR) program for funding this work (Grant DE-SC0004600). The author would also like to thank the NIST Center for Neutron Research and Boualem Hammouda for their assistance and grant of beam time on the NG-7 SANS instrument as a part of Proposal #19373, as well as ORNL's Spallation Neutron Source and Christopher Stanley for additional beam time, assistance, and expertise pertaining to the BL-6 EQ-SANS instrument and Proposal #11255. Finally, the author would like to thank Rolf Jentoft, Nicholas Briggs, Danielle Baker, Prapas Lohateeraparp, Laura Wesson, Bruce Roberts, and the many, many others who helped him throughout this research.

TABLE OF CONTENTS

Acknowledgements iv

Table of Contents v

List of Tables vii

List of Figures ix

Abstract xv

Chapter 1: Introduction 1

Chapter 2: Silica Nanoparticle Wettability: Characterization and Effects on Emulsion Properties 3

Introduction 3

Experimental 6

Materials 6

Methods 6

Results And Discussion 14

Capillary Rise Method 14

Sessile Drop Analysis 16

Heat Of Immersion 17

Comparing Wetting Methods And Results 18

Emulsification And Droplet Size 20

Conclusions 25

Chapter 3: Phase Behavior and Pseudo-solid, Shear-thinning Gel Formation in Binary Dispersions of Fumed Metal Oxide Nanoparticles at Low Volume Fractions 27

Introduction 27

Experimental 31

Materials 31

Methods 32

Results And Discussion 35
Gelation Phase Behavior 35
Structural Studies of the Gel Network 39
Conclusions 45
Chapter 4: Rheological characterization Of Pseudo-solid, Shear-thinning Gels from Binary Dispersion of Fumed Metal Oxide Nanoparticles at Low Volume Fractions 47
Introduction 47
Experimental 51
Materials 51
Methods 52
Results and Discussion 54
Yield Stress 56
Shear Moduli 59
Apparent Viscosity 61
Conclusions 65
Chapter 5: Small Angle Neutron Scattering of Pseudo-solid, Shear-thinning Binary Mixtures of Fumed Metal Oxide Nanoparticles at Low Volume Fractions 67
Introduction 67
Experimental 68
Materials 68
Methods 70
Results and Discussion 72
Conclusions 85
References 87
Appendix I: Gel Centrifugation Studies 96
Appendix II: Total system charge and gelation 99

LIST OF TABLES

Table 1. Desired and actual silane surface coverages for the particles used in this study. 9

Table 2. Capillary rise or Washburn method results for all tested nanoparticles containing calculated water contact angles and liquid uptake rates of both hexane and water. 15

Table 3. Heats of immersion and calculated water contact angles of surface-modified silica nanoparticles measured using microcalorimetry 18

Table 4. Emulsion properties and droplet sizes for 50-50 decane-water emulsions stabilized by a variety of surface-modified silica nanoparticles initially dispersed in the aqueous phase. 21

Table 5. Emulsion properties and droplet sizes for 50-50 decane-water emulsions stabilized by a variety of surface-modified silica nanoparticles initially dispersed in the oil phase. 23

Table 6. Mean particle size and zeta potential of 1.5 vol% 70:30 binary mixture of Aerosil 200:Aeroxide AluC dispersions. 44

Table 7. Yield stress values for gels made with various particle mixtures, ratios, and concentrations. Values were determined by taking the average yield stress of a series of five stress ramp experiments 57

Table 8. Ostwald-de Waele and Herschel-Bulkley power law fitting parameters for particle dispersions and colloidal gels, including pre-exponential consistencies, power-law indices, and shear rates where shear-thinning behavior transitions to Newtonian shear-rate independence. 63

Table 9. Unified Power Law fitting results for radius of gyration (Rg) and fractal dimension parameters for all scattering data presented in this study. P1 is the fractal dimension of the 'soft' microagglomerates, Rg2/P2 are the corresponding parameters for

the ‘hard’ nanoaggregates, and Rg3/P3 are the corresponding parameters for the spherical primary particle scattering, respectively. 81

LIST OF FIGURES

Figure 1. Illustration of apparatus used to measure powder wettability via the capillary rise method. 11

Figure 2. Example of typical particle wetting curve for capillary rise in a bed of modified silica nanoparticles 14

Figure 3. Two images illustrating the complete wetting observed with some nanoparticle-coated glass slides taken (a.) immediately prior to droplet deposition and (b.) immediately after droplet deposition, and an electron micrograph (c.) showing a portion of the surface of a nanoparticle-coated glass slide. 16

Figure 4. Droplet size distributions for emulsions stabilized with Ludox colloidal silica nanoparticles initially dispersed in the water phase that have been surface-modified with a.) phenyl trichlorosilane, b.) trimethyl chlorosilane, and c.) octadecyl trichlorosilane at two different surface coverages. The mean droplet size is larger for all emulsions stabilized by the low surface coverage particles when compared to the emulsions stabilized by the low surface coverage particles. Also note that all emulsions stabilized by low surface coverage nanoparticles are decane-in-water, while all emulsions stabilized by high surface coverage nanoparticles are water-in-decane. 20

Figure 5. Emulsion droplet size distributions for Pickering emulsions stabilized by nanoparticles modified with various alkyl chlorosilanes at two different surface coverages and particles being initially dispersed in aqueous solution..... 22

Figure 6. Droplet size distributions for emulsions stabilized with Ludox colloidal silica nanoparticles that have been surface-modified with a.) phenyl trichlorosilane, b.) trimethyl chlorosilane, and c.) octadecyl trichlorosilane at two different surface coverages. The mean droplet size is larger for emulsions stabilized by the high surface coverage particles when compared to the emulsions stabilized by the low surface

coverage particles for PhTCS- and TMCS-modified particles, while the opposite is true for the OTCS-modified particles. 23

Figure 7. Emulsion droplet size distributions for Pickering emulsions stabilized by nanoparticles modified with various alkyl chlorosilanes at two different surface coverages. 24

Figure 8. Images illustrating the gels' pseudo-solid behavior under gravity (a & b) and shear-thinning behavior observed when the gel is mildly perturbed by vibrational forces exceeding the gel's yield stress. 36

Figure 9. Representative images showing the significant transition from low-viscosity fluid to pseudo-solid gel, and vice versa, observed when crossing the gel region's pH boundary. Samples shown have a total particle concentration of 2.0 vol% and are a 70-30 mixture of Aerosil 200-Aeroxide Alu C. Pictures were taken after 1 min of inversion; pH adjustments were made using 10 wt% solutions of HCl and NaOH. 37

Figure 10. Phase behavior diagrams for various binary mixtures of fumed metal oxide nanoparticles in deionized water. X's indicate gel formation, O's indicate low-viscosity suspensions, and /'s indicate mild viscosity increases. Both silica/ alumina mixtures (a&b) experience gelation in a pH range between 4 and 10 with the gel region shifting to higher pH range as Si/ Al ratio decreases. Silica/ titania mixtures (c&e) show gelation between pH's 4 and 7, and alumina/ titania mixtures show gelation between 7 and 9. For different alumina and titania particles tested, the particles with smaller primary particle size (Alu130, Ti P90) were more effective for gel formation. 38

Figure 11. TEM micrographs illustrating areas of low particle density, containing dispersed nanoparticle aggregates of a variety of sizes with empty void spaces between them (a-c), and a series of micrographs showing a region of unbroken nanoparticle networks that extend for 10's of microns in all directions, at three different levels of magnification. Images are of ~100 nm thick sections of a 1.5 vol% 30-70 AluC-Aerosil

200 dispersions in polymerized LR White resin. Circles in background are from TEM grid..... 40

Figure 12. Small-angle x-ray scattering (SAXS) attenuation spectra illustrating the structural morphologies of the SiO_2 and Al_2O_3 in DI water and LR white..... 41

Figure 13. Optical microscope images for samples inside and outside the gel region: (a.)1.5 vol%, 30-70 AluC-Aerosil 200, pH = 7 and (b.) 1.5 vol%, 30-70 AluC-Aerosil 200, pH = 2..... 42

Figure 14. Measured attenuation spectra for the non-gel and gel samples (a. and b respectively), particle size distributions (c.) and ζ-potential (d.) of 1.5 vol% 30–70 Aerosil 200–Aeroxide Alu C dispersions at various pH values. The samples at pH 4, 6, 7, and 8 are gels, while the pH 2 and 10 samples are outside the gel region..... 43

Figure 15. Representative plots of viscosity vs. shear-rate (a), viscosity vs. shear stress (b), and shear modulus vs. strain (c) for gels made of oppositely charged, fumed metal oxide nanoparticles dispersed in deionized water. Results shown here are for a gel with a 75-25 mixture of Aerosil 200 (silica)-Aeroxide Alu C (alumina), a total particle concentration of 2.0 vol%, and a solution pH of 7. The gel behaves as a power-law fluid over the tested shear rate range, has a yield stress of ≈150 Pa, and behaves as a linear viscoelastic solid for strains < 2-3%. Open symbols in (a) were measured using the SR-5000, closed symbols were measured using the Merlin II. Closed symbols in (c.) represent the storage modulus (G') and open symbols represent the loss modulus (G"). 55

Figure 16. Typical stress-strain data from a yield stress test for silica-alumina gels at various particle volume fractions..... 56

Figure 17. Shear modulus vs frequency plots for silica-alumina (a-b), silica-titania (c-d), and titania-alumina (e-f) gels at various particle concentrations and ratios. Closed

symbols represent the storage modulus (G') and open symbols represent the loss modulus (G"). 59

Figure 18. Apparent viscosity vs shear rate plots for silica-alumina (a-c), silica-titania (d-f), and titania-alumina (g-i) dispersions at various particle concentrations, particle ratios, and solution pHs. 62

Figure 19. Normalized viscosity vs shear rate plot (a) and consistency vs max. +/- pairings plot (b) for all gels that exhibit yield stress behavior. Viscosities were normalized using the fitted consistency value found in Table 8. 64

Figure 20. Illustration demonstrating the two possible gelation mechanisms in electrostatically-driven heteroaggregation gels. Fig. 1a. displays a gel network generated via heteroaggregation of microagglomerates and Fig. 1b. displays a network generated via heteroaggregation of fully dispersed nanoaggregates. In this illustration blue and red are used to indicate aggregates and agglomerates of silica and alumina, respectively.. 73

Figure 21. Scattering curves for dispersions of Aerosil 200 at the alumina contrast match point and Aeroxide AluC at the silica contrast match point. Best fit lines for a Unified Power Law model are shown for each curve. 75

Figure 22. Scattering profiles of the overall gel structure for two Aerosil 200:Aeroxide AluC dispersions at the particle ratio and pH where gel strength is maximized. One sample is below the critical gelation concentration, the other is above the gelation concentration and exhibits a yield stress. Fractal dimensions obtained through fitting the data to a Unified Power Law model are displayed, and the solid lines illustrate the best fit line of the model..... 76

Figure 23. Scattering curves for contrast-matched gels at a series of total particle concentrations and a constant particle ratio and solution pH of 75:25 Si200:AluC and 6.5, respectively. Figs. 3a. and b. contain data taken from gels suspended at the alumina

contrast match point and silica contrast match point, respectively. Best fit lines for a Unified Power Law model are shown for each curve. 78

Figure 24. Scattering curves as a function of particle ratio (a. & b.) and solution pH (c. & d.) with all other parameters held constant. Figs. 4a. & c. contain data taken from gels suspended at the alumina contrast match point and Figs. 4b. & d. contain data taken from gels suspended at the silica contrast match point. Best fit lines for a Unified Power Law model are shown for each curve. 82

Figure 25. Model nanoaggregates of Aeroxide AluC and Aerosil 200 with the correct fractal dimension, primary particle size, and hydrodynamic radius. Alumina particles and silica particles are colored red and blue, respectively. (Particles in figure were resized to fit illustration and are not displayed at a constant relative scale.) 83

Figure 26. Illustrations of the gel networks generated using NetLogo, VESTA, and Packmol software (a.-c.) along with a high-resolution TEM micrograph (d.) and EDS elemental map (e.). Blue and red are used to indicate that the particle is Aerosil 200 and Aeroxide AluC, respectively. 84

Figure 27. Method used to study gel stability against sedimentation 96

Figure 28. Centrifuge stability results for Aerosil 200:Aeroxide AluC gels at 1.5 vol% (a.), 2.0 vol% (b.), and 2.5 vol% (c.) total particle concentrations at three different silica/alumina ratios. A combined plot containing all of the data is also shown (d.). All %'s reflect vol%. 97

Figure 29. Centrifuge stability results for gels consisting of Aerosil 150:Aeroxide AluC (a.) and Aerosil 200:Aeroxide Alu130 (b.) mixtures. 98

Figure 30. Total surface charge curves for Aerosil 200:Aeroxide AluC mixtures at various particle ratios and solution pHs. 100

Figure 31. Comparison of experimentally determined phase behavior diagram for Aerosil 200:Aeroxide AluC gel mixtures and a magnified view of the TSC chart shown in Figure 30. 100

ABSTRACT

Mixtures of fumed metal oxide nanoparticles (np's) dispersed in water, at a solution pH where one species is positively charged and the other is negatively charged, form pseudo-solid gels at volume fractions as low as 1.5 vol %. The nanoparticles consist of spherical primary particles that have been sintered into rigid, fractal aggregates. When the two particle species are mixed at a range of volume fractions, they heteroaggregate to form a percolated, fluid-spanning structure due to electrostatic interactions. These gels exhibit a measurable yield stress and an apparent viscosity that follows a power law relationship with shear rate. This work characterizes the rheological properties, physical structure, and phase behavior for binary mixtures of fumed silica, fumed alumina, and fumed titania in aqueous dispersions. Gels were characterized at various particle concentrations, solution pHs, and mixture ratios. The strength of the gel network, as evaluated by the storage modulus and yield stress, appears to be maximized when the total negative surface charge on one type of particle is closely matched to the total positive surface charge on the opposite particle type.

Secondly, recent interest in the use of nanoparticles in emulsion stabilization has driven increased efforts to understand how the characteristics of the particles influence emulsion properties. While it is clear that contact angle and wettability must play significant roles in determining the type of emulsion formed, it is not straightforward to measure the contact angle of a nanoparticle. In this paper we compare multiple techniques for characterizing the water-air contact angle of silica nanoparticles while systematically varying the hydrophobicity of the nanoparticles using silanization. We then compare the performance of the particles in decane/water emulsions. While the heat of immersion measured by microcalorimetry is found to provide the best method for discriminating between the wettability of the particles, the fraction of surface covered by the silane groups was observed to affect the structure of the emulsion more profoundly

than the differences in the contact angles of the particles. Furthermore, we find that the phase of initial dispersion is extremely influential in determining the resulting emultion type and droplet size.

Keywords – nanoparticles, wettability, silica, silanization, heat of immersion, contact angle, Pickering emulsions, heteroaggregation, fumed nanoparticles, yield stress, power law fluid, gel rheology, hydrogel, small angle scattering, fractal network

CHAPTER 1: INTRODUCTION

The following work was completed within the Center for Interfacial Reaction Engineering (CIRE), a collaborative research center at the University of Oklahoma, Oklahoma State University and the University of Tulsa. CIRE has four central research thrusts: 1) Synthesizing and characterizing nanoparticles that optimize the reactivity, emulsion stability, mass transfer, and interfacial area of phase-transfer catalysis processes; 2) Understanding how catalytic reaction mechanisms and kinetics change when the reactions take place at a liquid-liquid interface; 3) Using spectroscopy and molecular modeling to understand the reaction pathways, competitive adsorption, and thermodynamics of model reactions on interfacial catalysts; 4) Combining experimentation, theory, and modeling to understand the kinetics of mass transfer and phase equilibrium in dynamic, phase-transfer environments and how altering particle properties can be used to optimize phase transfer. Metal oxide nanoparticles are widely used in a variety of commercial industries, are relatively cheap, stable up to high temperatures, and their size/shape can be precisely controlled using a variety of synthesis techniques. All of these characteristics make them ideal to act as interfacially-active catalyst supports in the phase-selective reactions that are at the heart of CIRE's research mission. The results that follow fall under the first of CIRE's research thrusts and investigate two primary phenomena: 1) how altering metal oxide nanoparticles with hydrophobic and hydrophilic surface modifiers affects their ability to stabilize Pickering emulsions in order to understand how the type surface modifier used affects the characteristics of the emulsion formed, and 2) how oppositely charged metal oxide nanoparticles self-assemble in aqueous dispersions in order to gain insights into how charged nanoparticles may interact when adsorbed at liquid-liquid interfaces and to

explore the interesting rheological properties of the colloidal gels formed via electrostatic heteroaggregation of the different nanoparticle species.

The following four chapters have either been published in or will be submitted for publication in peer-reviewed journals, and are presented here as verbatim replications of their published forms.

CHAPTER 2: SILICA NANOPARTICLE WETTABILITY: CHARACTERIZATION AND EFFECTS ON EMULSION PROPERTIES

INTRODUCTION

Silanization has been extensively used to modify the wettability of metal oxide nanoparticles, soil sediments, clays, and zeolites.[1-6] The process uses chloro- or methoxy-silanes to attack the surface hydroxyls of the metal oxides, creating a M-O-Si-R bond that covalently attaches the silane to the metal oxide surface. Using alkyl silanes as the surface modifier can drastically alter the wettability of the metal oxide surface by replacing hydrophilic hydroxyl groups with hydrophobic hydrocarbon chains. At low surface coverages, these alkyl silanes have been shown to cluster together into patches rather than distribute homogenously across the surface, while it is still possible to form a complete, continuous monolayer at higher surface coverages.[7] Silicate nanoparticles with hydrophobic surface modifications have been shown to work very effectively as emulsion stabilizers,[8] absorbents for cleaning up hydrocarbon contaminants in surface/ground water,[9] and catalysts/catalyst supports with improved stability in the presence of hot water[10] and increased reaction rates due to decreased water adsorption capacity.[11] Others have used silanization to attach hydrophilic surface moieties onto the metal oxide surface, such as carboxylic acids,[12] aminos,[13] phosphates,[14] and sulfonates/sulfonic acids.[15] Hydrophilically modified nanoparticles have been used to create pH-responsive, particle-stabilized foams,[16] create pH-sensitive gates for controlling drug delivery,[17] and improve low-temperature CO_2-capture sorbents.[18] Silanes that have been covalently attached to the metal oxide surface can also provide excellent anchor points for block co-polymers and other molecules, which can be used to increase particle dispersion in dispersions and coatings,[19,20] create nanoparticle chelating agents for extraction of metal ions from ground water,[21] produce pH-responsive Pickering emulsions using different

hydrophilic polymers,[22] and generate nanoparticles that can exhibit both hydrophobic and hydrophilic surface properties, depending on the polarity of the surrounding fluid.[23] The numerous applications for surface-modified metal oxide nanoparticles and the importance of wettability to most of these applications makes the accurate characterization of the nanoparticle's wettability particularly important. Grigoriev,[24] Nowak,[25] and others have compared various methods of measuring nanoparticle and powder wettability and contact angle, and enumerated the pros and cons of each method. One common method involves measuring the amount of time for a known volume of particles to sink into a fluid after being placed at the air/fluid interface, taking advantage of how particle contact angle strongly affects the floatation characteristics of powders. However, when using this method it is difficult to compare particles that have different densities, surface areas, particle sizes, shapes, or any other difference that could also affect the floatation time of the powder. Numerous techniques for characterizing the particle contact angle by direct observation of the trapped particle at the fluid-fluid interface have been developed,[26-28] but these methods all suffer from problems relating to either the magnification limits of optical microscopy or the addition of gelation agents to one or both fluids that could potentially affect the location of the particles at the interface, especially in the case of nanoparticles where very small particle displacements would result in large changes in the observed contact angle. Ellipsometry is another technique that is very useful for determining particle contact angle in a large variety of situations, but, as pointed out by Binks,[29] the technique suffers from poor sensitivity when the interfacial coverage deviates very far above or below that of a close-packed monolayer.

One of the most popular methods involves analysis of static and dynamic sessile liquid drops in contact with either a thin film of particles on a substrate[30] or a compressed pellet of particles.[31] This method assumes that the particles form a smooth, flat, non-porous

surface as required by the Young-Laplace equation, an assumption that is inherently false with a deposited layer or compressed pellet of particles. The sessile drop method also ignores that mechanical compression can significantly alter particle surface chemistry, with previous studies showing that the observed contact angle decreases as compaction pressure increases.[32,33]

The capillary rise or Washburn method measures the rate of penetration of a liquid into a packed bed of particles and relates the rate to the particle/liquid contact angle. This method either requires that the particle bed be well characterized in terms of effective capillary diameter, average pore size/shape, pore tortuosity, etc. or that the particle packing be estimated by using a reference liquid that 'perfectly' wets the particles (usually a hydrocarbon with a low surface tension and minimal viscosity). Determining the former parameters is very difficult for nanoparticle systems and using a reference liquid does not work well when the contact angle of the test liquid(s) are close to zero degrees. The porosimetry-style method of measuring contact angle developed by Forny[34] addresses most of the issues related to the capillary rise method, but requires the use of a high-pressure pump and a high-pressure microcalorimeter. The thin-layer wicking and particle-coated Wilhelmy plate methods suffer from both the non-uniformity of coating/packing and smooth surface assumption problems related to the static and dynamic sessile drop methods.

Modern microcalorimetry instruments allow for the accurate measurement of the heat of immersion for small particles, which can be thermodynamically related to the particle contact angle.[35] However, the heat of immersion method also has flaws, namely, that converting enthalpy of immersion to contact angle requires a series of assumptions and that incomplete wetting of highly hydrophobic particles by water and vice versa requires the use of an extrapolation method. In summary, all of the methods of measuring particle contact angle currently in common use have a series of drawbacks and complications.

This study uses a combination of three different methods to determine the wettability of silica nanoparticles that have been treated with a variety of surface-modifiers in order to compare the advantages and disadvantages of each of the different wettability characterization techniques. These three particular techniques were chosen for five reasons: their general popularity in the literature, their ability to characterize a wide range of contact angles, the ease of measurement, the availability of equipment to complete the measurements, and the familiarity of the authors with the individual techniques. It also examines how different types of surface modifiers affect particle wettability at differing surface coverages, including the effect on droplet sizes and distributions in decane/water Pickering emulsions.

EXPERIMENTAL

MATERIALS

Ludox TM-50 colloidal silica was purchased from Sigma-Aldrich; it is a 50.0±1.0 wt% aqueous dispersion of spherical colloidal silica nanoparticles with an average diameter of 32 nm, a specific surface area of 110-150 m^2/g, and a solution pH of 8.5-9.5. Mercaptopropyl trimethoxysilane (MPTMS), trimethyl chlorosilane (TMCS), phenyl trichlorosilane (PhTCS), and octadecyl trichlorosilane (OTCS) were all purchased from Sigma Aldrich. Hydrogen peroxide was purchased as a 30 wt% aqueous solution from Fisher Scientific. Sodium hydroxide was purchased as solid pellets from Fisher Scientific. Hexane was obtained from Acros Organics at 99%, reagent-grade purity. Isopropyl alcohol was obtained from VWR International. Deionized water with a conductivity of < 2 μS/cm was obtained using a polymer ion-exchange filtration system.

METHODS

The silica nanoparticles must be removed from aqueous solution prior to silanization because chlorosilanes will react violently with water, preventing effective surface treatment. Therefore, the Ludox TM-50 colloidal silica nanoparticles were removed from

aqueous dispersion via evaporation of the liquid water in a fume hood, and washed to remove excess sodium hydroxide: the dry nanoparticles were repeatedly dispersed in deionized water via vortex mixing, centrifuged out of the dispersion at 7000 rpm, and the clear supernatant solution was removed. These steps were repeated until the supernatant solution had a conductivity of ≤75 μS/cm. Then the nanoparticles were washed an additional two times with a 70/30 (v/v) mixture of isopropyl alcohol and deionized water and dried at 120°C in a vacuum oven for 24hrs.

Silanization of the nanoparticles was carried out by first dispersing 10g of dried/washed Ludox in 100mL of toluene by sonication with a horn sonicator with a 1" stainless steel probe at 70% amplitude for 12 minutes. A known amount of silane agent was then added to the particle dispersion and allowed to react with the silica surface for 12 hours while being stirred with a magnetic stir bar at 35°C. After reaction with the silane, the particles were removed from solution via centrifugation, and washed five times with isopropyl alcohol to remove excess silane/toluene and twice with a 70/30 (v/v) mixture of isopropyl alcohol and deionized water, with a centrifugation/supernatant removal step between each wash. The nanoparticles were then dried for 24 hours in a vacuum oven at 120°C. The extent of surface modification was controlled by changing the amount of silane added during the reaction step, under the assumption that almost all of the silanes reacted with the silica surface as long as the number of silane molecules being grafted onto the surface was significantly less than the total number of surface hydroxyls, a reasonable assumption based on literature sources.[36,37,38] However, the degree of surface coverage was also determined independently after modification using temperature-programmed oxidation (TPO). The nanoparticles were modified with two different concentrations of silane, in the desire to obtain two different surface coverages, 1 μmol/m² and 2 μmol/m², based on BET-style surface area measurements showing that the dried and washed Ludox TM-50

nanoparticles had a specific surface area of 115 m^2/g. Silica nanoparticles generally have 2-3 surface hydroxyls per square nanometer;[39,40] implying that these surface coverages correlate to reacting 20-30% and 40-50% of the silica's surface hydroxyls, respectively. The nanoparticles silanized with MPTMS were then further modified into superhydrophilic silica nanoparticles using the technique described by Oh et al,[15] which oxidizes the thiol group of the MPTMS by dispersing the particles in a solution of 30 wt% H_2O_2 and stirring the solution at 24 hours at room temperature, resulting in sulfonic acid groups on the silica surface. The particles were then washed several times with water and dried. The sulfonic acid groups were then converted into sodium sulfonate by dispering the particles in a 0.1M solution of NaOH under continuous stirring for 24 hours. The particles were then washed and dried in a vacuum oven for 24 hours at 120°C. These particles are hereafter referred to as sulfonic acid/sulfonate propyl trimethoxysilane (SAPTMS) modified particles. After silanization and vacuum drying, the particles are a freely flowing powder and do not need to be further processed (grinding, ball-milling, etc.) prior to characterization or emulsification.

The level of surface coverage was determined using a TPO method where a known quantity of the sample is added to a quartz capillary tube and placed in a high temperature oven. Then, a mixture of O_2 and He is made to flow through the capillary tube and the oven heats the sample to 800°C at a rate of 10°C/min, oxidizing any carbon on the sample into CO and CO_2. The gases then flow into a reactor where they diffuse through a Ni catalyst bed with H_2, causing the CO/CO_2 to undergo a methanation reaction. The methanated gases are then fed into a flame ionization detector (FID) which

Table 1. Desired and actual silane surface coverages for the particles used in this study.

Functional Group	Desired Surface Coverage, µmol/m^2	Actual Surface Coverage, µmol/m^2
Phenyl	1.00	0.56
Phenyl	2.00	1.00
Trimethyl	1.00	0.89
Trimethyl	2.00	1.83
Octadecyl	1.00	0.72
Octadecyl	2.00	1.46

measures the concentration of methane in the stream. The FID signal is then integrated and the peak area is used to determine the amount of carbon on the nanoparticle surface through comparison to the peak area generated by injecting a known quantity of CO_2 into the methanator. Once the total amount of carbon on the surface is known, the molar surface coverage can be determined by dividing the number of moles of carbon measured by the number of carbon molecules in each of the silane modifiers (6 moles of carbon per molecule for PhTCS, 18 moles for OTCS, etc.). Table 1 contains the desired and actual levels of surface coverage observed for the PhTCS-, TMCS-, and OTCS-modified nanoparticles used in this work (the MPTMS/SAPTMS-modified nanoparticles were not characterized due to the potential damage to the methanation catalyst by sulfur poisoning). It can be seen that while the actual amount of surface coverage measured deviates from the desired level of surface coverage the ratio of surface coverages are quite close to the desired 2:1. Overall, the TMCS and OTCS modifiers appeared to provide surface coverages relatively close to the estimated/desired surface coverage, while the PhTCS only provided ~50% of the desired coverage. For the remainder of the text, samples created with a desired coverage of roughly 1 µmol/m^2 will be referred to as 'low' surface coverage particles, while samples created with a desired coverage of roughly 2 µmol/m^2 will be referred to as 'high' surface coverage particles.

The capillary rise or Washburn method of determining particle wettability and contact angle relates the rate of a liquid's rise into a packed bed of powder particles. This method uses an equation based on Poiseuille's law for liquid flow through a capillary. The Washburn method assumes that the porous bed of particles behaves like a bundle of cylindrical capillaries with a constant diameter. The resulting equation relating capillary rise to particle contact angle is:

$$\frac{m^2}{t} = C\frac{\rho^2\gamma_l cos\theta}{2\mu} \qquad \text{(Eqn. 1)}$$

Where m^2/t is the uptake rate of mass^2 as the liquid rises into the particle bed, c is an experimentally-determined geometric packing factor, ρ is the liquid density, γ_l is the surface tension of the liquid, θ is the particle-liquid contact angle, and μ is the liquid viscosity.[41] The geometric packing factor is usually determined for each type of particle/packing by using a liquid that completely wets the sample; usually pentane, hexane, octane, etc. due to their low viscosity and low surface tension.[5] This reference liquid is assumed to have a contact angle of 0°, which allows one to determine the packing constant, if the other liquid properties are known; the reference liquid used here was hexane, due to its low viscosity and minimal surface tension at room temperature. It should be noted that better wetting (lower contact angle) may not produce a greater mass uptake rate when the liquids have large differences in viscosity, surface tension, and/or density, as is the case between hexane and water. Fig. 1 contains an illustration of the experimental set up used to measure particle contact angle in this study, consisting of a 1 cm diameter glass cylinder that has been sealed on one end by a glass frit to provide a consistent base to begin packing the powder and keep the powder from falling out of the cell. The cell is packed with the sample using a device which applies a consistent packing pressure to ensure that the mass and height of the packed sample is similar from experiment to experiment. After packing, the cell is suspended from a cantilever arm that

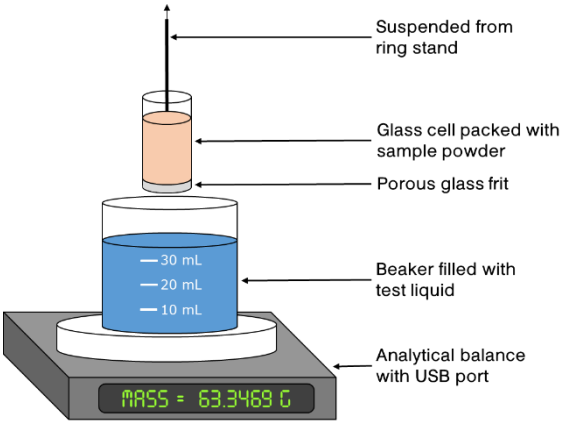


Figure 1. Illustration of apparatus used to measure powder wettability via the capillary rise method.

is attached to a ring stand and positioned above a beaker of the test liquid that rests on an analytical balance that is connected to a computer with data acquisition software. The mass of the beaker of liquid is measured for 200 s in order to calculate an accurate measurement of the liquid evaporation rate, which is later used to normalize the measured mass uptake to correct for liquid evaporation. After 200 s, the sample cell is lowered into the liquid to a known depth using the cantilever arm. The mass of liquid remaining in the beaker is then measured for an additional 600 s or until the sample cell has been saturated with liquid, whichever occurs first. The data is corrected for evaporative losses and plotted as m^2 (mass uptake of liquid into powder)^2 vs time, the slope of the linear portion of this plot then provides the m^2/t term used in Eqn. 1, and can be used to calculate the solid material constant, c, for the reference liquid or the contact angle for other liquids. At least two experiments were completed for each set of solid-liquid pairings to ensure that consistent results were obtained.

Sessile drops of water were analyzed with an Attension Theta optical tensiometer manufactured by Biolin Scientific. For the solid surface, glass slides were coated with a layer of nanoparticles using the procedure described by Dove[42] and Shang,[43] where 2-3 mL of a 1.0 wt% dispersion of nanoparticles in isopropyl alcohol are placed on a 76 x 26 x 1.2 mm glass slide and allowed to dry in a vacuum oven at 120°C for 12 hours to remove the alcohol and adsorbed water; each slide was kept in the vacuum oven until immediately prior to the experiments. The static contact angle was measured by placing an 8 μL droplet of water on the surface of the nanoparticle-coated slide. A droplet volume

of 8 μL was chosen because, at that volume, the capillary length of the droplet is larger than the droplet diameter, making the effect of gravity on the drop shape negligible. Each measurement was repeated at least three times and the average calculated.

A Setaram C80 microcalorimeter with a specially designed pair of powder cells was used to measure the heat of immersion for all of the modified nanoparticles. The heat of immersion is related to the particle contact angle using the theoretical approach described by Yan.[29] The method uses the enthalpy of immersion, a result of the change in Gibbs free energy that results from replacing a solid-gas interface with a solid-liquid interface, and relates it to the solid-liquid contact angle using the Young-Laplace equation. The resulting contact angle equation yields:

$$cos\theta = \frac{-KT - h_i - \pi_e}{\gamma_{lv}} \qquad \text{(Eqn. 2)}$$

Where θ is the solid-liquid contact angle, K is the difference between the temperature dependence of solid-liquid interfacial tension and solid surface tension, T is the absolute temperature, h_i is the enthalpy of immersion, γ_{lv} is the liquid-vapor surface tension, and π_e is the difference between the solid surface tension and the solid-vapor surface tension ($\gamma_s - \gamma_{sv}$), which is assumed to be negligible for systems with reasonably large contact angles. In this case, K is assumed to be $7.0 \cdot 10^{-5}$ J/m²·K, corresponding to a low-energy surface and a γ_{sl} that is temperature independent, following the assumptions made by Yan. The powder cells consist of a stainless steel cylinder and a pair of brass sealing rings that hold a membrane in place and seal each end of the cell; one cell is used as the sample cell, while the other is used as a reference cell. The calorimeter cells are designed by Setaram with a breaking rod that has been modified in-house with a sharp, pointed tip which is used to puncture the powder cell's membrane. Prior to each experiment the modified nanoparticles are dried in a vacuum oven at 120°C for at least 12 hours. Then, a known quantity of sample is placed into each powder cell, and the cell is sealed with a

nitrile rubber membrane. Both powder cells are then placed in the larger stainless steel, calorimetry cells (manufactured by Setaram) with approximately 8 mL of the wetting liquid. Both calorimeter cells are then installed into the microcalorimeter and allowed to equilibrate at 40°C. After the heat signal and cell temperatures stabilize, both membranes of the sample cell are punctured with the breaking rod, allowing the liquid to enter the cell and immerse the nanoparticles. The thermal energy released or absorbed by the sample immersion is then measured and recorded by the microcalorimeter. A series of eight blank punctures of sealed, empty powder cells were used to estimate the heat released by only puncturing the nitrile rubber membranes and subtracted from the measured immersion enthalpy as a constant background. The heat of immersion is measured at least four times for each sample and the average was used to calculate the particle contact angle.

Emulsions were made in two different ways to study how the phase of initial particle dispersion affected droplet size and emulsion type. Emulsions were made by dispersing 200 mg of nanoparticles in 10 mL of water/decane by horn sonicating the samples using a 1/8" probe at 25% amplitude for 7 minutes. Then, 10 mL of decane/water was added to the sample vial and the mixture was sonicated using the same settings for 20 minutes with the probe's tip approx. 2 mm below the oil/water interface. The resulting emulsions were allowed to separate and equilibrate for 24 hours and the phase ratios were determined by visually measuring the height of each phase using a micrometer. Emulsion type (oil-in-water or water-in-oil) was determined by placing a droplet of the emulsion phase into a beaker of deionized water; if the emulsion phase dispersed in the water it was assumed to be oil-in-water, and vice versa. The droplet size was determined using light microscopy and Image J image processing software. Droplet size distributions were created by measuring the droplet size of a minimum of 250 individual droplets from a total of 5 separate microscopy images.

RESULTS AND DISCUSSION

CAPILLARY RISE METHOD

Figure 2 shows a representative example of an evaporation-corrected particle wetting curve used to estimate particle contact angle via the capillary rise method. The curve is a plot of the evaporation-corrected squared mass uptake rate vs. time, and the m^2/t term in Eqn. 1 is found by calculating the slope of the curve in the linear region of the curve, indicated by the gray line. The disturbance at ~ 60s is due to the introduction of the capillary cell, which must break the surface tension and displace some of the liquid. Table 2 contains the results of capillary rise measurements for all of the modified nanoparticles. These measurements indicate that the unmodified Ludox particles have the lowest calculated contact angle with water while the nanoparticles modified with OTCS at the higher level of surface coverage have the highest calculated contact angle. The contact angles of the remaining nanoparticles vary largely as expected if one assumes that the water solubility of the surface modifier should be an accurate predictor of the 'wettability' of a surface coated with that modifier, with the exception of the SAPTMS-modified nanoparticles. The PhTCS-coated particles are least hydrophobic, followed by the TMCS-coated particles, with the OTCS-coated particles being the most hydrophobic.

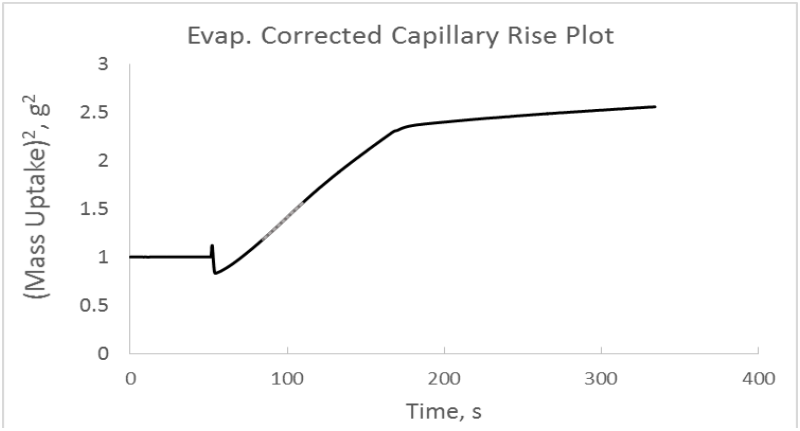


Figure 2. Example of typical particle wetting curve for capillary rise in a bed of modified silica nanoparticles

Table 2. Capillary rise or Washburn method results for all tested nanoparticles containing calculated water contact angles and liquid uptake rates of both hexane and water.

Sample	Contact Angle, Washburn	Hexane Uptake Rate, g^2/s	H_2O Uptake Rate, g^2/s	H_2O/Hex Uptake Rate Ratio
Bare Ludox	66	2.3E-03	2.5E-03	1.11
Low Coverage SAPTMS	73	1.0E-01	7.9E-02	0.78
High Coverage SAPTMS	73	1.2E-01	9.6E-02	0.78
Low Coverage PhTCS	69	5.0E-02	4.9E-02	0.99
High Coverage PhTCS	79	4.0E-02	2.1E-02	0.52
Low Coverage TMCS	85	6.0E-03	1.3E-03	0.22
High Coverage TMCS	87	5.9E-03	8.2E-04	0.14
Low Coverage OTCS	85	2.0E-03	4.8E-04	0.24
High Coverage OTCS	90	8.7E-04	5.4E-06	0.01

The uptake rate (mass^2/time) of the unmodified (bare) Ludox particles was measured six times with a standard deviation of 16%, and a similar degree of uncertainty is assumed to be present for the other nanoparticle samples, but due to the difficulty of synthesizing the particles in large batches and concerns about batch-to-batch reproducibility, each batch of nanoparticles was measured using the capillary rise method only twice with hexane and twice with deionized water to ensure consistency, but the sample population of two is too small to justify calculating a standard deviation.

Table 2 illustrates many of the problems related to measuring wettability of nanoparticles with the capillary rise method. The first problem involves determining the material packing factor using a reference liquid with a contact angle of zero degrees. All of the particles shown in Table 2 were created using the same silica nanoparticles and therefore should pack in an approximately similar manner, and subsequently be wet at the same rate by a reference liquid that 'perfectly' wets the particle surfaces. Nonetheless, a more than two order of magnitude variation in the hexane uptake rate was found, indicating that the particle contact angle with hexane varies to a similar degree and implying that hexane does not 'perfectly' wet all of the nanoparticles. In particular, we can observe that uptake rates of both hexane and deionized water are much larger for the

SAPTMS-modified nanoparticles than for any of the other types of particles, implying very strong surface-liquid interactions for these particles. Additionally, the capillary rise method cannot result in a contact angle > 90° because all of the parameters in Eqn. 1 are positive except for cosθ. Furthermore, in order to measure a contact angle of 90° the mass uptake rate must be equal to 0 g^2/s. Hence, as the measured contact angle approaches 90°, the capillary rise method will begin to significantly underestimate the particle contact angle, which is likely the case with all of the contact angle measurements for the TMCS- and OTCS-modified nanoparticles.

SESSILE DROP ANALYSIS

Results for the modified nanoparticles are summarized in Table 3, which shows the static contact angle for water calculated using the Attension Theta software and fitting the drop shape with a Young-Laplace contact angle model. Contact angles were only able to be determined for the high surface coverage PhTCS-modified particles, both batches of TMCS-modified particles, and both batches of OTCS-modified particles, because the water droplet completely wet and soaked-into the nanoparticle layer on the glass slides for the other nanoparticle batches. Fig. 3a.-b. contains images illustrating complete wetting of a nanoparticle-coated slide with a water droplet as observed with the glass slides coated with unmodified Ludox, both batches of SAPTMS-modified Ludox, and the low surface coverage PhTCS-modified Ludox; the two images are taken one

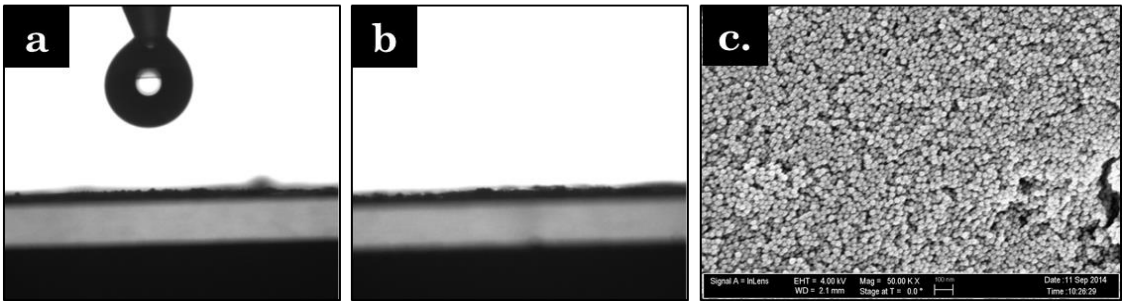


Figure 3. Two images illustrating the complete wetting observed with some nanoparticle-coated glass slides taken (a.) immediately prior to droplet deposition and (b.) immediately after droplet deposition, and an electron micrograph (c.) showing a portion of the surface of a nanoparticle-coated glass slide.

second apart from each other, where a. is immediately prior to the droplet being deposited on the surface and b. is immediately after the droplet has been deposited on the surface. Fig. 3c contains a scanning electron micrograph of the surface of a nanoparticle-coated glass slide, showing that the nanoparticles fully cover the surface of the glass slide in a continuous layer. The nanoparticle layer is relatively smooth, but it still has noticeable roughness and porosity that could alter the observed contact angle even if the nanoparticles are hydrophobic enough to prevent the droplet from soaking into the particle layer. These results illustrate a major problem with the sessile drop method of measuring wettability; it is very difficult to get accurate contact angle measurements for particles with a low contact angle because of the inherent porosity of a compressed pellet or deposited layer of particles. The nanoparticle contact angles shown in Table 3 largely follow the same trends observed in the capillary rise tests, with the PhTCS-modified nanoparticles being more hydrophilic than the TMCS-modified nanoparticles which are, in turn, more hydrophilic than the OTCS-modified nanoparticles and the particles with higher surface coverage of the alkyl chlorosilanes are more hydrophobic than those with the lower degree of surface coverage.

HEAT OF IMMERSION

Table 4 contains the heats of immersion and calculated water contact angles[29] for all of the modified nanoparticles tested. Similar to the sessile drop results, we do calculate contact angles of less than zero degrees when using the heat of immersion method, but unlike the sessile drop results, we are still able to quantify the differences in wettability between the nanoparticles by comparing immersion enthalpies. Namely, the SAPTMS-modified particles have a noticeable more exothermic heat of immersion when compared to the unmodified silica nanoparticles, indicating that the low surface coverage SAPTMS-modified particles are more hydrophilic than the unmodified Ludox and the high surface coverage SAPTMS-modified particles are even more hydrophilic,

Table 3. Heats of immersion and calculated water contact angles of surface-modified silica nanoparticles measured using microcalorimetry

Sample	Heat of Immersion, mJ/m^2	Contact Angle
Bare Ludox	-110.2 ± 6.7	<0
Low Coverage SAPTMS	-135.5 ± 28.8	<0
High Coverage SAPTMS	-170.1 ± 23.9	<0
Low Coverage MPTMS	-60.2 ± 2.6	58
High Coverage MPTMS	-65.8 ± 16.4	53
Low Coverage PhTCS	-65.8 ± 5.1	52
High Coverage PhTCS	-47.5 ± 3.3	69
Low Coverage TMCS	-5.1 ± 7.3	104
High Coverage TMCS	1.9 ± 3.9	109
Low Coverage OTCS	-0.4 ± 7.9	107
High Coverage OTCS	13.0 ± 2.1	120

with an enthalpy of immersion of -170.1 mJ/m^2. The enthalpy of immersion data also reinforces the order of hydrophobicity found with the previous methods, with the type of alkyl group appearing to be more dominant in determining particle wettability than the amount of surface coverage. The two different values of enthalpy of immersion for unmodified Ludox illustrate the importance of completely drying the nanoparticles prior to placing them in the sealed powder cell, with the enthalpy of immersion of air dried Ludox being less than 1/3 of the enthalpy of immersion measured for Ludox dried at 120°C in a vacuum oven. Finally, Table 4 also confirms the hydrophilizing effect of oxidizing and ionizing the MPTMS-modified nanoparticles, as the enthalpies of immersion became 75.3 and 104.4 mJ/m^2 more exothermic for the low and high surface coverage samples, respectively.

COMPARING WETTING METHODS AND RESULTS

Overall, the heat of immersion method of quantifying contact angle provided the largest range of quantifiable contact angles, the most reliable measurements of surface interactions between the silica nanoparticles and water, and the greatest ability to distinguish the differences between highly hydrophilic nanoparticles. Heat of immersion measurements also require only a small amount of sample for each measurement (~500 mg or ~50 m^2 of total particle surface area are required to achieve a high degree of precision), which provides a significant advantage in comparison to the capillary rise

cells used here. Theoretically, smaller capillary rise cells could be manufactured that required smaller amounts of sample, but these possibilities are limited because of increasing liquid-cell interactions as the capillary cell's diameter decreases; in the limit, wall effects would come to dominate the capillary rise of the fluid.

While the capillary rise method does have issues regarding picking the best reference liquid, it is a very simple and useful technique for particles that are easily wet by the test liquid, because the liquid droplet is likely to penetrate into a porous pellet or particle layer during the sessile drop method.

The heat of immersion method of measuring contact angle does encounter problems when trying to characterize very hydrophobic particles, which do not easily immerse in water and therefore may not be completely wetted in the test cell; this observation may be represented in our results in underestimation of the true contact angle of the very hydrophobic OTCS-modified particles. In these cases, it may be better to use the sessile drop method with static or dynamic drops, which is much better at quantifying contact angles for very hydrophobic particles, but fails once the contact angle becomes small enough for the droplet to penetrate into the porous pellet or layer of nanoparticles.

Comparing the results for the three different characterization methods contained in Tables 2-4, it can be seen that, while the calculated contact angles measured for each type of nanoparticle change drastically from one characterization method to another, all measurement methods show a relatively consistent trend in the hierarchy of particle hydrophobicity with the type of surface group being a much more dominant indicator of particle wettability than the degree of surface coverages, at least for the surface coverages measured.

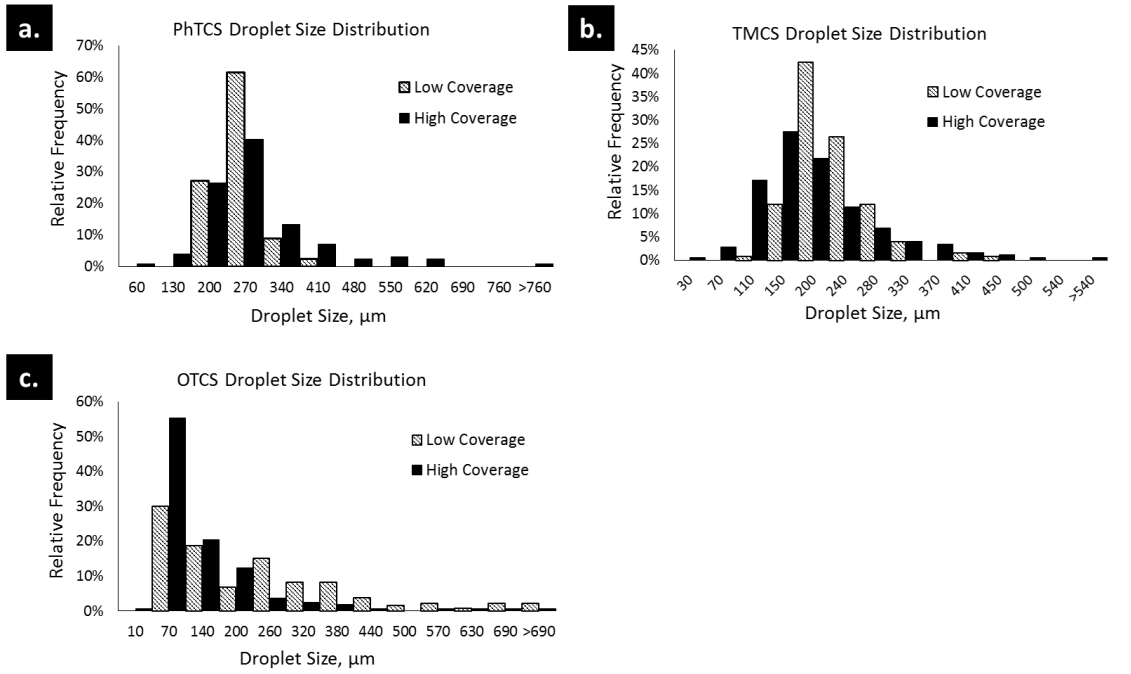


Figure 4. Droplet size distributions for emulsions stabilized with Ludox colloidal silica nanoparticles initially dispersed in the water phase that have been surface-modified with a.) phenyl trichlorosilane, b.) trimethyl chlorosilane, and c.) octadecyl trichlorosilane at two different surface coverages. The mean droplet size is larger for all emulsions stabilized by the low surface coverage particles when compared to the emulsions stabilized by the low surface coverage particles. Also note that all emulsions stabilized by low surface coverage nanoparticles are decane-in-water, while all emulsions stabilized by high surface coverage nanoparticles are water-in-decane.

EMULSIFICATION AND DROPLET SIZE

Silane-modified silica nanoparticles were used to stabilize decane and water emulsions; all of the nanoparticles were able to stabilize significant emulsion fractions except for the bare Ludox and SAPTMS-modified Ludox, which could only form small volumes of unstable emulsion droplets, with these particles largely remaining dispersed in the aqueous phase. Binks and Lumsdon[44] have shown that the initial location of nanoparticles has a strong influence on the type of Pickering emulsion formed. Therefore, two sets of emulsions were characterized, one with the particles initially dispersed in the aqueous phase and another with the particles initially dispersed in the oil phase. Binks and Lumsdon found that dispersing the particles in one phase resulted in a bias to form emulsions with that phase as the continuous phase. It was theorized that the relatively large size and mass of the nanoparticles limits their ability to quickly

diffuse into their preferred phase and rearrange at the interface; two things that molecular surfactants can do quite readily.

Table 4 contains all of the measured properties for emulsions created after initially dispersing the nanoparticles in deionized water (emulsion type, phase volumes, and mean droplet diameter). The emulsion type observed was entirely dependent on the amount of surface coverage rather than a function of the previously measured particle contact angles. This implies that the number of unreacted surface hydroxyls on the silica surface may play a relatively large role in determining the emulsion type in comparison to the type of alkyl group or even observed particle contact angle, at least for particles that have not had their regions of hydrophobicity/hydrophilicity controlled, as in Janus-style particles. The apparent importance of surface coverage relative to the type of functional group could be explained by strong adsorption of water on the remaining hydroxyl groups on the particle surface. The adsorbed water could potentially alter the overall particle wetting behavior or the surface heterogeneities could result in pinned contact lines that alter how the particles adsorb at the interface.[45] There does not appear to be any discernible trend in emulsion fraction as a function of surface coverage, alkyl group, or emulsion type, though there is a notable decrease in the excess water phase and corresponding increase in excess decane phase for both emulsions stabilized with OTCS-modified silica. Figure 4 contains three histograms showing the droplet size

Table 4. Emulsion properties and droplet sizes for 50-50 decane-water emulsions stabilized by a variety of surface-modified silica nanoparticles initially dispersed in the aqueous phase.

Initially Dispersed in Aqueous Solution					
Particle Type	**Emulsion Type**	**Excess Decane Fraction**	**Emulsion Fraction**	**Excess Water Fraction**	**Droplet Diameter, μm**
Low Coverage PhTCS	**O/W**	0.13	0.62	0.25	223±42
High Coverage PhTCS	**W/O**	0.15	0.50	0.35	251±116
Low Coverage TMCS	**O/W**	0.15	0.45	0.40	203±52
High Coverage TMCS	**W/O**	0.12	0.55	0.38	179±86
Low Coverage OTCS	**O/W**	0.45	0.55	0.00	204±185
High Coverage OTCS	**W/O**	0.40	0.60	0.00	109±110

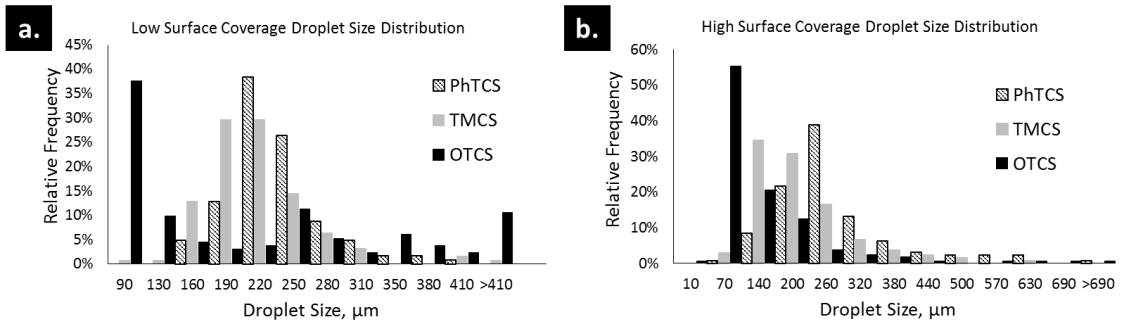


Figure 5. Emulsion droplet size distributions for Pickering emulsions stabilized by nanoparticles modified with various alkyl chlorosilanes at two different surface coverages and particles being initially dispersed in aqueous solution.

distribution for all of the characterized Pickering emulsions. These histograms show that the mean droplet size is larger for all emulsions stabilized by the high surface coverage particles in comparison to emulsions stabilized by the low surface coverage particles. Figure 5 contains two histograms that show how the emulsion droplet size distribution changes as a function of the type of alkyl group for both of the tested levels of surface coverage. Here, we see a consistent trend for both levels of surface coverage, where the mean droplet diameter decreases with increasing particle contact angle, i.e. PhTCS-modified silica-stabilized emulsion droplets are larger than TMCS-modified silica-stabilized emulsion droplets which are larger than OTCS-modified silica-stabilized emulsion droplets. This agrees with results reported by Binks[38] where it was shown that droplet diameter is large for emulsions stabilized by very hydrophilic nanoparticles, and then decreases with increasing contact angle up to a certain critical particle

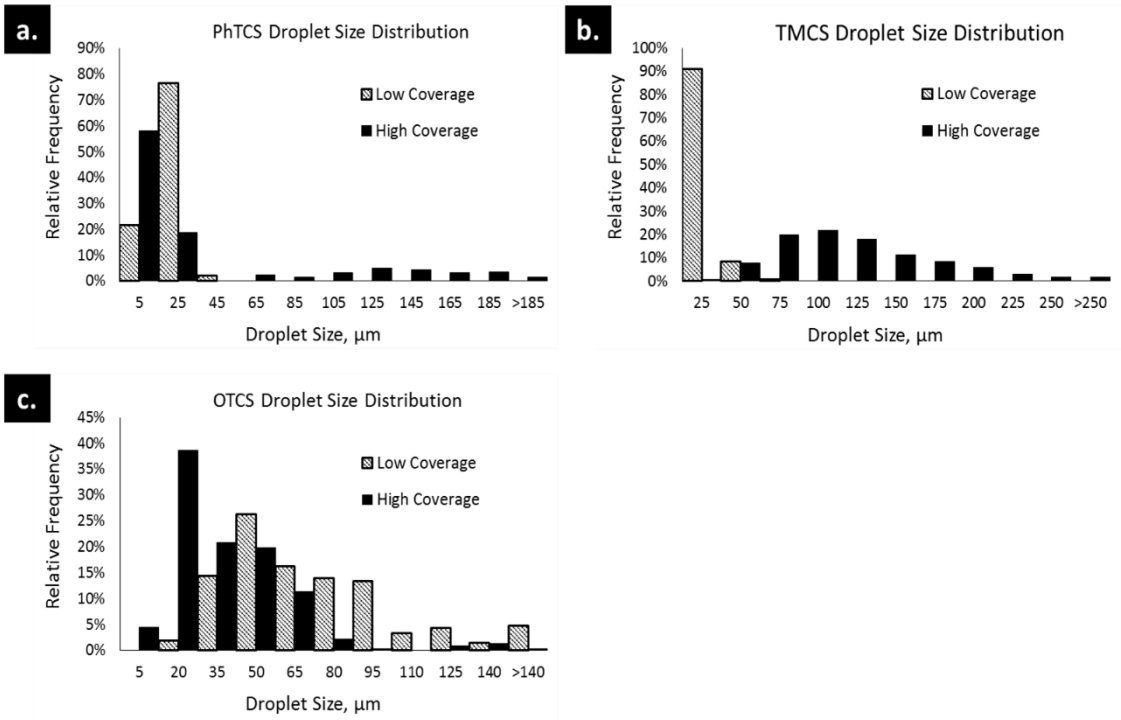


Figure 6. Droplet size distributions for emulsions stabilized with Ludox colloidal silica nanoparticles that have been surface-modified with a.) phenyl trichlorosilane, b.) trimethyl chlorosilane, and c.) octadecyl trichlorosilane at two different surface coverages. The mean droplet size is larger for emulsions stabilized by the high surface coverage particles when compared to the emulsions stabilized by the low surface coverage particles for PhTCS- and TMCS-modified particles, while the opposite is true for the OTCS-modified particles.

hydrophobicity, where the droplet size begins to increase again as the particles become extremely hydrophobic.

Table 5 contains all of the measured properties for emulsions created after initially dispersing the nanoparticles in decane. Similar to the previous results with

Table 5. Emulsion properties and droplet sizes for 50-50 decane-water emulsions stabilized by a variety of surface-modified silica nanoparticles initially dispersed in the oil phase.

Initially Dispersed in Oil Solution					
Particle Type	**Emulsion Type**	**Excess Decane Fraction**	**Emulsion Fraction**	**Excess Water Fraction**	**Average Droplet Diameter, µm**
Low Coverage PhTCS	**O/W**	0.34	0.32	0.34	8±5
High Coverage PhTCS	**W/O**	0.09	0.46	0.45	34±56
Low Coverage TMCS	**O/W**	0.16	0.55	0.29	15±8
High Coverage TMCS	**W/O**	0.09	0.57	0.34	110±56
Low Coverage OTCS	**W/O**	0.36	0.23	0.41	65±35
High Coverage OTCS	**W/O**	0.41	0.23	0.36	30±25

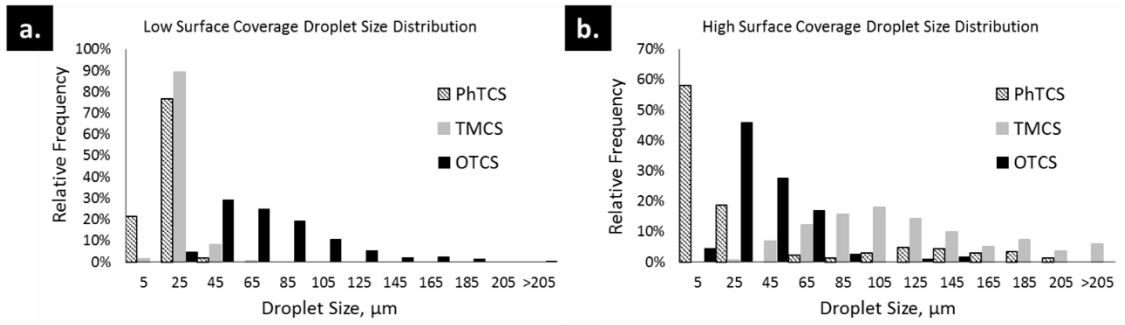


Figure 7. Emulsion droplet size distributions for Pickering emulsions stabilized by nanoparticles modified with various alkyl chlorosilanes at two different surface coverages.

water-dispersed particles, the emulsion type observed was largely dependent on the amount of surface coverage rather than the measured particle contact angles, except in the case of the low surface coverage OTCS particles, which formed an O/W emulsion when initially dispersed in water, but a W/O emulsion when initially dispersed in decane. This provides further evidence that the number of water-hydroxyl interactions may be quite high and a major factor in determining emulsion type. Again, no distinct trends appear in the emulsion fraction as a function of any of the tested variables. Average droplet sizes for oil-dispersed particles are an order of magnitude smaller than the droplets observed for the emulsions made from aqueously-dispersed particles.

Figure 6 contains three histograms showing the droplet size distribution for all of the characterized Pickering emulsions. These histograms show that the mean droplet size is larger for emulsions stabilized by the high surface coverage particles in comparison to emulsions stabilized by the low surface coverage particles for PhTCS- and TMCS-modified particles, while the reverse is true for emulsions stabilized with OTCS-modified particles. Figure 7 contains two histograms that show how the emulsion droplet size distribution changes as a function of the type of alkyl group for both of the tested levels of surface coverage. Here, we see almost the complete opposite of the trend observed with the water-dispersed emulsions, with the PhTCS-modified (most hydrophilic) particles stabilizing the smallest droplets and the more hydrophobic particles stabilizing larger emulsion droplets. Two of Binks' prior findings: 1) particles that are too

hydrophobic or too hydrophilic tend to stabilize large emulsion droplets, while particles with a more intermediate hydrophobicity produce smaller emulsion droplets; 2) initially dispersing particles in water/oil renders them more hydrophilic/hydrophobic, may help explain the behavior seen in Figures 5 and 7; initial dispersal in water leaves the more hydrophobic particles (OTCS-modified) at the optimum hydrophobicity to stabilize small droplets while initial dispersal in the decane leaves the more hydrophilic particles (PhTCS-modified) at the optimum hydrophobicity.

Regardless of the exact mechanism, these results reinforce the hypothesis that the phase of initial dispersal is extremely important for determining the resulting emulsion type and droplet size. The results also suggest that the 'effective' hydrophobicity of the particles *in situ* may be extremely important to emulsion stabilization, and the hysteresis observed depending on the phase of initial dispersion strongly indicates that the resulting emulsions are not global thermodynamic equilibria, but simply local equilibria that are highly path-dependent and likely controlled by particle diffusion, fluid viscosity, emulsification method, and numerous other parameters.

CONCLUSIONS

Nanoparticle wettability and contact angle, as measured by a variety of methods, seems to have a strong dependence on the type of surface group grafted on to the silica's surface hydroxyls and a lesser dependence on the level of surface coverage of the surface modifiers. Heat of immersion tests confirmed the results of Oh et al[15] in regards to the creation of superhydrophilic surface moieties when MPTMS-modified silica is successively exposed to hydrogen peroxide and sodium hydroxide solutions. Emulsions stabilized by the various hydrophobically modified nanoparticles were shown to follow four general trends: 1) low surface coverage nanoparticles stabilized O/W emulsions while high surface coverage nanoparticles stabilized W/O emulsions in almost all cases;

2) emulsions stabilized by high surface coverage nanoparticles have slightly smaller average droplet sizes than emulsions stabilized by low surface coverage nanoparticles in every case but the oil-dispersed TMCS particles; 3) when the particles are initially dispersed in water, the emulsions stabilized by more hydrophobic nanoparticles had smaller average droplet sizes than emulsions stabilized by more hydrophilic nanoparticles, regardless of surface coverage; and 4) when the particles are initially dispersed in decane, the emulsions stabilized by more hydrophilic nanoparticles had smaller average droplet sizes than emulsions stabilized by more hydrophilic nanoparticles, in most cases.

Additionally, the heat of immersion method of determining particle wettability and contact angle appears to provide the largest range of measureable contact angles (ranging from < 0° to ~120°) when compared to the other methods tested here and also allows for quantification of the relative hydrophilicity for nanoparticles that are completely wet by the test liquid, a significant advantage when compared to other common methods of measuring particle wetting. The method also allows for direct measurement of particle-fluid interactions regardless of the type of fluid (water vs. oil vs. gas) as long as the particles can be easily wetted by the fluid, without requiring any type of reference liquid.

CHAPTER 3: PHASE BEHAVIOR AND PSEUDO-SOLID, SHEAR-THINNING GEL FORMATION IN BINARY DISPERSIONS OF FUMED METAL OXIDE NANOPARTICLES AT LOW VOLUME FRACTIONS

INTRODUCTION

Characteristics of metal oxide surfaces are strongly dependent on their chemical composition, method of synthesis, crystallinity, and concentration of surface hydroxyl groups. Metal oxide-liquid interfaces have been extensively studied[46] and metal oxide-water interfaces are of particular interest as the hydrogen bond network present in water (and other polar solvents) can stabilize charged chemical species on the metal oxide surface. Charged groups on the surface can result in strong electrostatic attraction or repulsion in aqueous suspensions of metal oxide nanoparticles.

The fumed metal oxide particles studied in this research are manufactured by flame pyrolysis/oxidation of metal chloride salts.[47,48] This technique has been well-researched and methods have been developed to tightly control the primary particle size, purity, and surface area. These nanoparticles are already commonly used as pigments and viscosity adjusters in consumer goods such as paints, cosmetics, and soaps. Dispersions of these nanoparticles have also been proposed for use as contrast agents in geological surveys of oil reservoirs.[49]

With widespread industrial applications, dispersions of fumed metal oxide nanoparticles have been extensively studied. Their complex geometric shape and the presence of surface hydroxyl groups allow fumed metal oxide nanoparticles to be used to adjust the viscosity of non-polar solutions. Raghavan et al.[50] showed a direct relationship between the gelation behavior of hydrophilic fumed silica nanoparticle dispersions and the hydrogen-bonding ability of the dispersing liquid. Gelation only occurred when the dispersing liquid had limited to no hydrogen-bonding ability. These liquids interact weakly with the silica surface, enabling adjacent particles to adhere through H-bonds

between the surface silanol groups. However, when these hydrophilic fumed silica nanoparticles are dispersed in liquids more capable of hydrogen-bonding, a solvation layer forms around the particles and largely eliminates interparticle hydrogen bonding, which results in only a minimal increase in solution viscosity.[51] Cao et al.[52] and Fisher et al.[53] have shown that spherical metal oxide nanoparticles can be made to form colloidal gels in aqueous solutions by adding NaCl to silica dispersions[6] or by mixing silica and alumina nanoparticles together in solution[7]. However, the gels studied by Fisher et al form at relatively high volume fractions (10-20 vol%) when compared to the gels described in this work (concentrations >1.5 vol%) and those studied by Cao et al. (1.0-4.7 vol%).

The rheological behavior and stability of metal oxide nanoparticle dispersions have been extensively studied previously in regards to the effect of solids fraction, electrolyte concentration, solution pH, particle size, presence of polymers and surfactants, etc. Binks et al.[54] investigated similar binary mixtures of silica-alumina nanoparticles in order to relate a particle mixture's ability to stabilize emulsions to the particle mixture's behavior in aqueous suspensions. The dynamics of heteroaggregation of oppositely charged nanoparticles and the structure of the heteroaggregates have been extensively studied by a variety of researchers. Kim et al[55] studied the heteroaggregation of oppositely charged polystyrene nanoparticles and found that, in the presence of a variety of background electrolytes, the oppositely charged nanoparticles will aggregate into fractal clusters with a fractal dimension varying from 1.21 to 1.70 depending on the concentration of electrolyte. Rasa et al[56] studied the heteroaggregation of similarly sized, spherical silica (negatively charged) and alumina (positively charged) nanoparticles in aqueous solution and found that in mixtures of <50% positively charged particles heteroaggregation and sedimentation was observed, while in dispersions containing >50% positively charged particles, only small, colloidally stable aggregates were

observed. This effect may be due to the higher surface charge density of alumina when compared to silica, meaning that it would take an excess of 2-4x the number of silica nanoparticles to create a mixture where the net surface charge of all of the nanoparticles in solution is approx. neutral. This idea is reinforced by the results shown by Rasa et al, who observed the greatest amount of heteroaggregation and sedimentation at silica-alumina ratios between 2 and 4, similar to the results seen in Binks' work. Lopez-Lopez et al[57] completed an extensive study of the heteroaggregation of oppositely charged, spherical nanoparticles and came to similar conclusions; when oppositely charged, spherical particles are initially introduced to each other in solution they tend to form long, diffuse fractal-like heteroaggregates, but that over long time scales these particles tend to continue to aggregate and often sediment out of solution or phase separate into a clear supernatant with a concentrated suspension of heteroaggregates below. All of these authors observed that when the oppositely charged, spherical particles were mixed together, they heteroaggregated and settled out of solution for almost all tested positive particle-negative particle ratios and pH's, in stark distinction to the pseudo-solid gels here that are highly resistant to sedimentation. Additionally, the pH ranges and particle ratios where Binks, Kim, Rasa, and Lopez-Lopez observed flocculation were very similar to the ranges and ratios where we observed the gelation phenomenon, implying that both phenomena may share a common mechanism: the heteroaggregation of oppositely charged particles in aqueous solution. One factor that explains this drastic difference in behavior is the structure of the nanoparticles studied. The nanoparticles used by Binks, Kim, Rasa, and Lopez-Lopez were synthesized using a precipitation method,[58] rather than the pyrolytic method used for the fumed metal oxides in this study. Precipitated metal oxides tend to form well-dispersed, single, spherical particles rather than the sintered nanoparticle aggregates with fractal structures obtained from pyrolytic synthesis methods. The multi-dimensional rigidity created by the fractal structures of

the fumed nanoparticles creates a barrier to the formation of dense aggregates, as shown by Garcia-Perez et al.[59] and Tombacz et al.[60] The inability to form dense aggregates may be one of the primary causes of the gelation phenomenon described here; the oppositely charged, fractal nanoparticles studied experience the same interparticle forces that result in heteroaggregation in the systems studied by Binks, Kim, Rasa, and Lopez-Lopez. Due to their three-dimensional rigidity and fractality the fumed nanoparticles are unable to assemble into heteroaggregates with a high enough density to settle out of solution, and thus remain suspended forming a space filling fractal network that gels the aqueous dispersion. In the study by Binks, the most stable emulsions were formed when the amount of sedimentation was maximized, and they hypothesized that when attractive, interparticle electrostatic interactions were maximized, emulsion stability was also maximized. Several researchers[61-63] furthered this hypothesis by showing that the differing charges on the nanoparticles help reduce interparticle dipole-dipole repulsion at the interface yielding more stable emulsions.

In studying these gels we have focused on two primary goals: mapping the gelation phase boundary of nanoparticle mixtures and understanding the nanoparticle network at the nano-, micro-, and meso-scale. This work provides the first comprehensive phase boundary map for these gel systems. Four characterization techniques were used: transmission electron microscopy (TEM), light microscopy (LM), small-angle x-ray scattering (SAXS), and acoustic spectroscopy (AS). These four characterization techniques were consistent with one another, indicating that the structures are not simply a result of a given preparation method. This unique compilation of analytical tools provides structural information about these materials across a variety length scales that are useful for understanding the overall behavior of the nanoparticle networks underlying the gelation phenomenon.

EXPERIMENTAL

MATERIALS

The nanoparticles used in this study were obtained from Evonik Inc. and include: Aerosil 150, Aerosil 200, and Aerosil 300, Aeroxide AluC, Aeroxide Alu130, Aeroxide TiO_2 P25, and Aeroxide TiO_2 P90. Aerosil 150 is a fumed silica nanoparticle with an average primary particle size of 14 nm, specific surface area of 150±15 m^2/g.[3] point of zero charge (PZC) of pH=4.0, and an average of 3 surface hydroxyls per nm^2.[12] Aerosil 200 is a fumed silica nanoparticle with an average primary particle size of 12 nm,[3] specific surface area of 200±25 m^2/g,[2] PZC of pH=4.0, and an average of 3 surface hydroxyls per nm^2.[12] Aerosil 300 is a fumed silica nanoparticle with an average primary particle size of 7 nm,[3] specific surface area of 300±30 m^2/g,[2] PZC of pH=4.0, and an average of 3 surface hydroxyls per nm^2.[12] Aeroxide Alu C is a fumed alumina nanoparticle with an average primary particle size of 13 nm,[3] specific surface area of 100±15 m^2/g,[2] PZC of pH=8.0, and an average of 8 surface hydroxyls per nm^2.[12] Aeroxide Alu 130 is a fumed silica nanoparticle with an average primary particle size of 10 nm,[3] specific surface area of 130±15 m^2/g,[2] PZC of pH=8.0, and an average of 8 surface hydroxyls per nm^2.[12] Aeroxide TiO_2 P25 is a fumed titania nanoparticle with an average primary particle size of 21 nm,[3] specific surface area of 50±15 m^2/g,[2] PZC of pH=5.9, and an average of 6.8 surface hydroxyls per nm^2.[12] Aeroxide TiO_2 P90 is a fumed silica nanoparticle with an average primary particle size of 14 nm,[3] specific surface area of 90±20 m^2/g,[2] PZC of pH=5.9, and an average of 6.8 surface hydroxyls per nm^2.[12] The sintered fractal aggregates for all of the nanoparticles used, which cannot be broken down further, range from ~30-200 nm in size, as determined by TEM and Acoustic Spectroscopy. The nanoparticles were manufactured by flame pyrolysis of metal chlorides at high

temperature (1000°C).[3] During the pyrolytic manufacturing process, the molten, spherical primary particles collide with one another and sinter together to form the fractal aggregates mentioned previously. These fractal-like nanoparticles are imperfect crystals and therefore contain surface hydroxyl groups that can be protonated or deprotonated depending on the pH of the suspending solution. When calculating nanoparticle volume fractions, the density of the nanoparticles was assumed to be that of bulk, amorphous silica, alumina, and titania, which is 2.25, 3.85 and 4.23 g/cm^3, respectively. These densities are comparable to those cited in the literature, as determined by solution densitometry.[64,65,66]

A polyhydroxy-aromatic acrylic embedding resin, LR White, was used for the TEM/ultramicrotomy studies, and was obtained from Ted Pella, Inc. Solutions of LR White with 10 wt% hydrochloric acid and 10 wt% sodium hydroxide, both purchased from Fisher Scientific, Inc., were used so the solution pH could be controlled. De-ionized water with a conductivity of <2 µS/cm was used for preparing aqueous dispersions and obtained using a polymer ion-exchange filtration system. For light microscopy experiments, gel samples were stained using Mallory's Azure II Methylene Blue dye.

METHODS

The gelation phase boundary was investigated by preparing 20 mL aqueous dispersions (using deionized water) of binary mixtures of metal oxide nanoparticles at varying particle ratios (defined on a volume fraction, vol/vol basis) while maintaining a constant volume fraction of solids. Particles were dispersed via vortex mixing at 3200 rpm for approx. five minutes; additional mixing with a spatula was necessary for gels with >2.5 vol% solids due to their very high viscosity/yield stress. The solution pH of these dispersions was varied from 2 to 13 in order to map the gelation region as a function

of both particle ratio and pH. All pH adjustments were made with highly concentrated HCl and NaOH solutions (10 wt%, in both cases) in order to minimize the effect of dilution during the pH scan.

Four different techniques (TEM, SAXS, AS, and LM) were used to characterize the structure of the nanoparticle network within the gels. A JEOL 2000-FX TEM was used to study the in-solution nanoparticle network. Samples were prepared for TEM study by dispersing particles in LR White, a hydrophilic resin solution, at a 70:30 silica:alumina ratio and concentration of 1.75 vol%. This was a ratio and concentration that was known to form a gel in an aqueous solution. The resin was then polymerized into a solid by placing the sample into a 40 ^{o}C oven for 48 hours in a tightly sealed gelatin capsule. The solidified polymer-nanoparticle composites were then removed from the gelatin capsules and 50-100 nm slices were removed from the sample using a Reichert UltraCut E ultramicrotome. The thin sections were then placed on a holey carbon TEM grid for imaging.

SAXS experiments were performed using a pinhole-collimation SAXS system from Rigaku with a copper anode (λ=0.154 nm) and a 2-D wire-style x-ray detector capable of measuring scattering vectors ($q=4\pi\sin\theta/\lambda$) from 0.07 nm^{-1} to 4 nm^{-1}. SAXS was used to probe the fractal dimension of both the primary nanoparticles and the nanoparticle networks present in the gels using methodology used by previous authors.[67-70] A 1.7 mm capillary was used to measure liquid samples and pure water in the same capillary was used as the background. SAXS was also used to confirm that the bulk structure of the nanoparticle network is consistent between the aqueous gels and the polymerized LR White block to ensure that the structure observed in the TEM micrographs is a realistic representation of the gel network present in the aqueous dispersions and has not been distorted by the polymerization reaction.

Acoustic spectroscopy is a reliable technique for characterizing concentrated dispersions in-situ.[71] A Dispersion Technology Inc., DT 1201 acoustic spectrometer was used for measuring the particle size distributions and zeta potential of the gel network samples. During operation, attenuation and frequency changes are measured at 21 different transmitter-receiver gaps (0.1 – 20 mm) and 18 different signal frequencies. The total attenuation is measured as a sum of the attenuation caused by viscous, scattering, thermal, structural, and intrinsic losses (Eq. 3). For particle size distribution measurements, the experimental attenuation is fit to the theoretical attenuation described in Eq. 3. Depending on the particle type, critical frequency and loss mechanism dominant for each system, the most appropriate prediction model will be used to quantify the particle size distribution. For this study, the binary mixture of nanoparticles were defined as a large particulate system based on the TEM and optical microscopy images. For large particulate systems (> 3μm), the scattering loss mechanism contributes primarily to the total attenuation. A detailed description of fitting the experimental attenuation data to the theoretical model has been published by Dukhin and Goetz[26].

$$\propto_{Total} = \propto_{Viscous} + \propto_{Scattering} + \propto_{Thermal} + \propto_{Structural} + \propto_{Intrinsic} \qquad \text{(Eq. 3)}$$

Zeta-potential is measured using electroacoustic theory to model the electric field produced when acoustic energy is applied to a dispersion of charged particles. The induced electric current is referred to as the colloidal vibration current (CVI) and is directly related to the zeta potential of the dispersed particles. The CVI signal is converted to acoustic signal using Eq. 4 to predict the zeta potential of the dispersion as a function of the particle size and standard deviation which are calculated from the acoustic theory particle size prediction model.

$$\text{CVI} = \frac{3\varepsilon_m \varepsilon_o \zeta}{a} \frac{\varphi}{1+0.5\varphi} \frac{1}{\sin\theta} \frac{\partial u_\theta}{\partial r_{r=a}} \qquad \text{(Eq. 4)}$$

For the acoustic spectrometer measurements shown here, 300 mL samples were prepared with 70:30 ratio of silica (Aerosil 200) to alumina (Aeroxide AluC) and a total nanoparticle concentration of 2 vol % with the remaining 98 vol% consisting of deionized water. The sample was mixed well by shaking vigorously by hand for five minutes and the pH was measured. The pH of the sample was then adjusted using 10% NaOH and HCl solutions, accordingly. Independent samples were prepared for each pH value tested to avoid dilution in the nanoparticle gel via addition of further NaOH or HCl solution.

Light microscopy experiments were performed on the gel samples using a Leica TCS SP2 microscope system at various magnifications for comparison with the other characterization techniques. The gel samples were stained using one drop (~10 μL) of Mallory's Azure II Methylene Blue dye prior to imaging.

RESULTS AND DISCUSSION

GELATION PHASE BEHAVIOR

This study focuses on three parameters (particle concentration, solution pH, and particle ratio) and how they affect the gelation of binary mixtures of fumed metal oxide nanoparticles. Gelation occurs in polar liquids when the solution pH is between the isoelectric points (also known as the point of zero charge or PZC) of the two metal oxides, i.e. one particle has a net positive charge and the other has a net negative charge. Net surface charge is controlled by solution pH because hydroxyl groups located on the surface of the metal oxide nanoparticles can be in a protonated or deprotonated state depending on solution pH, which changes the surface charge. The sign and magnitude of the surface charge also depends on the type of metal oxide, i.e. silica, alumina, and titania, because the type of metal atom changes the pK_a of the metal oxide's surface hydroxyl groups (altering the isoelectric point) and the number of surface defects (altering the number of charged surface sites per unit area). The gel networks studied here are formed due to electrostatic interactions between oppositely charged

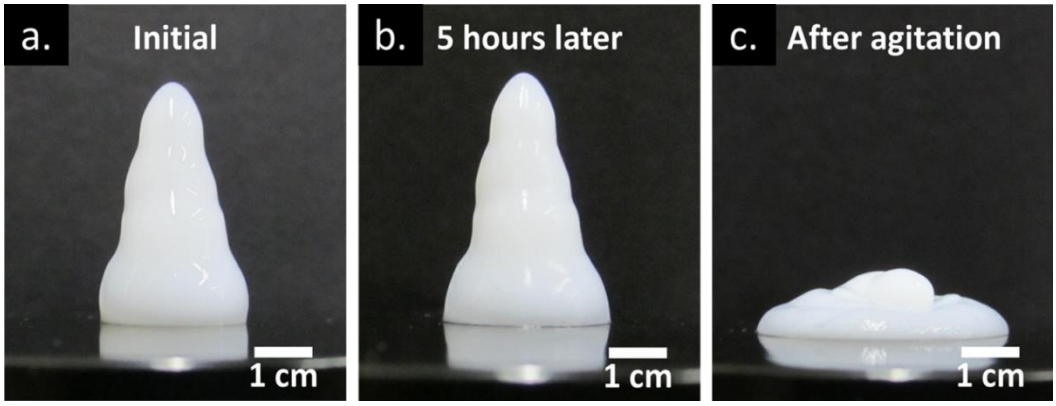


Figure 8. Images illustrating the gels' pseudo-solid behavior under gravity (a & b) and shear-thinning behavior observed when the gel is mildly perturbed by vibrational forces exceeding the gel's yield stress.

nanoparticles. These networks can be broken when the solution pH crosses one of the particles' isoelectric points (i.e. switching the sign of the particle's surface charge), or when enough stress is added to the system to overcome the particles' electrostatic interactions, physically breaking the nanoparticle network. Figure 8 illustrates how these gels resist flow and behave in a pseudo-solid manner under gravitational forces over many hours (a and b), but flow and slump quite readily when agitated with a force greater than the yield stress (c). The amount of stress required to cause the gels to flow, or yield stress, is defined as the stress at which the gel undergoes plastic deformation. The yield stresses for the 75-25 Aerosil 200-Aeroxide Alu C gels are 54 Pa, 160 Pa, and 329 Pa for the 1.75 vol%, 2.0 vol%, and 2.5 vol% samples, respectively. The gels also exhibit very little thixotropy; relaxing back from the liquid state to the gel state immediately after being stressed/strained with no observable 'setting' time. The quick relaxation/gelation phenomenon is based on direct observation and attempts to quantify gel thixotropy using a strain-controlled rheometer have not provided any useful insights.

Figure 9 contains a series of representative images that illustrate the drastic viscosity change observed at the gel region's phase boundary. The gel phase boundaries were determined by visually observation of the samples while adjusting the solution pH. These images help illustrate how drastic the phase transition if for these gels, with the

dispersions transitioning from a yield stress gel to a more water-like particle dispersion with relatively low viscosity (<20 cP at shear rates >100 s^{-1}).

Figure 10 (a-f) contains a collection of phase diagrams for binary mixtures of metal oxide nanoparticles as a function of both solution pH and particle ratio. For these diagrams the phase of the dispersions was determined visually by observing whether the samples exhibit yield stress behavior at the conditions tested. As illustrated in Fig. 9, the gel-fluid transition is not subtle, therefore no further characterization technique was used to determine the phase boundaries for the diagrams in Fig. 10 beyond visual observation of the samples. Samples within the gel region exhibit a high viscosity and noticeable yield stress due to electrostatic interactions between the oppositely charged nanoparticles. The interactions result in heteroaggregation of the two different nanoparticle species throughout the entire dispersion, creating a network of heteroaggregates that spans the entire fluid. Some samples near the phase boundary exhibited obvious viscosity increases in comparison to samples clearly outside the gel region, but did not exhibit a noticeable yield stress. It is believed that this behavior is a

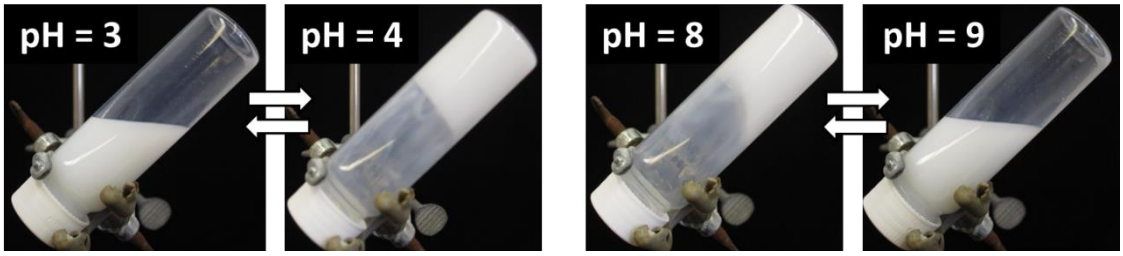


Figure 9. Representative images showing the significant transition from low-viscosity fluid to pseudo-solid gel, and vice versa, observed when crossing the gel region's pH boundary. Samples shown have a total particle concentration of 2.0 vol% and are a 70-30 mixture of Aerosil 200-Aeroxide Alu C. Pictures were taken after 1 min of inversion; pH adjustments were made using 10 wt% solutions of HCl and NaOH.

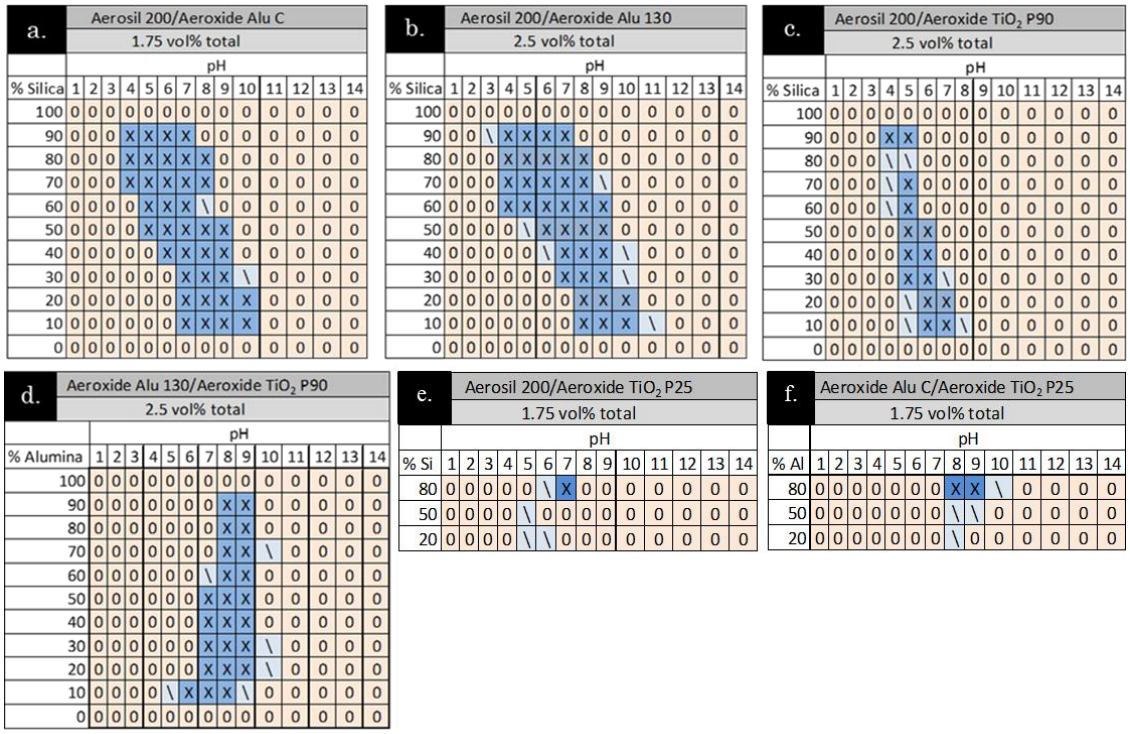


Figure 10. Phase behavior diagrams for various binary mixtures of fumed metal oxide nanoparticles in deionized water. X's indicate gel formation, O's indicate low-viscosity suspensions, and /'s indicate mild viscosity increases. Both silica/ alumina mixtures (a&b) experience gelation in a pH range between 4 and 10 with the gel region shifting to higher pH range as Si/ Al ratio decreases. Silica/ titania mixtures (c&e) show gelation between pH's 4 and 7, and alumina/ titania mixtures show gelation between 7 and 9. For different alumina and titania particles tested, the particles with smaller primary particle size (Alu130, Ti P90) were more effective for gel formation.

result of the samples containing a mixture of large heteroaggregates of the two nanoparticles along with a significant fraction of individualized excess particles, resulting in a viscosity increase, but lacking enough interparticle and interaggregate connections to form the volume-spanning network necessary for the samples to exhibit a yield stress; samples of this nature have been designated with a '/' in Fig. 10's phase diagrams. For all of the tested nanoparticle mixtures, the gelation behavior supports the hypothesis that gel formation occurs due to electrostatic interactions between oppositely charged nanoparticles because the gel region corresponds with the pH range between the two particles' isoelectric points. For example, the gel region for the silica:alumina (Figs. 10a and 10b) mixtures corresponds to 3 < pH < 9-10; the isoelectric point of silica is 1.7-3.5 and the isoelectric point of alumina is 7-9,[72] where the exact value depends on

the crystal phase of the metal oxide. Similarly, when silica or alumina are mixed with titania (Figs. 10c-f), the gel region shifts to only cover the pH range between the silica/alumina isoelectric point and the titania isoelectric point of pH = ~6. If the regions of gelation from the phase behavior diagrams for the Aeroxide Alu 130/Aeroxide TiO_2 P90 (Fig. 10c) and Aeroxide TiO_2 P90/Aerosil 200 (Fig. 10d) mixtures are combined together, the resulting region of gelation closely matches the phase behavior diagram of the Aeroxide Alu 130 mixture/Aerosil 200 (Fig. 10b). This implies that the gelation is primarily a result of electrostatic interactions between the nanoparticles and that gelation would likely be observed with other types of fumed metal oxides nanoparticles beyond silica, alumina, and titania.

STRUCTURAL STUDIES OF THE GEL NETWORK

Prior to polymerization, the LR White/nanoparticle dispersions exhibited the same pseudo-solid/shear-thinning behavior as the aqueous gels. Fig. 11 contains a selection of TEM micrographs of the nanoparticles dispersed in polymerized LR White resin. TEM studies showed that the samples contain two major types of morphologies: 1.) areas dominated by empty space interspersed with nanoparticle aggregates with apparent sizes ranging from approximately 200 nm up to 5 μm, and 2.) areas dominated by unbroken networks of nanoparticles that extend for hundreds of micrometers in all directions. Micrographs a.-c. show regions of the gel sample with the first type of morphology with seemingly independent aggregates. However, it is currently unclear if these are truly independent aggregates or merely appear to be independent due to an artifact from the thin-sectioning. The thin sections imaged here are merely thin slices of a three dimensional gel network, therefore what appear to be independent aggregates at

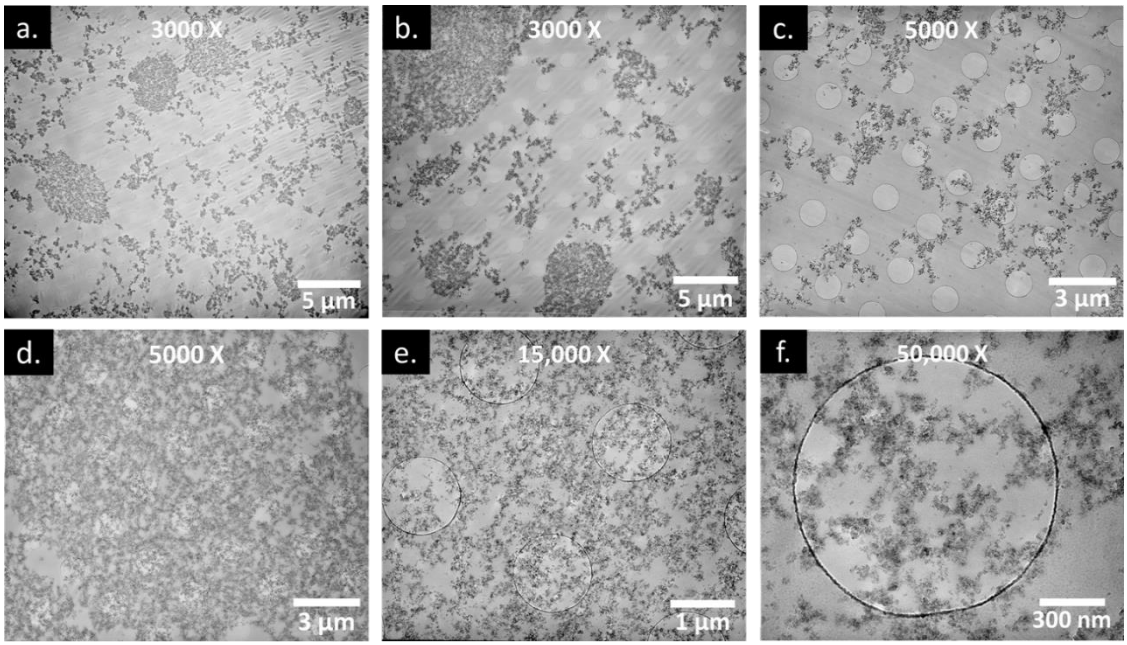


Figure 11. TEM micrographs illustrating areas of low particle density, containing dispersed nanoparticle aggregates of a variety of sizes with empty void spaces between them (a-c), and a series of micrographs showing a region of unbroken nanoparticle networks that extend for 10's of microns in all directions, at three different levels of magnification. Images are of ~100 nm thick sections of a 1.5 vol% 30-70 AluC-Aerosil 200 dispersions in polymerized LR White resin. Circles in background are from TEM grid.

the level of these images may actually be connected to the overall nanoparticle network at a different point in the sample above or below the image plane. Micrographs d.-f. illustrate examples of the second type of morphology, showing unbroken nanoparticle networks at three different levels of magnification, which illustrate the fractal-like nature of both the primary particles and the gel network, as they exhibit self-similar features over wide ranges of magnification.[73]

Small-angle x-ray scattering (SAXS) experiments were used to compare the aqueous gel dispersions with the nanoparticle networks suspended in LR White resin to confirm that the structures observed in Fig. 11 were an accurate representation of the nanoparticle networks that cause the gelation observed in aqueous dispersions. SAXS can be used to characterize the size, shape, characteristic distances, fractal dimension, pore sizes, and other information for features with a size range of ~1-100 nm. Experiments revealed that the normalized (normalized because of the difference in

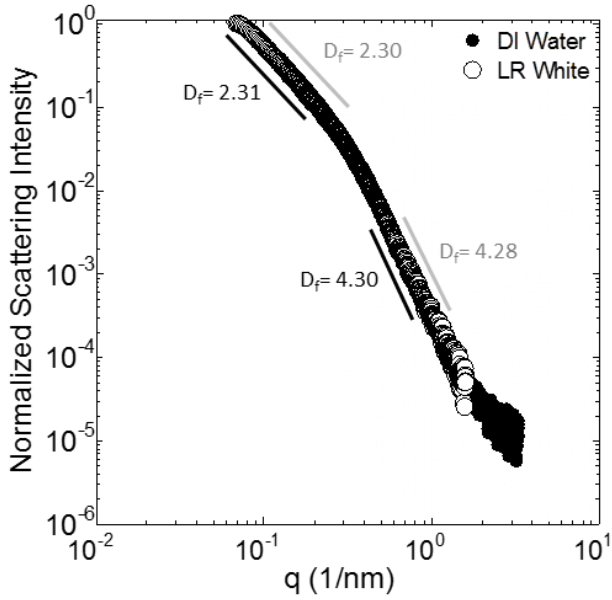


Figure 12. Small-angle x-ray scattering (SAXS) attenuation spectra illustrating the structural morphologies of the SiO_2 and Al_2O_3 in DI water and LR white.

electron density between water and the polymer resin), background-corrected SAXS spectra, shown in Fig. 12, are almost identical throughout both the Porod region of q (0.3 nm^{-1} < q < 2 nm^{-1}) which has features corresponding to characteristics of primary particles and the Guinier region of q (0.06 nm^{-1} < q < 0.3 nm^{-1}) which has features corresponding to characteristics of primary particle aggregates and small multi-particle networks. Fractal dimensions were calculated by fitting the data in Fig. 12 to Beaucage's Unified Power Law Scattering model.[17] The fractal dimension (D_f) of the Porod region, 4.28-4.30 corresponds to power law scattering from a fractally smooth solid object, in this case the spherical primary particles. The fractal dimension of the Guinier region (2.30/2.31) is very similar for both systems, indicating that the spherical primary particles are arranged in similarly branched networks in both samples, this fractal dimension also corresponds closely to the fractal dimension of 2.5 calculated by Tolman and Meakin[74] for diffusion-limited particle-cluster agglomeration (DLA) in three dimensions, indicating that the fractal structures are relatively closed, but are consistent with DLA. The location of the transition between the Porod and Guinier scattering (~0.3 nm^{-1}) is also consistent for both samples, as expected. These scattering results indicate that the structure observed in the TEM micrographs of the nanoparticle network in resin (Fig. 11) are representative of the networks that are observed in the aqueous gels, at least over the scattering vectors (q) that can be probed with the SAXS equipment available.

However, since some of the sintered fractal aggregates of the silica and alumina are larger (aggregates range from ~30-200 nm in size, as determined by TEM) than the maximum feature size that can distinguished with SAXS (~100 nm), we cannot conclusively state that the long-range structure of the LR White and aqueous gels are completely similar since the scattering results shown in Fig. 12 could simply reflect scattering from a weighted average of the individual fractal aggregate particles. Therefore, additional ultra-small angle x-ray or neutron scattering experiments, which can probe feature sizes up to ~6 μm, will be necessary to determine if the nanoparticle network structures are consistent over the larger length scales shown in electron micrographs. SAXS spectra shown in Fig. 12 are a combination of the scattering from both the silica and alumina particles. Additionally, since the electron density of silica is ~75% of the electron density of alumina, the combined scattering spectra in Fig. 12 over-represent the scattering profile of the alumina relative to its concentration in solution because x-ray scattering is proportional to the electron density of the scatterer, a problem that could be alleviated by conduction neutron scattering experiments since the neutron scattering cross sections of silica and alumina are quite similar.

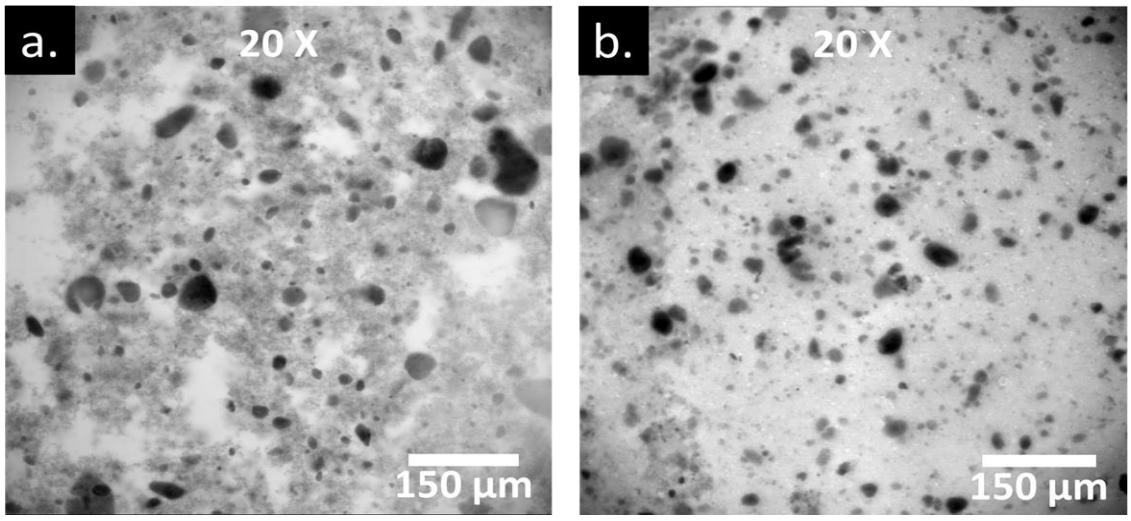


Figure 13. Optical microscope images for samples inside and outside the gel region: (a.)1.5 vol%, 30-70 AluC-Aerosil 200, pH = 7 and (b.) 1.5 vol%, 30-70 AluC-Aerosil 200, pH = 2.

Figure 13 shows optical microscopy images of 1.5 vol%, 30–70 Aeroxide Alu C–Aerosil 200 nanoparticle dispersions in deionized water after being dyed with one drop of Mallory's trichrome stain. Micrograph a. shows a dispersion at pH = 7, which is within the gel region, while micrograph b. shows a dispersion at pH = 2, which is outside the gel region. As seen in Fig. 13a., the gel-region sample contains observable, nanoparticle networks, while Fig. 13b. does not appear to contain any interconnected nanoparticles networks spanning the image, but instead appears to contain particle aggregates separated by empty spaces of water. One can also observe the previously discussed self-

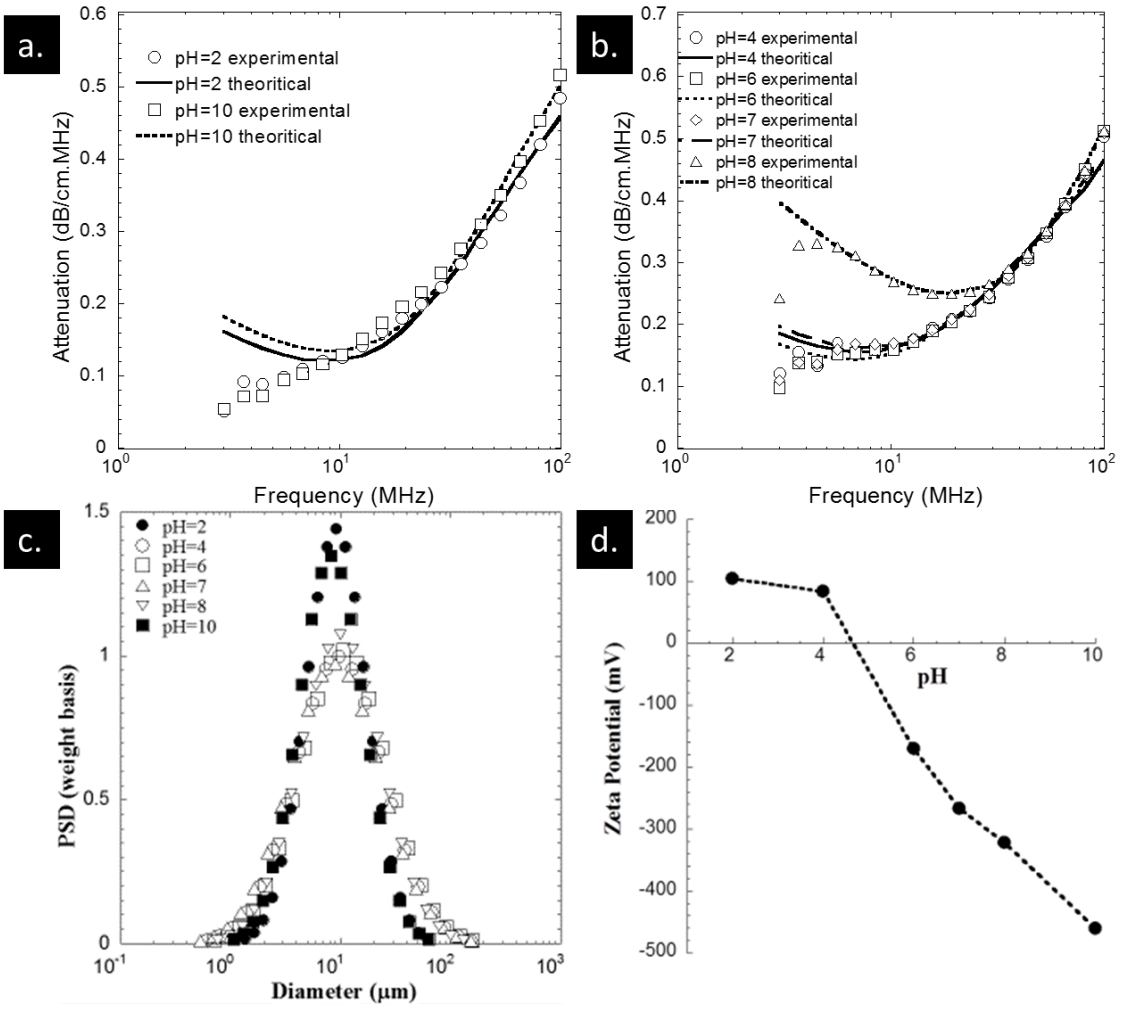


Figure 14. Measured attenuation spectra for the non-gel and gel samples (a. and b respectively), particle size distributions (c.) and ζ-potential (d.) of 1.5 vol% 30–70 Aerosil 200–Aeroxide Alu C dispersions at various pH values. The samples at pH 4, 6, 7, and 8 are gels, while the pH 2 and 10 samples are outside the gel region.

similarity between micrographs in Fig. 11 d.-f. and those in Fig. 13a., where a similar fractal pattern of interparticle connections is observed. The round, dark spots in Fig. 13a.-b. are believed to be concentrated regions/droplets of stain, not nanoparticle aggregates.

Figure 14 contains all of the experimental results from the acoustic spectroscopy measurements on 1.5 vol%, 30–70 Aeroxide Alu C–Aerosil 200 dispersions at pH values of 2, 4, 6, 7, 8, and 10. Fig. 14a. and b. show a comparison of the experimental data fit to the theoretical model, as described in the methods section, for the non-gel and gel samples, respectively. A sharp contrast can be seen in the attenuation spectra for the gel region samples (pH = 4, 6, 7, and 8) and the spectra for the two samples outside the gel region (pH = 2 and 10), shown in Fig. 14a and b. The high viscosity gel samples exhibit more ultrasound attenuation at low frequencies than the non-gel dispersions, which is likely due to strong particle-particle interactions when the silica and alumina particles have opposing surface charges. Figure 14c. shows the particle size distributions for all of the tested samples which is calculated by fitting the experimental attenuation curves to a unimodal model based on acoustic theory. The attenuation of the sample at pH equal to 8 is higher than the other gel samples because this sample was very close to the

Table 6. Mean particle size and zeta potential of 1.5 vol% 70:30 binary mixture of Aerosil 200:Aeroxide AluC dispersions.

Sample	Mean Particle Size (μm)	Zeta Potential (mV)
pH= 2	11.2	104.9
pH=4	14.8	84.3
pH=6	14.5	-169.7
pH=7	13.7	-266
pH=8	14.2	-326.2
pH=10	10.4	-461.8

isoelectric point of alumina (pH = 8-9). Table 6 contains a summary of the mean particle sizes and zeta potential for each pH that was considered.

Fig. 14d. shows how the ζ-potential changes as a function of pH in binary dispersions of Aeroxide Alu C and Aerosil 200. The mixed particle dispersions go through an isoelectric point between pH 4 and 6. Unexpectedly, there do not appear to be large changes of ζ-potential associated with crossing the gel region boundary, as the ζ-potential of the pH 2 and pH 4 samples are very similar. The difference between the ζ-potentials of the pH 8 and pH 10 samples is not greater than the difference between the pH 6 and pH 8 samples. For binary mixtures of fumed nanoparticle dispersions, the zeta potential is due to the combined effect of electrostatic interaction between the two oppositely charged particles. For dispersions in the acidic pH region (pH's of 2 and 4 sample), the zeta potential is primarily attributed to the interaction between the H^+ ions and the excess charge due to silica particles. Whereas, for dispersions with low H^+ ion concentration, the zeta potential is caused due to the excess charge from the alumina particles. This implies that if the gelation mechanism involves strong interparticle electrostatic attractions (which the phase behavior studies seem to indicate is the case), then the electroacoustic method of measuring the surface potential may not be fully capturing the surface charging phenomena in these particular dispersions due to the added complications of particle-particle interactions.

CONCLUSIONS

The gelation mechanism described here appears to be the result of electrostatic interactions between oppositely charged nanoparticles dispersed in a polar solvent, but these electrostatic interactions can be broken by the addition of a shear force to the solution that is strong enough to break the network's binding forces, overcoming the gel's yield stress,[75,76] inducing plastic deformation and flow.[77] However, the electrostatic attraction that generates the gel network does not seem to lead to particle aggregation

and the unstable dispersions seen by Binks and others. The gels are likely stabilized by a combination of three important phenomena: firstly, repulsive electrostatic interaction between like-charged particles preventing aggregation beyond a certain limit where attractive silica-alumina interactions are balanced against repulsive silica-silica and alumina-alumina interactions; secondly, the fractal structure of the sintered primary particle aggregates add three-dimensional rigidity that prevents aggregates from being tightly packed together into dense aggregates[78] that can no longer be suspended in solution by Brownian forces; and finally, hydration forces related to enthalpically adsorbed water molecules at the solid-liquid interface resisting the desorption necessary for dispersed particles to come into direct contact with one another.[79]

The microscopic and macroscopic structure of these gels was investigated using electron microscopy, optical microscopy, small-angle x-ray scattering, and acoustic spectroscopy. All of these techniques indicated that, when dispersed in water at particle ratios and pH's where gel formation occurs, the nanoparticles appear to connect in a large-scale fractal network throughout the solution. These fractal networks can be seen at a wide variety magnifications and exhibit the self-similarity that are expected of fractal networks.

CHAPTER 4: RHEOLOGICAL CHARACTERIZATION OF PSEUDO-SOLID, SHEAR-THINNING GELS FROM BINARY DISPERSION OF FUMED METAL OXIDE NANOPARTICLES AT LOW VOLUME FRACTIONS

INTRODUCTION

Yield stress fluids, or Bingham plastics, are widely found both in industry (drilling muds, plastic extrusions) and our daily lives (toothpaste or mayonnaise), these fluids behave like an elastic solid under small stresses, but flow like viscous liquids when exposed to sufficient stress. Many particle suspensions, polymer dispersions, and emulsions exhibit yield stress behavior and will only undergo viscous flow after being subjected to a stress large enough to degrade the three-dimensional structure of the dispersed phase, commonly referred to as the yield stress. Colloidal gels which behave as yield stress fluids have a wide range of potential and current applications, such as altering flow patterns in porous media,[80] vibration dampening in electrorheological suspensions,[81,82] forming cake filtration beds,[83] printing flexible microelectrodes,[84] improving performance of woven body armor[85] and fabricating durable biological scaffolds.[86] A variety of colloids have been found to form yield stress fluids when dispersed in a liquid: paper pulp fibers,[87] various clay minerals,[88] and carbon black.[89]

Metal oxide nanoparticles are widely used in a variety of industrial and consumer product applications. These nanoparticles are quite complex and their behavior depends on factors such as chemical composition, synthesis method, degree of crystallinity, and number of surface defects. In particular, fumed metal oxide nanoparticles are synthesized through co-injection of hydrogen, oxygen, and metal chlorides into a flame at temperatures in excess of 1500°C, where the metal chlorides oxidize to form spherical nanoparticles.[90,91] After oxidation, the spherical nanoparticles remain suspended in the gas stream at high temperatures, where they collide with each other due to turbulence and sinter to form 'hard' fractal aggregates that cannot be broken apart via

homogenization or ultrasonication. The sintered fractal aggregates can agglomerate into larger 'soft' structures due to van der Waals forces.[92] These larger 'soft' agglomerate structures can be broken apart by homogenization or ultrasonication.[93] Fumed metal oxide nanoparticles are already commonly used as pigments and viscosity adjusters in consumer goods such as paints, cosmetics, and soaps. Dispersions of these nanoparticles have also been proposed for use as contrast agents in geological surveys of oil reservoirs.[94]

Widespread industrial use of fumed metal oxide nanoparticles has resulted in study of their behavior when dispersed in a liquid. Their complex geometric shape and ability for particles to hydrogen bond with each other via surface hydroxyls allow fumed metal oxide nanoparticles to be used to adjust the viscosity of non-polar solutions. Numerous groups have studied the ability of unmodified (hydrophilic) fumed silica to form yield stress gels when dispersed in non-polar solvents[95,96] and Raghavan[97] demonstrated a direct relationship between the gel strength and the ability of the dispersing liquid to hydrogen bond with the metal oxide surface. Gelation only occurred when the dispersing liquid had limited to no hydrogen-bonding ability, meaning the liquids interact weakly with the silica surface encouraging the particles to form a volume-spanning fractal network held together by interparticle hydrogen bonds. Alternatively, when hydrophilic fumed silica nanoparticles are dispersed in liquids more capable of hydrogen-bonding, like water, a solvation layer forms around the particles and largely eliminates interparticle hydrogen bonding, resulting in a minimal increase in solution viscosity.[98]

The interactions between aqueous solutions and metal oxide surfaces have been extensively studied[99,100,101] and are of particular interest for this work because the hydrogen bond network present in water can stabilize charged chemical species on the metal oxide surface resulting in strong electrostatic attractive or repulsive forces between

metal oxide nanoparticles. Electrostatic charges on metal oxide surfaces are governed by the protonation state of hydroxyl groups scattered across all metal oxide surfaces. If the hydroxyl group is doubly protonated, which occurs at low pH, the surface takes on a net positive charge. As the solution pH increases the number of doubly protonated hydroxyl groups decreases while the number of deprotonated, i.e. negatively charged, hydroxyl groups increases. The surface charge thus goes through a transition between a net positive charge at low pH and a net negative charge at high pH with the pH where a zero net surface charge (an equal number of positively charged and negatively charged surface sites) occurs being known as the isoelectric point (IEP) or point of zero charge (PZC). The pH where the isoelectric point occurs differs depending on the type of metal oxide being studied. More complex aluminosilicates have surface regions with different IEPs; i.e. for some pH ranges a fraction of surface regions will be positively charged while others are negatively charged.

Dispersing oppositely charged nanoparticles in the same liquid can lead to colloidal gels under certain conditions. Fisher[102] has shown that spherical metal oxide nanoparticles can be made to form colloidal gels in aqueous solutions by adding small amounts (< 1 vol%) of spherical silica nanoparticles to 10 vol% alumina slurries at a pH between the two IEPs. Gelation occurs due to electrostatic interactions between smaller (5-25 nm) silica nanoparticles and larger (250 nm) alumina particles, resulting in a volume-spanning network of heteroaggregates. Kim[103] studied the heteroaggregation of oppositely charged polystyrene nanoparticles and found that, in the presence of a variety of background electrolytes, the oppositely charged nanoparticles will aggregate into clusters with fractal dimensions varying from 1.21 to 1.70 when the liquid phase is density matched with the polystyrene particles to prevent sedimentation. They also found that the fractal dimension of the aggregates was slightly affected by particle concentration, but strongly affected by the addition of salts, which increase electrostatic screening

between particles. Zong[104] characterized the rheological behavior of similar mixtures of oppositely charged polystyrene particles over a range of volume fractions (0.18-0.53) in order to quantify the particle bonding and caging present in the dispersions. Rasa[105] studied the heteroaggregation of similarly sized, spherical silica (negatively charged) and alumina (positively charged) nanoparticles in aqueous solution and found that in mixtures of <50 vol% positively charged particles, heteroaggregation and sedimentation occurred, while in dispersions containing >50 vol% positively charged particles, the liquid contained small colloidally stable aggregates but did not form a colloidal gel. Binks et al.[106] investigated similar binary mixtures of silica and alumina nanoparticles in order to relate a particle mixture's ability to stabilize Pickering emulsions with the particles' behavior in aqueous suspensions. They observed that particle mixtures with the greatest tendency to heteroaggregate and sediment out of solution (i.e. had the most interparticle attraction) were most able to stabilize oil and water emulsions. Lopez-Lopez[107] completed a study of the heteroaggregation of oppositely charged, spherical nanoparticles and came to similar conclusions; when oppositely charged, spherical particles are initially introduced to each other in solution they tend to form long, diffuse fractal-like heteroaggregates, but that over long time scales these particles tend to continue to aggregate and often sediment out of solution or phase separate into a clear supernatant with a concentrated suspension of heteroaggregates below. All of these authors observed that when oppositely charged, spherical particles were mixed together, they heteroaggregated and settled out of solution, unless either the liquid was density matched to that of the particles or the particles made up a large volume fraction (> 10 vol%) of the suspension.

The gels studied here are generated by dispersing mixtures of two different fumed metal oxide nanoparticles in deionized water at a pH where one nanoparticle specie is positively charged while the other is negatively charged. The key reason why these

particles did not sediment is that the individual species are themselves fractal in nature, preventing dense particle packing. Previous work has mapped the gelation phase boundaries for mixtures of silica/titania, silica/alumina, and titania/alumina and shown that the gels can be reversibly broken and reconstructed by varying pH.[108] Here, we focus on quantifying the rheological characteristics of the gels, e.g. the yield stress, apparent viscosity, and shear moduli, and how these properties change as a function of particle concentration, solution pH, and the ratio of positively charged particles to negatively charged particles.

EXPERIMENTAL

MATERIALS

The nanoparticles used in this study were obtained from Evonik Inc. and include: Aerosil 200, Aeroxide Alu C, and Aeroxide TiO_2 P90. Aerosil 200 is a fumed silica nanoparticle with an average primary particle size of 12 nm, specific surface area of 200±25 m^2/g, IEP of pH=4.0, an average of 3 surface hydroxyls per nm^2,[109] and an average fractal dimension of 2.22. Aeroxide Alu C is a fumed alumina nanoparticle with an average primary particle size of 13 nm, specific surface area of 100±15 m^2/g, IEP of pH=8.5, an average of 8 surface hydroxyls per nm^2,[109] and an average fractal dimension of 2.06. Aeroxide TiO_2 P90 is a fumed titania nanoparticle with an average primary particle size of 14 nm, specific surface area of 90±20 m^2/g, IEP of pH=5.9, an average of 6.8 surface hydroxyls per nm^2,[109] and an average fractal dimension of 2.02. All fractal dimensions are based on SAXS and SANS data described in detail in Part III of this series. The sintered fractal aggregates for all of the nanoparticles used, which cannot be broken down further, range from ~30-200 nm in size, as determined by TEM and acoustic spectroscopy. The nanoparticles were manufactured by flame pyrolysis of metal chlorides at high temperature (1000°C). When calculating nanoparticle volume fractions, the density of the nanoparticles was assumed to be that of bulk, amorphous

silica (2.25 g/cm^3), alumina (3.85 g/cm^3), and titania (4.23 g/cm^3), which are comparable to those determined by solution densitometry.[110,111]

De-ionized water with a conductivity of <2 μS/cm was used for preparing aqueous dispersions and obtained using a polymer ion-exchange filtration system. All pH adjustments were made with 10 wt% NaOH and HCl in order to prevent excessive dilution of the nanoparticles. Sodium hydroxide and hydrochloric acid were both purchased from Fischer Scientific.

Gels were prepared by weighing out the desired amount of each particle into a container along with the necessary amount of deionized water. Then, the particles were initially dispersed in the aqueous phase using a vortex mixer followed by an initial pH adjustment to the desired pH. Three pHs were used for each nanoparticle pairing: a pH below the isoelectric points of both particles, a pH in the center of the gel region between the two particles' isoelectric point, and a final pH above the isoelectric point of both particles. Next, the particle dispersions are sonicated using a Fisher Scientific FB505 horn sonicator with a 1/8 inch stainless steel tip for 9 minutes at 40% amplitude in order to break up particle agglomerates. Following sonication, the solution pH is checked a second time and, if it has changed by protonation/deprotonation of the surface hydroxyls, adjusted to the desired pH using NaOH and HCl.

METHODS

A variety of techniques have been developed to measure both shear and compressive yield stress.[112,113,114] These studies illustrate the difficulty of measuring the yield stress and other rheological properties of yield stress fluids. The ability to make accurate measurements strongly depends on the chosen geometry and precision with which the instrument can control stress and strain/strain rate, in order to prevent wall-slip, fracture, and shear banding.[115,116] Yield stress measurements here were made using a Rheometrics Scientific SR-5000 stress-controlled rheometer using a cone and plate

geometry. The cone/plate size was varied between 25 mm and 40 mm to ensure that the measured yield stress did not require torques outside of the apparatus' specified range. The 25 mm cone had a cone angle of 0.0996 radians and was operated at a gap of 0.0533 mm. The 40 mm cone had a cone angle of 0.0393 radians and was operated at a gap of 0.0787 mm. No major problems with wall slip or shear banding were observed during experimentation, so additional measures to control for these factors were not employed. Yield stress was measured by exposing a sample to a steady stress ramp until the sample began to undergo plastic deformation, the stress at which plastic deformation begins was taken to be the yield stress. A series of five stress ramp experiments were completed for each sample, with the average yield stress of all five runs being stated as the samples' yield stress.

Apparent viscosity was measured using two different methods. For low shear rates ($<0.1\ s^{-1}$) a Rheometrics Scientific SR-5000 rheometer was used with the same cone and plate geometry described previously. The rheometer was made to exert a constant stress on the sample until the shear rate and apparent viscosity stabilized; the shear rate and viscosity were then measured for five minutes and the average value over that time was used as the stated shear rate and viscosity for each sample. Then, the stress would be changed and the system allowed to stabilize again at a different shear rate. All sample measurements were taken using data that exhibited a steady build-up of stress as the sample approached its steady state viscosity to avoid collecting data from samples that have undergone significant network rearrangement prior to reaching steady state. Viscosity measurements were made in order of ascending stress/shear rate to avoid measurement errors related to wall slip. Viscosities at higher shear rates were measured using a Rheosys Merlin II rheometer using a 25 mm concentric cylinder (bob and cup) geometry, where the diameter of the cup is in proportion to the bob size as defined by the DIN Standard 53019. This rheometer can directly control shear rate, and shear rate

was increased from 0.1 s^{-1} – 2000 s^{-1} while measuring stress to obtain viscosity vs. shear rate data. At every measured shear rate, the sample was sheared for 30 s prior to data collection followed by a 45 s data integration time to determine sample viscosity. By using both of these instruments, a shear rate regime of seven orders of magnitude was collected. Further, no shifting of the data was necessary; the two instruments agreed when there was overlap between the shear rates.

Complex shear moduli were measured using a Rheometrics Scientific SR-5000 rheometer with the same cone and plate geometry described previously. The experiments were carried out at various frequencies and a constant strain of 1.0%, which was determined to be within the linear viscoelastic region for all of the gels tested. Again, 25 mm and 40 mm plates were used to ensure that the required torques were within the operating range of the rheometer. We were sure to choose conditions so that instrument inertia did not affect the results.

RESULTS AND DISCUSSION

Figure 15 contains a series of representative plots that illustrate the general rheological behavior of the studied gels in terms of viscosity vs. shear rate, viscosity vs. shear stress, and shear moduli vs strain. The plots illustrate extremely similar trends to the data presented by Aerschot and Uriev for 2.5 vol% hydrophilic fumed silica dispersed in methyl laurate, a non-polar liquid. As previously discussed, hydrophilic fumed silica will form a yield stress gel when dispersed in a non-polar solvent by forming a fractal network held together by interparticle hydrogen bonding. In the hydrogels studied here, an extremely similar fractal network is formed throughout the aqueous phase, but the network is held together by electrostatic interactions rather than hydrogen bonds. The electrostatically stabilized network studied here is significantly stronger than the hydrogen bond network studied by Uriev. In fact, the differences in viscosity, moduli,

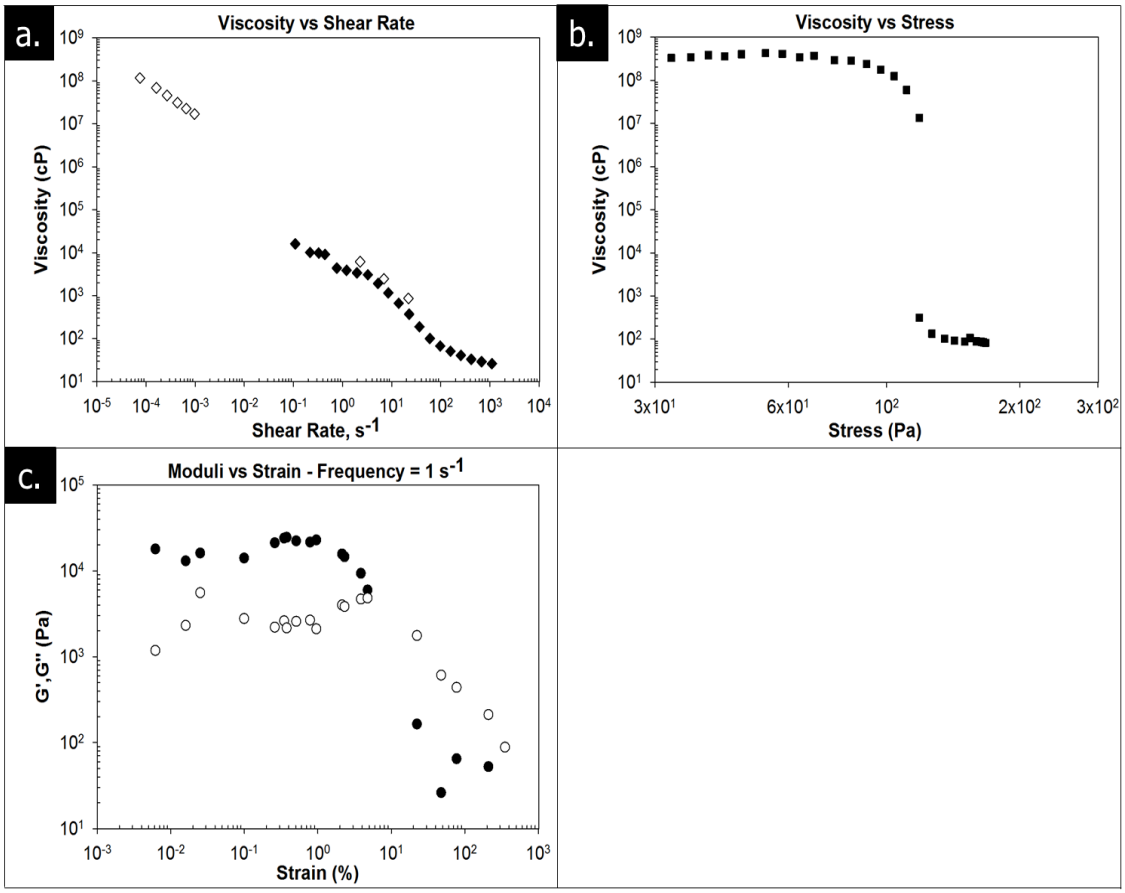


Figure 15. Representative plots of viscosity vs. shear-rate (a), viscosity vs. shear stress (b), and shear modulus vs. strain (c) for gels made of oppositely charged, fumed metal oxide nanoparticles dispersed in deionized water. Results shown here are for a gel with a 75-25 mixture of Aerosil 200 (silica)-Aeroxide Alu C (alumina), a total particle concentration of 2.0 vol%, and a solution pH of 7. The gel behaves as a power-law fluid over the tested shear rate range, has a yield stress of ≈150 Pa, and behaves as a linear viscoelastic solid for strains < 2-3%. Open symbols in (a) were measured using the SR-5000, closed symbols were measured using the Merlin II. Closed symbols in (c.) represent the storage modulus (G′) and open symbols represent the loss modulus (G″).

and yield stress roughly correspond to the difference in force between electrostatic interactions and hydrogen bonding, approximately 1-1.5 orders of magnitude.

A more detailed analysis of these graphs shows that in Figure 15a, the apparent viscosity follows a power law relationship with shear rate, a fairly common rheological phenomenon that has been used to describe the flow of a variety of different fluids and suspensions, e.g. drilling muds,[117] fresh concrete,[118] mud slides,[119] ideal hard sphere colloids,[120] and gluten gels.[121] The area of the plot between shear rates of 10^{-3} s^{-1} and 10^{-1} s^{-1} is largely bereft of data points because those shear rates correspond to stresses that

are near the yield stress of the gel where it transitions from elastic to viscous behavior, making it impossible to measure reproducible stress-strain data in this region on our equipment. Figure 15b. contains a plot of viscosity vs. shear stress which illustrates the obvious transition from solid-like to fluid-like behavior above and below the gel's yield stress of approximately 150 Pa. Figure 15c. displays how the storage and loss moduli change for these gels as the strain is increased. G' and G" largely do not change as a function of strain for strains below 2-3% and drop precipitously at strains above that level, indicating a transition from the linear to nonlinear viscoelastic region. As stated previously, G' and G" values as a function of frequency reported were measured at 1% strain, which is in the linear viscoelastic region.

YIELD STRESS

Yield stresses were measured for gels at particle concentrations varying from 1.0 vol% -2.5 vol%, at three different particle ratios, and at pHs below, within, and above the gelation region for three different binary mixtures of fumed metal oxide nanoparticles: silica-alumina, silica-titania, and titania-alumina. Figure 16 shows examples of the stress-strain data gathered during a typical yield stress test for 75-25 Silica-Alumina dispersions at three different particle concentrations. The stress where the gels begin

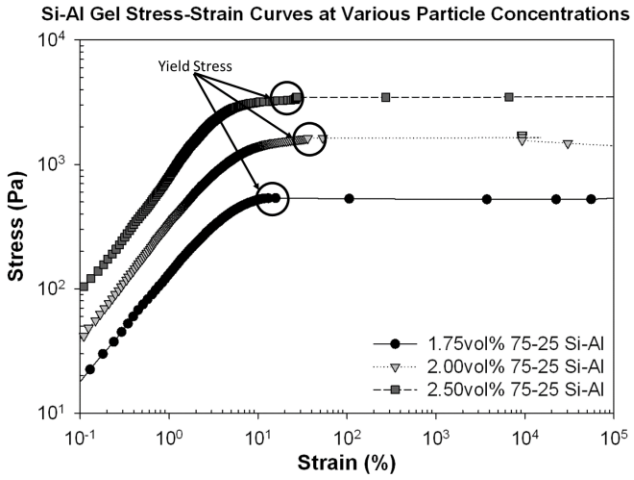


Figure 16. Typical stress-strain data from a yield stress test for silica-alumina gels at various particle volume fractions.

undergoing plastic deformation is quite obvious and can be seen to strongly correlate with particle concentration. The arrows indicate the approximate point where the stress value is sampled during the determination of the yield stress, the maximum stress before an extremely large jump in strain/shear rate.

Table 7 contains the average yield stress and standard deviations for all of the tested gels (entries marked N/A indicate that the sample had either a yield stress below the minimum stress measurable by the instrument (0.06 Pa) or no yield stress at all). Unsurprisingly, the yield stress is strongly affected by the particle volume fraction for all of the different nanoparticle mixtures. None of the 1.0 vol% dispersions have a measurable yield stress. This could be a result of the gels' having a yield stress below the stress minimum of the rheometer (0.06 Pa), but could also be the result of these dispersions being below a 'percolation' threshold or minimum particle concentration required for the heteroaggregated nanoparticles to form a volume-spanning network throughout the fluid. The latter is the case based on observations that the 1.0 vol% dispersions have a tendency to settle into an opaque dispersion phase and a clear supernatant phase without any centrifugation. All of the nanoparticle mixtures at concentrations, pHs, and particle ratios that result in yield

Table 7. Yield stress values for gels made with various particle mixtures, ratios, and concentrations. Values were determined by taking the average yield stress of a series of five stress ramp experiments.

Yield Stress Values		
Silica-Alumina, pH=7		
Particle Concentration	SiO_2-Al_2O_3 Ratio	Yield Stress, Pa
1.0 vol%	75-25	N/A
1.5 vol%	75-25	24±2
1.6 vol%	75-25	38±3
1.75 vol%	75-25	58±4
2.0 vol%	75-25	156±17
2.0 vol%	50-50	53±2
2.0 vol%	25-75	3±0.1
2.5 vol%	75-25	358±24
3.0 vol%	75-25	451±29
Silica-Titania, pH=5		
Particle Concentration	SiO_2-TiO_2 Ratio	Yield Stress, Pa
1.0 vol%	75-25	N/A
1.5 vol%	75-25	33±6
2.0 vol%	75-25	143±21
2.0 vol%	50-50	35±5
2.0 vol%	25-75	82±23
2.5 vol%	75-25	289±25
Titania-Alumina, pH=7		
Particle Concentration	TiO_2-Al_2O_3 Ratio	Yield Stress, Pa
1.0 vol%	50-50	N/A
1.5 vol%	50-50	52±8
2.0 vol%	75-25	157±27
2.0 vol%	50-50	130±7
2.0 vol%	25-75	151±8
2.5 vol%	50-50	306±35

stress gels do not sediment in this way under standard gravitational forces for periods as long as at least one year. The effect of particle ratio on yield stress differs depending on the type of nanoparticles used. For all of the tested nanoparticles, 2.0 vol% dispersions of a single type of nanoparticle (100-0 particle ratio) do not exhibit any measurable yield stress. Therefore, all of the metal oxide pairings tested here show a non-linear relationship between particle ratio and yield stress, with some ratio of particles having a 'maximum' yield stress. For gels made with silica and alumina, the highest yield stress was observed at a 75-25 silica-alumina ratio with the observed yield stress dropping significantly as the silica-alumina ratio decreased. The silica-titania and titania-alumina gels, however, present more complicated trends. For the silica-titania gels, the largest yield stress was observed at a 75-25 silica-titania ratio while the 50-50 ratio sample had the lowest yield stress and the 25-75 sample had a yield stress between the two other samples. This unusual behavior may be due to the especially narrow gelation region for silica-titania mixtures, meaning that any minor deviation from the optimum pH could result in a large shift in the amount of surface charge on the particle surface, weakening the interparticle bonds. Meanwhile, the titania-alumina gels' yield stress changes very little as the particle ratio is varied implying that the interparticle bonds differ very little in number or strength over the particle ratios tested. The importance of particle ratio for silica-alumina and silica-titania gels relative to titania-alumina gels could be related to the specific surface charge (charged groups per unit area) of the three different types of particles. Silica has approximately 3 hydroxyl groups/nm^2 while titania and alumina have 6.8 and 8 hydroxyls/nm^2, respectively. Hence, in order to maximize the number of positive-negative pairings it would be necessary to have a silica-titania or silica-alumina ratio of between 2.3:1 and 2.7:1, which are close to the 75-25 silica-titania or silica-alumina ratios where the largest yield stresses are observed. Meanwhile, the specific surface charges of the titania and alumina are much closer to each other, implying that

the 'optimum' particle ratio should be closer to 1:1 and gel strength should not be as strongly affected by shifts away from this optimum; a hypothesis that is in agreement with the yield stress results for the titania-alumina gels shown in Table 7. Overall, these hydrogels exhibit higher yield stresses than fumed metal oxide lyogels because the electrostatic interactions used to stabilize the particle networks are stronger than the hydrogen bonds and van der Waals interactions present in lyogels. Specifically, the 2.5 vol% silica dispersions in methyl laurate had a yield stress of 10 Pa compared to the maximum yield stresses of 358, 289, and 306 Pa measured here for the 2.5 vol% dispersions of silica-alumina, silica-titania, and titania-alumina, respectively.

SHEAR MODULI

Storage and loss moduli (G' and G") were collected at frequencies ranging from 0.006 s^{-1} to 16 s^{-1} for all samples listed in Table 7 and modulus vs. frequency plots are shown in Figure 17. Most of the gels have storage moduli (G') that are larger than their corresponding loss moduli (G"), and a G' that evolves largely independent of frequency. This behavior is consistent with a soft, elastic solid and is comparable to the behavior observed in clay mineral dispersions,[122] nanoparticle/clay mixtures,[123] and other

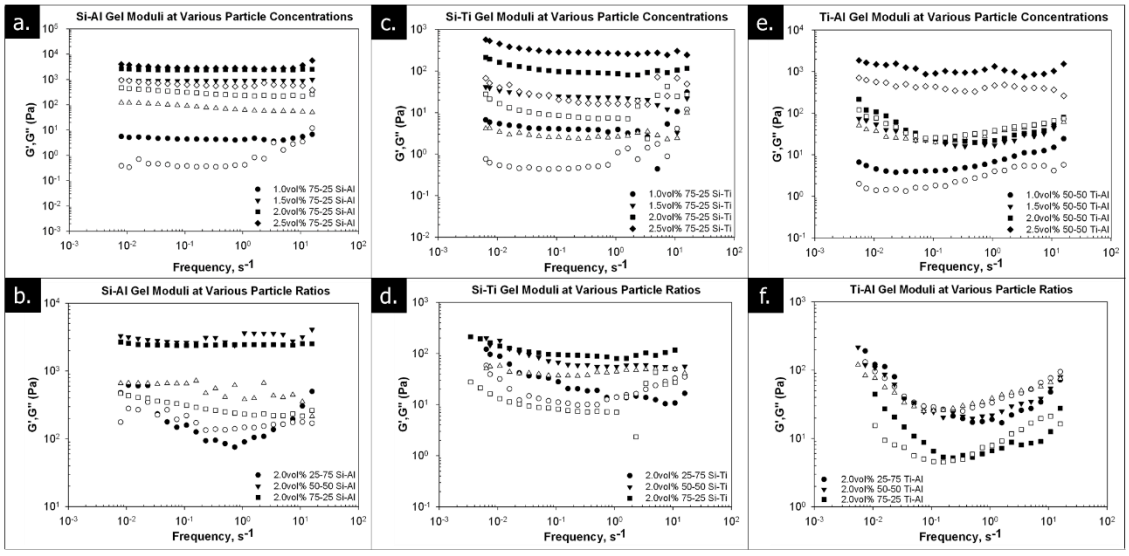


Figure 17. Shear modulus vs frequency plots for silica-alumina (a-b), silica-titania (c-d), and titania-alumina (e-f) gels at various particle concentrations and ratios. Closed symbols represent the storage modulus (G') and open symbols represent the loss modulus (G").

attractive colloidal gels.[124] The elastic moduli for the silica-alumina gel mixtures are roughly an order of magnitude larger than the corresponding silica-titania and titania-alumina gels. This difference is likely explained by the optimum gelation pH for the silica-alumina gels being much farther away from the IEPs of both particles (approx. 2 pH units) than for either of the other nanoparticle mixtures. Since the magnitude of surface charge changes rapidly within two pH units on either side of a particle's IEP, small changes in pH result in a large change of the total surface charge on the nanoparticles, thereby strongly affecting the number of interparticle, electrostatic interactions and overall gel strength. The specific surface charge is strongly affected by the solution pH and when the solution pH is within one pH unit of the IEP, the surface is populated with a mixture of protonated and deprotonated hydroxyls, reducing the total surface charge and limiting the number of electrostatic interactions between oppositely charged particles, likely weakening the gel. This trend in shear modulus of different particle mixtures is in contrast to the yield stress measurements discussed previously, where all of the nanoparticle pairings exhibited approximately similar yield stress values at the same particle concentrations.

Several of the gels with relatively low yield stresses present less solid-like behavior. For instance, the 2.0 vol% 25-75 silica-alumina gel shown in Figure 17b behaves much more viscously than the other silica-alumina gels. G' and G" are not independent of frequency and at high frequencies viscous effects dominate and G'<G" followed by a cross-over point at a critical frequency, ω_c, leading into a region where elastic effects dominate and G'>G". The G'/G" cross-over implies that the gel has a terminal relaxation time on the order of 0.1-0.2 s, where the terminal relaxation time, τ_r, is physically related to the time required for the gel network to rearrange and respond to an applied stress and is defined as $\tau_r=1/\omega_c$.[125] Similar cross-overs are observed for several other gels, in particular, a majority of titania-alumina gels exhibit this type of behavior; their moduli are strongly

dependent on frequency and the G' and G" curves appear much closer together than in the silica-alumina or silica-titania gels. These facts imply that the titania-alumina gels are much more thixotropic than the other gels tested and their viscoelastic behavior will be much more strongly dependent on the timescale of the experiment.

APPARENT VISCOSITY

Apparent viscosities were measured at shear rates ranging from 10^{-6} s^{-1} to 2500 s^{-1}, and Figure 18 contains flow curves that show how gel viscosity profiles change with particle concentration, particle ratio, and solution pH. Gaps or abbreviations in the flow curves are related to one of two experimental limitations; 1) shear rates that require stresses near the yield stress of the gel are very difficult to measure with our equipment and result in noisy, irreproducible viscosity values, and 2) low viscosity fluids cannot be measured at low shear rates because the torque exerted by the fluid is below the minimum measureable torque of the rheometer. All of the gels and particle dispersions display power-law shear-thinning behavior at shear rates below some critical value and therefore lend themselves to analysis using the Ostwald-de Waele[126] (OdW) or Herschel-Bulkley[127] (HB) model for relating viscosity and shear rate. The OdW and HB models both model viscosity and shear rate using a power-law relationship, but the HB model adds an additional term to account for a yield stress, if present. The basic relationship used by both models is:

$$\mu_{app} = K * \left(\frac{d\gamma}{dt}\right)^{n-1} \qquad \text{Eqn. 5}$$

Where μ_{app} is the apparent viscosity, K is a pre-exponential factor commonly referred to as the consistency, $d\gamma/dt$ is the shear rate, and n is exponential term commonly referred to as the power law index. This equation was used to fit the viscosity vs shear rate curves in Figure 18 and the best-fit values for the consistency and power law index parameters for each sample are shown in Table 8 along with the shear rate where the sample

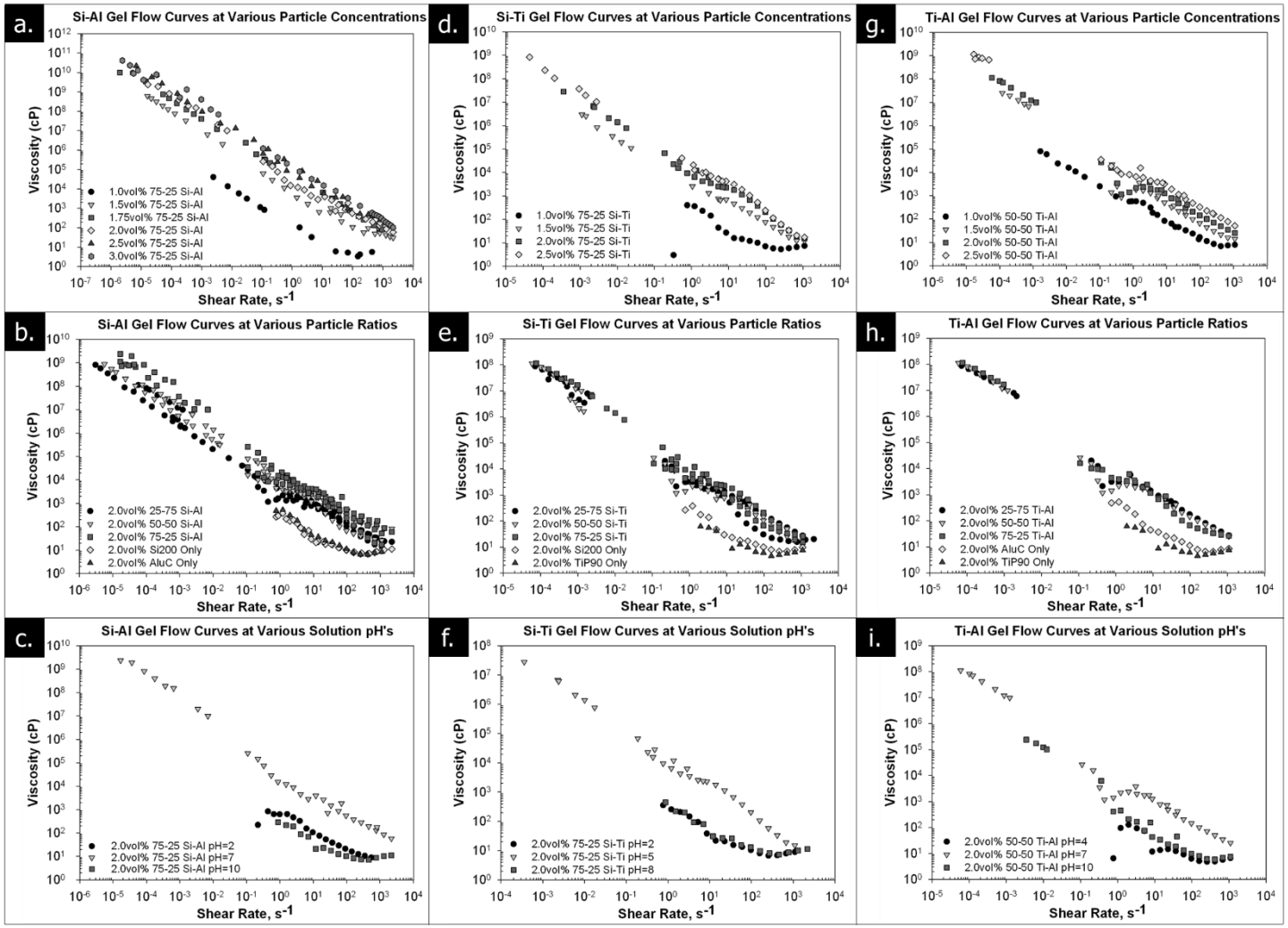


Figure 18. Apparent viscosity vs shear rate plots for silica-alumina (a-c), silica-titania (d-f), and titania-alumina (g-i) dispersions at various particle concentrations, particle ratios, and solution pHs.

transitions from power-law to Newtonian behavior.

Table 8. Ostwald-de Waele and Herschel-Bulkley power law fitting parameters for particle dispersions and colloidal gels, including pre-exponential consistencies, power-law indices, and shear rates where shear-thinning behavior transitions to Newtonian shear-rate independence.

Power Law Fitting Parameters			
Sample	**Consistency (cP)**	**Power Law Index**	**Power-Law to Newtonian Transition (s^{-1})**
Nanoparticle Dispersions			
2.0vol% Aerosil 200	254	0.242	255
2.0vol% TiP90	105	0.356	160
2.0vol% Aeroxide AluC	398	0.202	255
Silica-Alumina Gels			
1.0vol% 75-25 pH=7	199	0.2	150
1.5vol% 75-25 pH=7	13660	0.065	>2200
2.0vol% 25-75 pH=7	6164	0.133	1300
2.0vol% 50-50 pH=7	16001	0.154	1300
2.0vol% 75-25 pH=7	49084	0.015	>2000
2.5vol% 75-25 pH=7	125060	0.014	>2000
2.0vol% 75-25 pH=2	613	0.287	460
2.0vol% 75-25 pH=10	248	0.302	275
Silica-Titania Gels			
1.0vol% 75-25 pH=5	293	0.154	160
1.5vol% 75-25 pH=5	4455	0.096	1050
2.0vol% 25-75 pH=5	4376	-0.019	460
2.0vol% 50-50 pH=5	5160	0.117	1200
2.0vol% 75-25 pH=5	13730	0.033	>2000
2.5vol% 75-25 pH=5	25213	-0.021	>2000
2.0vol% 75-25 pH=2	269	0.27	255
2.0vol% 75-25 pH=8	279	0.338	450
Titania-Alumina Gels			
1.0vol% 50-50 pH=7	550	0.264	415
1.5vol% 50-50 pH=7	5161	0.051	>2000
2.0vol% 25-75 pH=7	12291	0.057	>2000
2.0vol% 50-50 pH=7	10652	0.049	>2000
2.0vol% 75-25 pH=7	7764	-0.017	>2000
2.5vol% 50-50 pH=7	18851	0.053	>2000
2.0vol% 50-50 pH=4	164	0.316	255
2.0vol% 50-50 pH=10	798	-0.014	255

The data in Table 8 lends itself to a few generalizations about the gel behavior. First, the 'strength' of the gel can be approximated by the consistency value, which agrees with previous results in that the silica-alumina gels have a much higher viscosity than the corresponding silica-titania and titania-alumina gels. Consistency values also reinforce the previous trends noticed regarding particle ratio, with consistency being a strong function of particle ratio for silica-containing gels, but less of a factor for the titania-alumina gels. A similar trend is observed with power-law index values, where stronger gels and increased network strength results in indices close to zero, while samples at low concentrations and pH outside of the gelation window display power-law indices in the range of 0.2-0.3, which is similar to the indices observed for dispersions of only a single species of fumed nanoparticle. Four of the tested gels have power-law indices that are <0, a property that is not theoretically possible, but has been observed in a variety of biomass dispersions.[128,129] Padmanabhan theorized that the negative indices were a result of some combination of molecular degradation of the sample, viscous dissipation, and

fluid slip. Since molecular degradation of the fumed metal oxide nanoparticles is certainly not occurring at these shear rates and stresses, the negative indices observed here are therefore likely due to viscous dissipation and wall slip; however, non-linear degradation of particle agglomerates could also be a contributing factor.

The particle mixtures demonstrate a very strong and reversible relationship between viscosity and solution pH, as shown in Figure 18c, f, and i. The apparent viscosity drops by two orders of magnitude or more when the solution pH is pushed below or above the IEPs of both of the metal oxides. Similar behavior has been observed in clay dispersions where the various facets of the clay particle have different IEPs[130] and in alumina dispersions near the IEP, where positively charged and negatively charged surface groups coexist and maximize interparticle electrostatic interactions.[131] In addition to the large drop in viscosity, the low- and high-pH dispersions do not exhibit a yield stress, implying that there is no long range structure present.

Since all of the tested dispersions at a pH within the gelation window display power-law behavior and have similar power law exponents, it was hoped that there would be a single descriptive factor that could relate how the viscosity profile changes for different particle mixtures, concentrations, and ratios. Figure 19a shows a combined viscosity profile for all of the samples that exhibited gel-like behavior after being

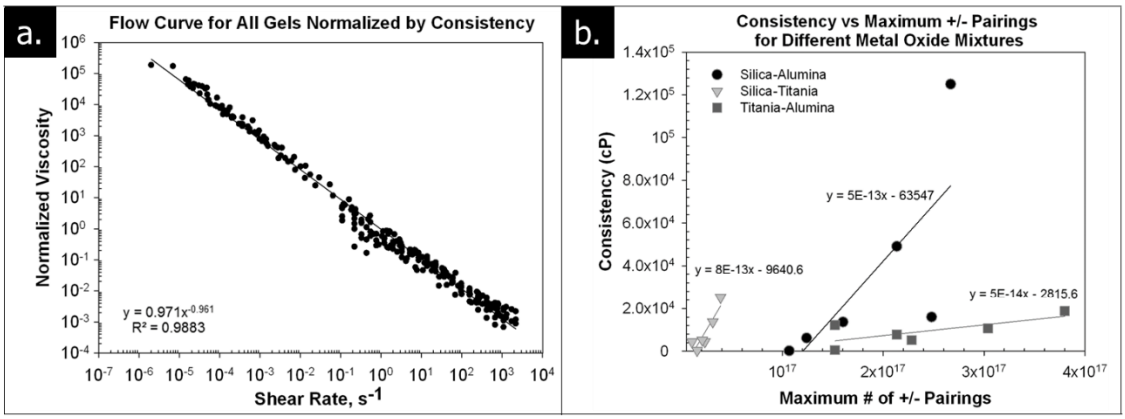


Figure 19. Normalized viscosity vs shear rate plot (a) and consistency vs max. +/- pairings plot (b) for all gels that exhibit yield stress behavior. Viscosities were normalized using the fitted consistency value found in Table 8.

normalized using the consistency values reported in Table 8. The normalized viscosity data for all of the samples collapses onto a single power-law profile with a minimal amount of scatter, as the slight variations in power law index from sample to sample would suggest. If a single variable or set of variables could be found that relate each gel sample to its measured consistency, it would allow us to predict viscosity profiles for other particle mixtures. One possible parameter would be the maximum number of +/- pairings in a given gel mixture, since the number of interparticle bonds should, in theory, be strongly correlated to the overall strength of the particle network and its viscoelastic behavior. A value for the maximum number of +/- pairings can also be easily calculated using the specific surface charges reported in the literature. However, a plot of consistency vs max. number of +/- pairings, shown in Figure 19b, shows that there is no overall correlation between the two across different nanoparticle pairings, though within each pairing there is a decent correlation between the two variables. Hence, additional factors must exist that are important to understanding the gel structure and behavior for the different nanoparticle pairings beyond a simple charge balance between negatively charged surface sites and positively charged surface sites. Other potential factors may be sintered aggregate size, aggregate fractal dimension, relative polydispersity of the aggregates, etc.

CONCLUSIONS

This work demonstrates that mixing different species of fumed metal oxide nanoparticles with some fractal structure at certain particle ratios and pH allows for the spontaneous generation of a volume-spanning particle network via electrostatic interactions. The gels exhibit solid-like behavior when total particle volume fractions are greater than 0.015 and the total number of positively-charged and negatively-charged surface sites are approximately equal, but exhibit increasingly viscous behavior upon deviation from either of those two requirements. This result is in agreement with the

work of both Rasa and Binks who showed that heteroaggregation was maximized when the charge ratios were approximately the same for similar particles. Additionally, the pH ranges where the gelation phenomenon is observed closely matches the pH values where Binks, Kim, Rasa, and Lopez-Lopez observed flocculation and sedimentation, implying that both phenomena may be the result of heteroaggregation of oppositely charged particles in aqueous solution. We believe gelation was observed here while sedimentation was observed in those other studies because the nanoparticles used by Binks, Kim, Rasa, and Lopez-Lopez were synthesized using a precipitation method,[132] rather than the pyrolytic method used to synthesize fumed metal oxide nanoparticles. Precipitated metal oxides tend to form well-dispersed, individualized, spherical particles rather than fractal, sintered, nanoparticle aggregates as obtained from pyrolytic methods. The multi-dimensional rigidity created by the fractal structures of the fumed nanoparticles generates an obstacle to the formation of dense aggregates.[133]

Once formed, the nanoparticle networks are responsible for the fluid acquiring a yield stress and power-law shear-thinning behavior. This behavior is similar to that of other fractal particles dispersed in non-polar solvents, but these hydrogels exhibit higher yield stresses, viscosities, and elastic moduli than the lyogels because the electrostatic interactions used to stabilize the particle networks are stronger than the hydrogen bonds and van der Waals interactions present in other fractal gels.

The apparent viscosity of the gels can be modeled accurately using the Ostwald-de Waele power law relationship between shear rate and viscosity. Gel consistencies are roughly correlated to particle concentration and the number of +/- surface charge partners within each nanoparticle pairing, but no obvious relationship tying the viscosity profiles of all of the different nanoparticle pairings was found. Finally, the viscoelastic behavior of these gels can be easily controlled by varying the solution pH above or below the isoelectric points of the two particles.

CHAPTER 5: SMALL ANGLE NEUTRON SCATTERING OF PSEUDO-SOLID, SHEAR-THINNING BINARY MIXTURES OF FUMED METAL OXIDE NANOPARTICLES AT LOW VOLUME FRACTIONS

INTRODUCTION

Small-angle scattering (SAS) is a powerful technique that can be used to characterize the nanoscale structure of a number of materials, including metal alloys,[134] surfactant micelles,[135] colloidal dispersions,[136,137] proteins,[138] and block co-polymers.[139] Small-angle scattering can also be used in conjunction with rheometers to gain information regarding how the structure of colloid, polymer, and protein dispersions changes when the fluid is undergoing flow at a variety of shear rates.[140,141] SAS experiments can be carried out using a variety of radiation sources, with the most commonly used being light (SALS), x-rays (SAXS), and neutrons (SANS). Each of these radiation sources offers different benefits and drawbacks, for example neutrons provide excellent penetration of thicker or more concentrated samples and contrast matching techniques are possible, but are generally operated at much lower fluxes, meaning each experiment takes a longer period of time to complete.

The first installment of this series mapped the gelation phase boundaries for mixtures of silica/titania, silica/alumina, and titania/alumina at various particle species ratios and volume fractions, and showed that the gels can be reversibly broken and reconstructed by varying pH.**Error! Bookmark not defined.** As discussed in both apers, in most situations where oppositely charged particles are mixed the dispersion is unstable and the particles precipitate or sediment; our belief is that the fractal nature of the individual metal oxide particles prevents dense particle packing, which results in gelation rather than sedimentation. Some limited structural information from SAXS was previously presented in the first paper, however because of the small angular region sampled and the fact that the scattering contribution of each particle species was a strong

function of the volume fraction, very limited information could be obtained using this technique. The second article of this series investigated and quantified the rheological properties of the nanoparticle gels including viscosity vs shear rate, shear moduli vs. frequency and yield stress results. For a given particle pairing, a universal scaling law based on the total number of +/- surface charge pairings provided a reasonable description of viscosity vs shear rate curves. The maximum yield strength of gel was found to occur at the volume fraction ratio of the two particles where the total numbers of positive and negative surface charges were roughly balanced. Further, the measured yield strengths, storage moduli, and viscosities of the electrostatic gels were approximately a factor of ten higher than the corresponding properties of similar gels where the interparticle attraction was driven by hydrogen bonding, roughly matching the differences between a hydrogen bonding force and an electrostatic force. In this work, we characterize the nanoscale structure of the silica/alumina gels using small-angle neutron scattering and show how the nanoparticle network changes as a function of particle concentration, solution pH, and ratio of positively charged particles to negatively charged particles. Contrast matching is used to examine each particle species individually; to our knowledge this study is the first time where this approach has been used for these types of gels.

EXPERIMENTAL

MATERIALS

The nanoparticles used in this study, Aerosil 200 and Aeroxide Alu C, were obtained from Evonik. Aerosil 200 (Si200) is a fumed silica nanoparticle with an average primary particle size of 12 nm, specific surface area of 200±25 m^2/g, IEP of pH=4.0, an average of 3 surface hydroxyls per nm^2,[142] and an average fractal dimension of 2.22. Aeroxide Alu C (AluC) is a fumed alumina nanoparticle with an average primary particle size of 13 nm, specific surface area of 100±15 m^2/g, IEP of pH=8.5, an average of 8

surface hydroxyls per nm^2, and an average fractal dimension of 2.06. Fractal dimensions were determined using SANS data described in this paper. The sintered fractal aggregates for all of the nanoparticles used, which cannot be broken down, range from ~30-250 nm in size, as determined by TEM and Acoustic Spectroscopy. When calculating nanoparticle volume fractions, the density of the nanoparticles was assumed to be that of bulk, amorphous silica (2.25 g/cm^3) and alumina (3.85 g/cm^3), values which are comparable to those found in the literature for other fumed metal oxide nanoparticles.[143,144]

De-ionized water with a conductivity of < 2 μS/cm was used for preparing aqueous dispersions and obtained using a polymer ion-exchange filtration system. All pH adjustments were made with 10 wt% NaOH and HCl in order to prevent excessive dilution of the nanoparticles. Sodium hydroxide and hydrochloric acid were both purchased from Fischer Scientific. Deuterium oxide, D_2O, > 99.0 atom % D was obtained from Sigma-Aldrich.

Gels were prepared by weighing out the desired amount of each particle, as determined by converting wt % into vol % using the previously enumerated nanoparticle densities, into a container along with the necessary amount of deionized water. Then, the particles were initially dispersed in the aqueous phase using a vortex mixer followed by an initial pH adjustment to the desired pH. Three pHs were used for each nanoparticle pairing: a pH below the isoelectric points of both particles, a pH in the center of the gel region between the two particles' isoelectric point, and a final pH above the isoelectric point of both particles. Next, the particle dispersions were sonicated using a Fisher Scientific FB505 horn sonicator with a 1/8 inch stainless steel tip for 9 minutes at 40% amplitude in order to break up particle agglomerates. Following sonication, the solution pH was checked a second time and, if changed due to protonation/deprotonation of surface hydroxyls, adjusted to the desired pH using NaOH and HCl. For brevity, all

subsequent uses of the unit '%' refer to volume percent and any use of mol % or wt % will be clearly stated.

METHODS

Small-angle neutron scattering experiments were carried out at two different locations. Initial experiments were completed on the NG-7 30 m SANS instrument at the NIST Center for Neutron Research (NCNR) located in Gaithersburg, MD.[145] Neutron wavelengths of 8.0 Å were used along with sample-to-detector distances varying from 1.0 - 15.0 m to obtain scattering data over the scattering vector range of 0.01298 nm^{-1} < q < 3.8 nm^{-1}, where ($q=4\pi\sin\theta/\lambda$) with 2θ is the solid angle between the incident radiation beam and the detector and λ is the wavelength of the incident radiation. Further experiments were completed on the BL-6 EQ-SANS instrument at the Spallation Neutron Source (SNS) within Oak Ridge National Laboratory.[146] Neutron wavelengths of 3.0 – 15.0 Å were used along with sample-to-detector distances varying from 3.0 - 9.0 m to obtain scattering data over the scattering vector range of 0.01857 nm^{-1} < q < 1.4 nm^{-1}.[147] All experiments at both locations were carried out using sealed quartz window cells with a 1 mm sample path length. Raw pinhole-collimated two-dimensional scattering data were reduced to q vs I plots using software developed at NCNR and ORNL. Data was reduced using standard procedures implemented through Igor macros[148] or MantidPlot[149] to correct for background scattering, neutron time-of-flight, detector dark current, detector sensitivity, and a variety of other factors. The reduced scattering profiles were then fit using the SasView fitting software[150] and all results were fit using the Unified Power Law Scattering model developed by Beaucage, as shown in Equation 6.[151,152] The first term describes the exponential decay in scattering at a characteristic feature size, R_{gi}, and the second term describes

$$I(q) = \sum_{i=1}^{n} G_i \exp\left(\frac{-q^2 {R_{gi}}^2}{3}\right) + B_i exp\left(\frac{-q^2 {R_{g(i+1)}}^2}{3}\right)\left[\frac{\left(\mathrm{erf}\left(\frac{qR_{gi}}{\sqrt{6}}\right)\right)^3 \mathrm{erf}}{q}\right]^{Pi} \quad \text{(Eqn. 6)}$$

the power-law decay in scattering that follows the exponential region, with Pi indicating the fractal dimension for the feature sizes between R_{gi} and $R_{g(i+1)}$.

Electron microscopy images were obtained using a JEOL 2000-FX transmission electron microscope and a Zeiss NEON 40 EsB scanning electron microscope. Energy dispersive x-ray spectroscopy (EDS) was carried out using a Kevex Quantum 10 mm^2 x-ray detector, which was also used in conjunction with an IXRF x-ray analyzer to complete EDS mapping of samples. Samples were prepared for TEM study by dispersing particles in LR White, a hydrophilic resin solution, at a 75:25 silica:alumina ratio and total particle concentration of 2.0 vol %; a ratio and concentration that was known to form a gel in an aqueous solution. The resin was then polymerized into a solid by placing the sample into a 40 ^oC oven for 48 hours in a tightly sealed gelatin capsule. The solidified polymer-nanoparticle composites were then removed from the gelatin capsules and 50-100 nm slices were removed from the sample using a Reichert UltraCut E ultramicrotome. The thin sections were then placed on a C-flat holey carbon TEM grid for imaging. These thin sections were used for high-resolution imaging, EDS, and elemental mapping of the gel network. Previous small-angle x-ray scattering experiments showed that the particle networks were consistent in the polymer resin and aqueous solution over the length scales that can be probed using SAXS and are assumed to be approximately representative of the gel structure present in aqueous dispersions.

Gel illustrations were created using a combination of software programs and were based on the fractal dimensions and radii of gyration information obtained from model fitting of SANS data. The NetLogo software package[153] and its three-dimensional diffusion limited aggregation model were used to generate xyz coordinates for fractal

aggregates with fractal dimensions varying from 1.6-2.3; the fractal dimensions of generated aggregates were evaluated using a standard box-counting method.[154] The xyz coordinates were then exported to the 3-D visualization software package, VESTA,[155] where structural models of the 'hard' fractal aggregates present in fumed metal oxides were made using simple spheres to represent the primary particles. A series of 5 'base' particles were generated in this manner for both Aerosil 200 and Aeroxide AluC. These base particles were created in a way so that their structure corresponded to the correct primary particle size, fractal dimension, and hydrodynamic diameter for Aerosil 200 and Aeroxide AluC as determined by our own SANS experiments and other literature sources that have characterized these nanoparticles.[156,157,158] These primary particles were then arranged into a three-dimensional fractal aggregate with the correct fractal dimension, etc. using NetLogo to generate unit cell xyz coordinates for particles within the aggregate, VESTA for visualization of the final structure, and Packmol software[159] to randomly populate the xyz coordinates with the previously generated alumina and silica 'base' particles. Final structures were then exported as high resolution raster images of the aggregate structure using VESTA.

RESULTS AND DISCUSSION

A major advantage of neutron scattering over x-ray scattering in studying these gels is the large difference in scattering length density between hydrogen (H) and deuterium (D). Hence, the contrast in aqueous dispersions can be varied by changing the H_2O to D_2O ratio so that the scattering length density of the water is matched to the scattering length density of one of the dispersed components and hence the scattering profile is only that from the other dispersed components, a method called solvent or contrast matching. In this case, contrast matching allows separate scattering profiles for the silica and the alumina nanoparticles in addition to a scattering profile for the combined gel network structure. Preliminary scattering length density calculations

indicated that SiO_2 should have a contrast match point of ~68 mol % D_2O/32 mol % H_2O and Al_2O_3 should have a contrast match point of ~90 mol % D_2O/10 mol % H_2O. More precise contrast match points were obtained by running a series of contrast variation experiments at NCNR. Aerosil 200 particles and Aeroxide AluC particles were dispersed separately in a series of aqueous solutions at five different D_2O/H_2O ratios focused around the theoretical match points. Scattering profiles were obtained for each of these dispersions and the 'contrast' of each sample was determined by subtracting the scattering intensity (I) at a scattering vector (q) value of 1.0 nm^{-1} from the scattering intensity at q = 0.1 nm^{-1}. The measured contrast values were then plotted against the D_2O/H_2O ratio for each sample and fitted to a 2nd degree polynomial. Finally, the fitted polynomial was solved for its minimum value and that D_2O/H_2O ratio was used as the contrast match point for each nanoparticle species. These experiments resulted in a contrast match point of 62% D_2O for Aerosil 200 and 88% D_2O for Aeroxide AluC.

Previous work has demonstrated that the gelation phenomenon observed in these nanoparticle mixtures is caused by electrostatic heteroaggregation of silica and alumina. However, at this point it is unclear which of two potential mechanisms is responsible for the behavior. Several literature articles have studied the methods required to fully

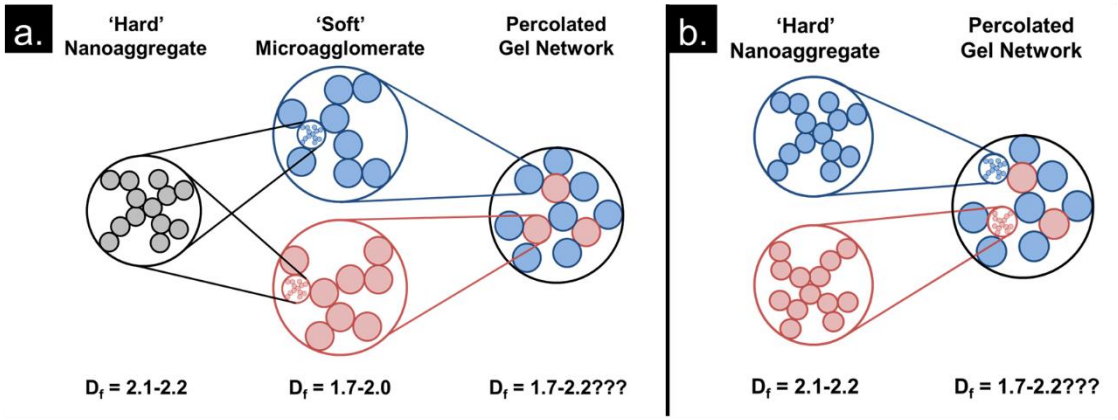


Figure 20. Illustration demonstrating the two possible gelation mechanisms in electrostatically-driven heteroaggregation gels. Fig. 1a. displays a gel network generated via heteroaggregation of microagglomerates and Fig. 1b. displays a network generated via heteroaggregation of fully dispersed nanoaggregates. In this illustration blue and red are used to indicate aggregates and agglomerates of silica and alumina, respectively.

disperse fumed metal oxide nanoparticles in polar and non-polar solvents.[160,161,162] These studies have shown that, when dispersed via shaking and/or vortex mixing, many 'soft' particle agglomerates cannot be broken up into their constituent 'hard' sintered aggregates. However, ultrasonication and high-pressure homogenization has been shown to impart sufficient energy to fully disperse the particles, breaking up all multi-aggregate agglomerates. The gels studied here were ultrasonicated prior to experimentation under the same conditions where full dispersal of both Aerosil 200 and Aeroxide AluC individual particles has been achieved as described later in more detail. However, additional viscous forces generated by gelation prior to full dispersal could possibly absorb a large enough fraction of the sonic energy to prevent full dispersal of the sintered aggregates in the studied gels.

Figure 1 illustrates the two different gelation mechanisms possible in the gels studied here. Fig. 1a. illustrates a 'microagglomerate' heteroaggregation mechanism where ultrasonication of the nanoparticle dispersions fails to fully break apart the 'soft' agglomerates into the 'hard' nanoaggregates. Despite incomplete dispersion, the silica and alumina microagglomerates will still be oppositely charged at neutral pH and undergo electrostatic heteroaggregation into a percolated gel network that spans the entire continuous phase, resulting in the observed yield stress and viscoelastic properties. In theory, the size of the microagglomerates could vary in size from large agglomerates several microns in diameter to smaller agglomerates of a just a few nanoaggregates and cluster diameters of < 1 μm, depending on the ability of the sonicator to impart kinetic energy to the large agglomerates. Figure 1b illustrates the final gel network expected if complete dispersion of the nanoaggregates is achieved, with electrostatic repulsion largely preventing self-association of the silica and alumina and attractive electrostatic forces binding the oppositely charged particles into a fractal network. The gels could also exist in a state somewhere between those shown in Fig. 1a.

and 1b., with the dispersion consisting of a mixture of microagglomerates and nanoaggregates simultaneously interacting to result in the observed rheological behavior.

An initial study of Aerosil 200-only and Aeroxide AluC-only dispersions was carried out to confirm that the sonication method used for the binary gel mixtures was sufficient to fully disperse the particles in water and to determine the characteristics of the pure particles. The scattering curves for those dispersions are shown in Figure 2. Aerosil 200-only scattering was performed at the Aeroxide AluC contrast match point and vice versa. In Fig. 2, it can be seen that the scattering curve undergoes a transition from power law scattering towards q-independent (q^0) scattering. This transition indicates that there are no ordered structures with sizes larger than the feature size probed by this scattering vector (approx. 200 nm). These results are consistent with aggregate sizes observed via electron microscopy and by others[156,158,163] using small-angle scattering and dynamic light scattering. All of these results indicate that the

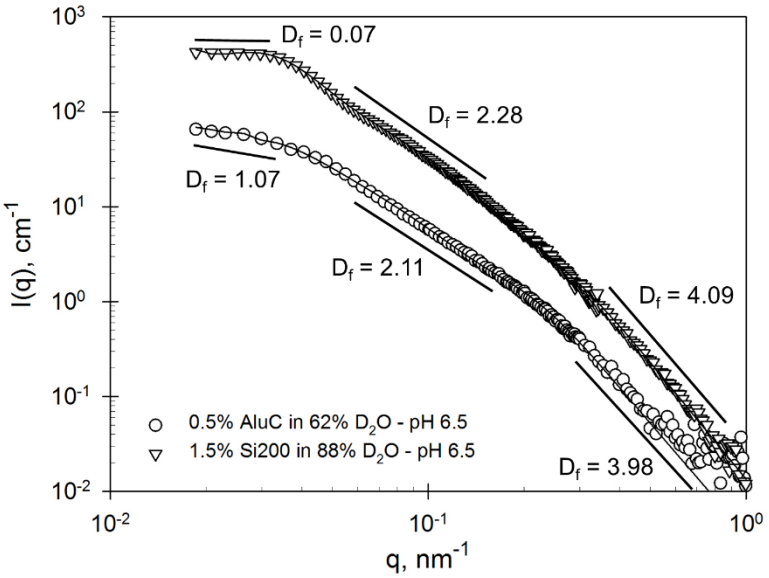


Figure 21. Scattering curves for dispersions of Aerosil 200 at the alumina contrast match point and Aeroxide AluC at the silica contrast match point. Best fit lines for a Unified Power Law model are shown for each curve.

microagglomerates in the dispersions containing only one particle or the other can be fully broken up using the same sonication procedure used to prepare the gels.

A non-contrast-matched scattering profile of the overall gel structure shown in Figure 3 was obtained after forming 75:25 Si200:AluC gels in 100 mol % D_2O, pH of 6.5 and two different total particle concentrations. The background scattering length density is sufficiently far from those of silica and alumina to get scattering from both particle types, and incoherent scattering from hydrogen is minimized. A strong gel (yield stress of 156 Pa) exists for the high concentration sample, while the low concentration sample exhibits no yield stress behavior. The scattering profile for both samples contains three different power law regimes: 1) at large scattering vectors ($q > 0.4$ nm^{-1}), scattering intensity follows a q^{-4} relationship, implying scattering from smooth three-dimensional objects; 2) at intermediate scattering vectors (0.06 nm$^{-1} < q < 0.13$ nm^{-1}), scattering intensity follows an $\sim q^{-2.18}$ relationship, implying scattering from mass fractal particles with a

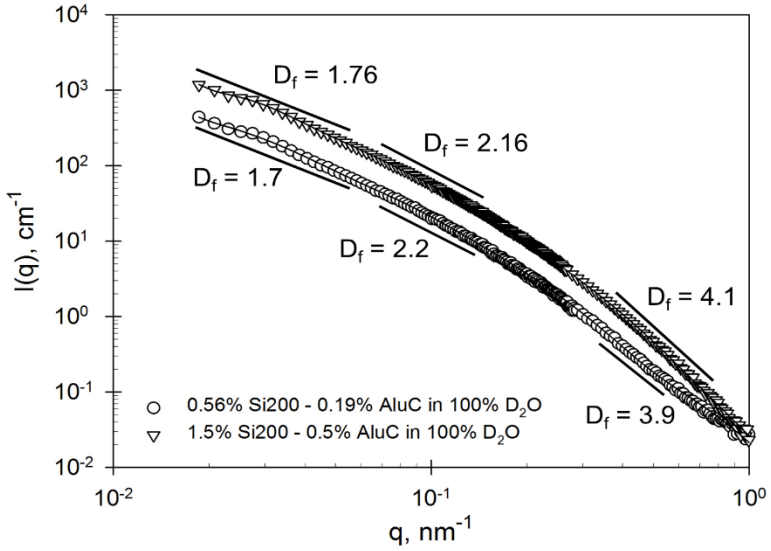


Figure 22. Scattering profiles of the overall gel structure for two Aerosil 200:Aeroxide AluC dispersions at the particle ratio and pH where gel strength is maximized. One sample is below the critical gelation concentration, the other is above the gelation concentration and exhibits a yield stress. Fractal dimensions obtained through fitting the data to a Unified Power Law model are displayed, and the solid lines illustrate the best fit line of the model.

fractal dimension (D_f) ≈2.18; 3) at sufficiently small scattering vectors (0.015 nm^{-1}< q < 0.05 nm^{-1}), scattering intensity follows an ~$q^{-1.73}$ relationship, implying scattering from a more diffuse mass fractal agglomerate with D_f ≈1.73. These three regimes are believed to correspond to scattering from the spherical primary particles (1), the sintered, 'hard' nanoagglomerates (2), and either the microagglomerates or the percolated gel network (3); in a structure roughly analogous to that observed by Schaefer in studies of silica-reinforced elastomers.[164] Compared to the scattering from the pure particles, the composite scattering pattern has the expected slopes at intermediate and high scattering vectors; with the former being intermediate between the two individual particles. The scattering profiles of the low and high concentration gels are extremely similar, with the only major difference being an upward shift in overall scattering intensity. This shift implies an increase in the number concentration of scattering objects in the beam path, a logical outcome from increasing the total particle concentration. However, the fractal dimensions of the two samples at small q's remain relatively constant, suggesting that the additional nanoparticles present at the high concentration are not being packed into the existing structure of the lower concentration sample, but rather being added to interstitial spaces beyond the range of feature sizes that can be studied with these SANS experiments (in this case, feature sizes < ~500 nm). Since the rheological characteristics of the two samples are extremely different while the scattering profiles are quite similar, these results seem to indicate that the particle network imparting yield stress behavior to the gels consists of subunits that are larger than ~500 nm maximum feature size explored by SANS, perhaps in a network similar to that observed in certain clay suspensions.[165] At this time, it is unclear what produced the small scattering feature at q ≈0.03 nm^{-1}, but it does not appear on subsequent scattering curves obtained at the silica and alumina contrast match points, so it may be an artifact.

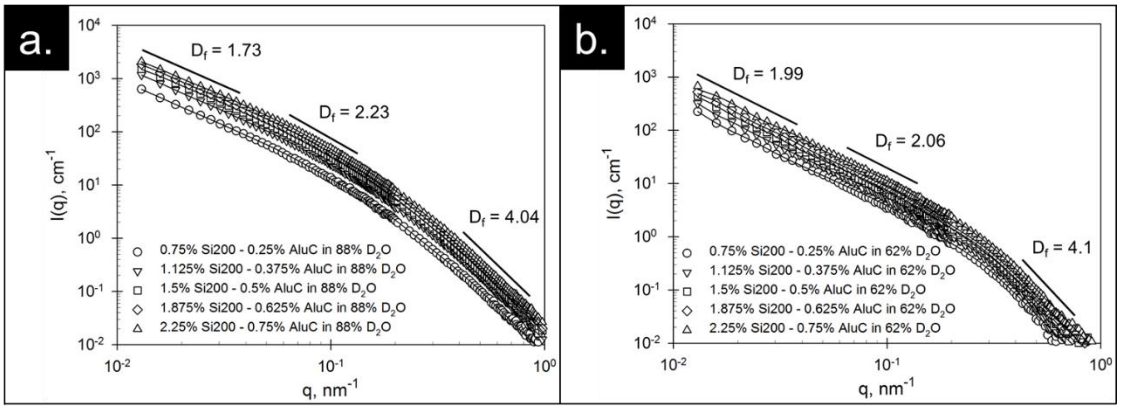


Figure 23. Scattering curves for contrast-matched gels at a series of total particle concentrations and a constant particle ratio and solution pH of 75:25 Si200:AluC and 6.5, respectively. Figs. 3a. and b. contain data taken from gels suspended at the alumina contrast match point and silica contrast match point, respectively. Best fit lines for a Unified Power Law model are shown for each curve.

Figure 4 contains scattering curves for contrast-matched gels with a variety of total particle concentrations and a constant particle ratio (75:25 Si200:AluC) and solution pH (6.5). Fig. 4a. contains scattering curves from the alumina contrast match point, i.e. sample scattering comes from the dispersed Si200 nanoparticles, while Fig. 4b contains scattering curves obtained at the silica contrast match point, i.e. sample scattering comes from dispersed AluC nanoparticles. Again, the shape of the scattering curve for both the silica-matched and alumina-matched samples are very consistent throughout all of the tested particle concentrations, with only the overall scattering intensity being affected by the increase in nanoparticle concentration, as in the 100% D_2O samples.

At the alumina contrast match point, the sample scatters in a manner similar to the 100% D_2O gels shown earlier, and has three relatively distinct power law scattering regions corresponding to primary particle, nanoaggregates, and microagglomerate scattering with average fractal dimensions of 4.04, 2.23, and 1.73, respectively. The first two fractal dimensions correspond very closely to those measured in the Aerosil 200-only dispersions. The slope of these scattering curves at low q appears to indicate that the silica nanoaggregates are not fully dispersed because, since the rheological properties of

the gels change significantly over the concentration range shown (gels with 1.0% total particle concentration exhibit no yield stress while 2.5% gels have yield strengths of ~360 Pa), the gel network must be changing. If the network is changing but the low-q fractal dimensions does not change, the 'gel network' must be constructed of interacting constituents larger than the largest feature size probed in these SANS experiments which is ~500 nm. In other words, if these samples were constructed of direct heteroaggregation of the nanoaggregates and the gel network is self-similar over larger length scales, the fractal dimension observed at scattering vectors corresponding to feature sizes larger than the nanoaggregates ($q < 0.03$-0.06) should respond to increases in concentration due to tighter packing of the nanoparticle network, which did not occur. Therefore, it is probable that the nanoaggregates remain at least semi-agglomerated into microagglomerates with $D_f \approx 1.73$ and diameters of at least 485 nm (the feature size corresponding to the smallest scattering vector where data was collected).

The Aeroxide AluC scattering data obtained at the silica contrast match point seems to contain only two distinct power law regions, though the data was still fit using a three-level Unified Power Law model for consistency. Similar to the Aerosil 200-only scattering, Fig. 4b. suggests that the alumina nanoaggregates have not been fully dispersed following the sonication protocol used in this study based on the same reasoning of no change in fractal exponent at low q with a significant change in rheological response. The Aeroxide AluC appears to consist of microagglomerates with $D_f \approx 1.99$ and, again, a minimum agglomerate diameter of 485 nm.

The Unified Power Law fitting results (see Table 1) for the scattering data shown in Fig. 4 indicate that the Aerosil 200 consists of primary particles with an average radius of 10 ±1 nm and nanoaggregates with an average D_f of 2.23 ± 0.03 nm and an average radius of gyration of 82±10 nm. Meanwhile, the Aeroxide AluC consists of primary particles with an average radius of 13 ± 2 nm and nanoaggregates with an average D_f of 2.07 ±

0.05 nm and an average radius of gyration of 101 ± 60 nm. All of these fitted values are consistent with previously cited characterization studies as well as our SANS measurements on the pure particles. Within the fitting results shown in Table 1, one would expect that R_{g3} (radius of spherical primary particles), P3 (fractal dimension of primary particles), R_{g2} (radius of gyration of the 'hard' nanoaggregates), and P2 (mass fractal dimension of the 'hard' nanoaggregates) to remain the same for both the Aerosil 200 and Aeroxide AluC regardless of total particle concentration, pH, particle ratio, etc; and the results in Table 1 agree with this expectation. The fitting results shown in Table 1 also show very little change in the value of P1 (fractal dimension for the gel network) for all of the gel samples, in agreement with the idea that the nanoaggregates remain partially agglomerated. Table 1 does not show values for R_{g1} because the scattering results shown here do not go to low enough values of q to definitively provide any information on the radius of gyration of the gel network's subunits.

Table 9. Unified Power Law fitting results for radius of gyration (R_g) and fractal dimension parameters for all scattering data presented in this study. P1 is the fractal dimension of the 'soft' microagglomerates, R_g2/P2 are the corresponding parameters for the 'hard' nanoaggregates, and R_g3/P3 are the corresponding parameters for the spherical primary particle scattering, respectively. **Note:** R_g values are provided in units of nanometers.

Unified Power Law Fitting Parameters					
Sample	**R_g3**	**R_g2**	**P3**	**P2**	**P1**
Varying Concentration					
0.75% Si200 - 0.25% AluC - 88% D_2O - pH 6.5	9.8	82.4	4.08	2.22	1.76
1.125% Si200 - 0.375% AluC - 88% D_2O - pH 7.0	10.9	83.5	4.01	2.23	1.77
1.5% Si200 - 0.5% AluC - 88% D_2O - pH 6.5	10.2	76.9	4.06	2.22	1.70
1.875% Si200 - 0.625% AluC - 88% D_2O - pH 7.0	10.7	79.5	4.01	2.23	1.73
2.25% Si200 - 0.75% AluC - 88% D_2O - pH 7.0	10.1	75.8	4.06	2.23	1.70
0.75% Si200 - 0.25% AluC - 62% D_2O - pH 6.5	14.7	143.3	4.02	2.07	1.92
1.125% Si200 - 0.375% AluC - 62% D_2O - pH 7.0	13.7	240.5	4.16	2.07	1.97
1.5% Si200 - 0.5% AluC - 62% D_2O - pH 6.5	14.4	112.8	4.03	2.03	2.00
1.875% Si200 - 0.625% AluC - 62% D_2O - pH 7.0	13.3	99.9	4.22	2.04	2.06
2.25% Si200 - 0.75% AluC - 62% D_2O - pH 7.0	13.9	90.0	4.10	2.06	2.01
Varying Particle Ratios					
0.5% Si200 - 1.5% AluC - 88% D_2O - pH 8.5	12.1	110.1	3.95	2.25	1.95
1.0% Si200 - 1.0% AluC - 88% D_2O - pH 7.0	9.8	73.1	4.03	2.25	1.82
1.5% Si200 - 0.5% AluC - 88% D_2O - pH 6.5	10.2	76.9	4.06	2.22	1.70
0.5% Si200 - 1.5% AluC - 62% D_2O - pH 8.5	13.8	29.6	4.03	2.06	2.16
1.0% Si200 - 1.0% AluC - 62% D_2O - pH 7.0	13.6	78.0	4.16	2.03	1.97
1.5% Si200 - 0.5% AluC - 62% D_2O - pH 6.5	14.4	112.8	4.03	2.03	2.00
Sample	**R_g3**	**P3**	**R_g2**	**P2**	**P1**
Varying Solution pH					
1.5% Si200 - 0.5% AluC - 88% D_2O - pH 2.0	11.4	89.2	4.00	2.22	1.98
1.5% Si200 - 0.5% AluC - 88% D_2O - pH 6.5	10.2	76.9	4.06	2.22	1.70
1.5% Si200 - 0.5% AluC - 88% D_2O - pH 10.0	10.6	86.4	3.99	2.25	1.82
1.5% Si200 - 0.5% AluC - 62% D_2O - pH-2.0	13.0	27.2	4.15	2.10	2.01
1.5% Si200 - 0.5% AluC - 62% D_2O - pH 6.5	14.4	112.8	4.03	2.03	2.00
1.5% Si200 - 0.5% AluC - 62% D_2O - pH 10.0	14.1	28.8	4.00	2.01	2.07
Single Particle Type Dispersions					
1.5% Si200 - 88% D_2O - pH 6.5	12.5	77.4	4.09	2.28	0.07
0.5% AluC - 62% D_2O - pH 6.5	7.2	147.8	3.98	2.11	1.07
Pure D_2O Gel Mixtures					
0.56% Si200 - 0.19% AluC - 100% D_2O - pH 6.5	5.3	54.2	3.90	2.24	1.70
1.5% Si200 - 0.5% AluC - 100% D_2O - pH 6.5	10.5	81.9	4.17	2.16	1.77

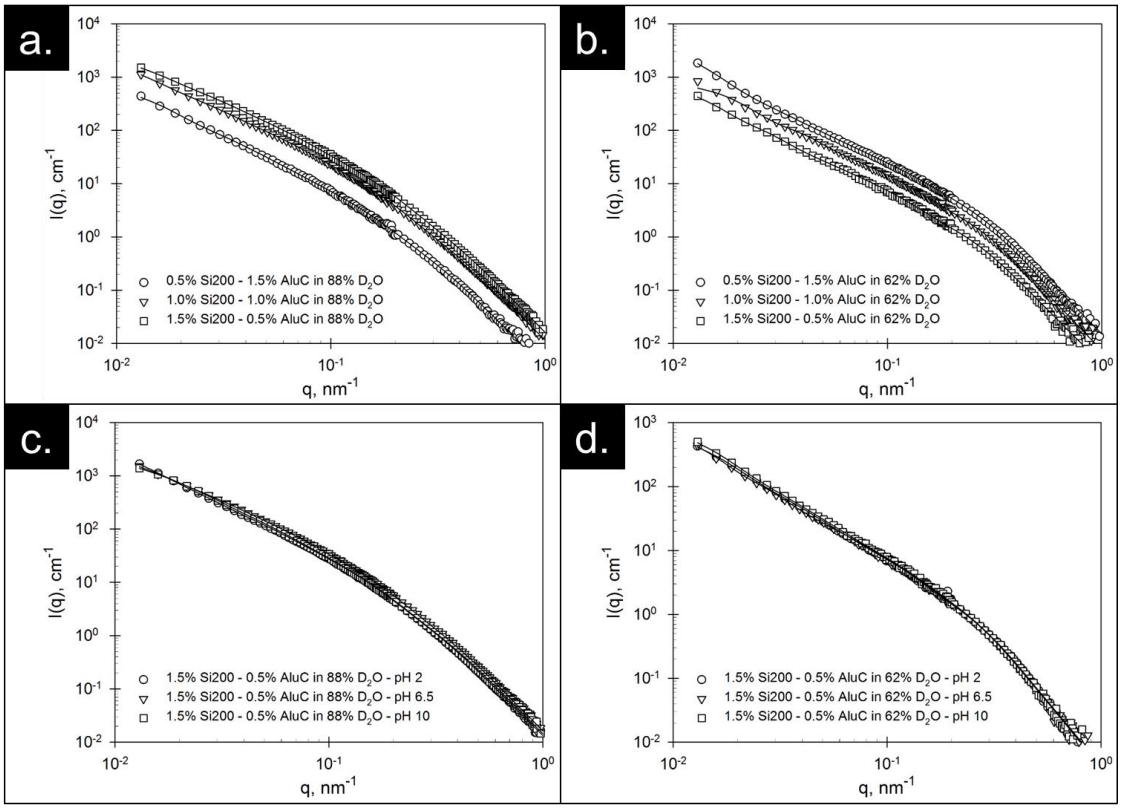


Figure 24. Scattering curves as a function of particle ratio (a. & b.) and solution pH (c. & d.) with all other parameters held constant. Figs. 4a. & c. contain data taken from gels suspended at the alumina contrast match point and Figs. 4b. & d. contain data taken from gels suspended at the silica contrast match point. Best fit lines for a Unified Power Law model are shown for each curve.

Similar results to those shown in Fig. 4 for a variety of particle concentrations can be seen in Figure 5, where scattering curves are shown as a function of particle ratio (a. & b.) and as a function of solution pH (c. & d.). These results again show that there is very little change in the scattering profile for the silica or the alumina as one changes the particle ratio or pH beyond shifts in scattering intensity related to total particle concentration. Additionally, Figs. 5a. & b. illustrate that contrast matching of the silica and alumina was successful, since the overall scattering intensity follows the concentration of the Aerosil 200 (a.) and Aeroxide AluC (b.) even though the total particle concentration remains constant in both cases. The pH variation results (5c. & 5d.) provide additional strong evidence that the gels are a result of heteroaggregation of microagglomerates since there is essentially no change in the scattering profile for either

silica (c.) or alumina (d.) as the solution pH is changed despite large changes in the rheological properties among the three samples. Specifically, the pH 6.5 sample exhibits a yield stress and viscosity 2-3 orders of magnitude larger than either the pH 2.0 or pH 10.0 samples, where all of the particles have similar surface charge and the gel network is expected to be mostly, if not completely, broken down. All SANS results consistently indicate that the microagglomerates are not being completely broken up during the mixing process, despite the use of ultrasonication. Therefore the studied gelation phenomenon appears to be the result of microagglomerate heteroaggregation similar to that illustrated in Fig. 1a.

Scattering curves contain large amounts of information but transferring that information into real-space structures can be difficult. So, for illustrative purposes, a series of modeling and visualization software suites were used to generate visual approximations of the silica and alumina nanoaggregates and percolated gel networks. NetLogo software and its 3-D diffusion limited aggregation model was used to generate fractal aggregates and agglomerates with the correct fractal dimension and VESTA was used to generate illustrations of the particle and gel models. Five model nanoaggregates

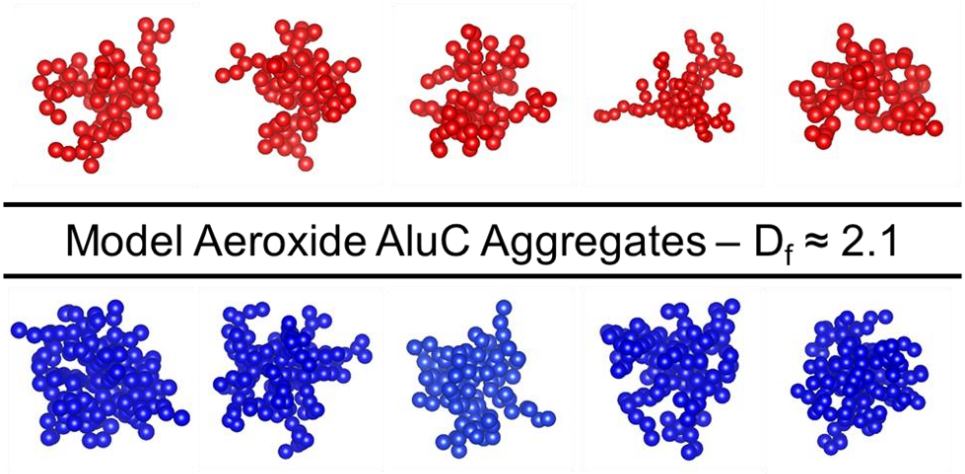


Figure 25. Model nanoaggregates of Aeroxide AluC and Aerosil 200 with the correct fractal dimension, primary particle size, and hydrodynamic radius. Alumina particles and silica particles are colored red and blue, respectively. (Particles in figure were resized to fit illustration and are not displayed at a constant relative scale.)

were created for both Aerosil 200 and Aeroxide AluC with the correct fractal dimensions, primary particle diameters, and average hydrodynamic radii. These nanoaggregates are the 'hard' nanoaggregates that cannot be broken down by sonication. Figure 6 contains illustrations of these ten model nanoaggregates with the alumina particles and silica particles colored red and blue, respectively.

The model nanoaggregates were then used to randomly populate a larger model with a fractal dimension corresponding to that of the agglomerates measured in the 100% D_2O gels shown in Fig. 2 and compared to TEM micrographs and EDS maps of thin sections of a 1.75% total particle concentration, 75:25 Si200:AluC dispersion of particles embedded in a hydrophilic polymer resin. The random population method used to generate the illustrations does not take into account electrostatic interactions that would favor the aggregation of oppositely charged particles and separation of like-charged particles, but nevertheless appears to produce a reasonable approximation of

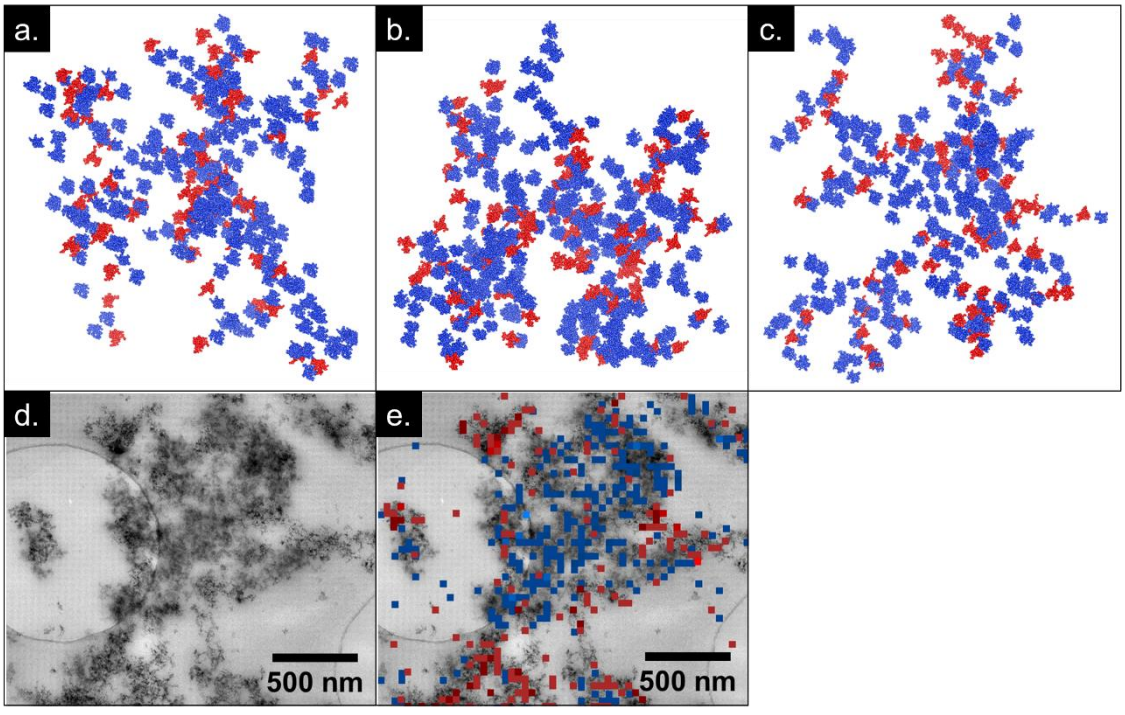


Figure 26. Illustrations of the gel networks generated using NetLogo, VESTA, and Packmol software (a.-c.) along with a high-resolution TEM micrograph (d.) and EDS elemental map (e.). Blue and red are used to indicate that the particle is Aerosil 200 and Aeroxide AluC, respectively.

the structures observed in the TEM images of the gels embedded in the polymer resin. Figure 7 shows three model gel network illustrations (a.-c.) along with a high-resolution TEM micrograph (d.) and EDS elemental map (e.). Throughout Fig. 7, blue and red are used to indicate that the particle is Aerosil 200 and Aeroxide AluC, respectively. The model gels and the EDS elemental map show qualitative similarities and the latter, at least, is likely to be reasonably accurate representations of the gel network as present in aqueous gels. Gaps between the particles observed in the gel illustrations occur when the roughly spherical nanoparticle aggregates are substituted into the cube based coordinate system used by the NetLogo 3D DLA model.

Additional detail could be added by gaining longer-range structural information for the gels from ultra-small angle scattering and/or static light scattering experiments, which can provide structural information regarding features several microns in size. This information would allow one to add an additional layer of coordination to the current models, with nanoaggregates assembled into appropriately sized microaggregates, which are then assembled into a percolated gel network of the correct fractal dimension, whereas the current models are generated under the assumption of near-complete dispersion of nanoaggregates, which we believe to not be true based on SANS results.

CONCLUSIONS

Small-angle neutron scattering experiments have been combined with electron microscopy and energy dispersive x-ray spectroscopy to quantitatively study the gel structure of electrostatically heteroaggregated fumed metal oxide nanoparticle gels under a variety of conditions. These results were then used to create qualitatively accurate models of the gel structure for illustrative purposes. The gels appear to be the result of heteroaggregation of ‘soft’ microagglomerates of silica and alumina nanoparticles that form a percolated network throughout the fluid and produce the observed yield stress and viscoelastic behavior. In pure particle solutions, these soft

microagglomerates are fully dispersed with 2-3 minutes of sonication; apparently the formation of the gel network in mixtures of the particles dissipates the sonic energy, preventing complete dispersion of the microaggregates. Perhaps gels could be generated without any microagglomerates by fully dispersing the individual particle species in more concentrated stock solutions, which could then be mixed together at the proper ratios and quantities to generate fully dispersed gels. Fully dispersed gels should result in a far greater number of interparticle electrostatic interactions, and thus a significantly stronger gel network. Since the soft microagglomerates of like-charged particles that appear to be present in the heteroaggregate gels are easily dispersed by sonication in the absence of the oppositely charged particles, these microaggregates are likely "weak links" in the gel network; the concentration of the soft microaggregates may well control the yield strength of the gels.

REFERENCES

[1] H. Barthel. Surface interactions of dimethylsiloxy group-modified fumed silica. *Coll. And Surf. A: Physiochem. And Eng. Aspects.* **1995,** *101,* 217-226.

[2] B. P. Binks and S. O. Lumsdon. Effects of oil type and aqueous phase composition on oil–water mixtures containing particles of intermediate hydrophobicity. *Phys. Chem. Chem. Phys.* **2000,** *2,* 2959-2967.

[3] P. Huttenloch, K. E. Roehl, and K. Czurda. Sorption of Nonpolar Aromatic Contaminants by Chlorosilane Surface Modified Natural Minerals. *Environ. Sci. Technol.* **2001,** *35,* 4260-4264.

[4] A. Klint. Amphiphilic surface modification of colloidal silica sols. *Master of Science Thesis in the Master Degree Programme Chemistry and Bioscience.* Chalmers University of Technology, Goteborg, Sweden. **2011.**

[5] M. Marquez, B. P. Grady, and I. Robb. Different methods for surface modification of hydrophilic particulates with polymers. *Coll. And Surf. A: Physiochem. And Eng. Aspects.* **2005,** *266,* 18-31.

[6] T. Pisuchpen, N. Chaim-ngoen, N. Intasanta, P. Supaphol, and V. P. Hoven. Tuning Hydrophobicity and Water Adhesion by Electrospinning and Silanization. *Langmuir.* **2011,** *27,* 3654-3661.

[7] D. H. Flinn, D. A. Guzonas, and R.-H. Yoon. Characterization of silica surfaces hydrophobized by octadecyltrichlorosilane. *Coll. And Surf. A: Physiochem. And Eng. Aspects.* **1994,** *87,* 163-176.

[8] B. P. Binks. Particles as surfactantssimilarities and differences. *Curr. Op. in Coll. And Interf. Sci.* **2002,** *7,* 21-41

[9] K. A. Northcott, J. Bacus, N. Taya, Y. Komatsu, J. M. Perera, and G. W. Stevens. Synthesis and characterization of hydrophobic zeolite for the treatment of hydrocarbon contaminated ground water. *J. of Haz. Mat.* **2010,** *183,* 434-440.

[10] P. A. Zapata, Y. Huang, M. A. Gonzalez-Borja, and D. E. Resasco. Silylated hydrophobic zeolites with enhanced tolerance to hot liquid water. *J. of Catalysis.* **2013,** *308,* 82-97.

[11] Y. Kuwahara, T. Kamegawa, K. Mori, Y. Matsumura, and H. Yamashita. Fabrication of Hydrophobic Zeolites Using Triethoxyfluorosilane and their Application for Photocatalytic Degradation of Acetaldehyde. *Top Catal.* **2009,** *52,* 643-648.

[12] Y. An, M. Chen, Q. Xue, and W. Liu. Preparation and self-assembly of carboxylic acid-functionalized silica. *J. of Coll. And Interf. Sci.* **2007,** *311,* 507-513.

[13] S. A. Idris, K. Alotaibi, T. A. Peshkur, P. Anderson, and L. T. Gibson. Preconcentration and selective extraction of chromium species in water samples using amino modified mesoporous silica. *J. of Coll. And Interf. Sci.* **2012,** *386,* 344-349.

[14] Y. Nam, D. Lee, and E.-B. Cho. Role of phosphate-modified mesoporous silica nanoparticles for altering biomimetic metal-induced aggregation process of pluronic F127 block copolymer. *Materials Letters.* **2013,** *110,* 176-179.

[15] Y.-K. Oh, L.-Y. Hong, Y. Asthana, and D.-P. Kim. Synthesis of Super-hydrophilic Mesoporous Silica via a Sulfonation Route. *J. Ind. Eng. Chem.* **2006,** *6,* 911-917.

[16] B. P. Binks, R. Murakami, S. P. Armes, S. Fujii, and A. Schmid. pH-Responsive Aqueous Foams Stabilized by Ionizable Latex Particles. *Langmuir,* **2007,** *23,* 8691-8694.

[17] V. Cauda, C. Argyo, A. Schlossbauer, and T. Bein. Controlling the delivery kinetics from colloidal mesoporous silicananoparticles with pH-sensitive gates. *J. of Mat. Chem.* **2010,** *20,* 4305-4311.

[18] J.-L. Liu and R.-B. Lin. Structural properties and reactivities of amino-modified silica fume solid sorbents for low-temperature CO2 capture. *Powder Technol.* **2013,** *241,* 188-195.

[19] B. Faure, G. Salazar-Alvarez, A. Ahniyaz, I Villaluenga, G. Berriozabal, Y. R. De Miguel, and L. Bergstrom. Dispersion and surface functionalization of oxide nanoparticles for transparent

photocatalytic and UV-protecting coatings and sunscreens. *Sci. and Technol. Of Adv. Mat.* **2013,** *14,* 023001.

[20] J.-T. Park, J.-A. Seo, S.-H. Ahn, J.-H. Kim, and S.-W. Kang. Surface modification of silica nanoparticles with hydrophilic polymers. *J. of Ind. And Eng. Chem.* **2010,** *16,* 517-522.

[21] P. K. Jal, S. Patel, and B. K. Mishra. Chemical modification of silica surface by immobilization of functional groups for extractive concentration of metal ions. *Talanta.* **2004,** *62,* 1005-1028.

[22] M. F. Haase, D. Grigoriev, H. Moehwald, B. Tiersch, and D. G. Shchukin. Nanoparticle Modification by Weak Polyelectrolytes for pH-Sensitive Pickering Emulsions. *Langmuir.* **2011,** *27,* 74-82.

[23] M. Motornov, R. Sheparovych, R. Lupitskyy, E. MacWilliams, and S. Minko. Responsive colloidal systems- Reversible aggregation and fabrication of superhydrophobic surfaces. *J. of Coll. And Interf. Sci.* **2007,** *310,* 481-488.

[24] D. O. Grigoriev, J. Kragel, V. Dutschk, R. Miller, and H. Mohwald. Contact angle determination of micro- and nanoparticles at fluid/fluid interfaces: the excluded area concept. *Phys. Chem. Chem. Phys.* **2007,** *9,* 6447-6454.

[25] E. Nowak, G. Combes, E. H. Stitt, and A. W. Pacek. A comparison of contact angle measurement techniques applied to highly porous catalyst supports. *Powder Technology.* **2013,** *233,* 52-64.

[26] Z. Ho´rvo¨lgyi, S. Ne´meth and J. H. Fendler. Monoparticulatelayers of silanized glass spheres at the water–air interface: particle–particle and particle–subphase interactions. *Langmuir.* **1996,** *12,* 997–1004.

[27] O. D. Velev, N. D. Denkov, V. N. Paunov, P. A. Kralchevsky and K. Nagayama. Capillary image forces: II. Experiment. *J. Colloid Interface Sci.* **1994,** *167,* 66–73.

[28] L. N. Arnaudov, O. J. Cayre, M. A. Cohen Stuart, S. D. Stoyanov, and V. N. Paunov. Measuring the three-phase contact angle of nanoparticles at fluid interfaces. *Phys. Chem. Chem. Phys.* **2010,** *12,* 328-331.

[29] B. P. Binks, J. H. Clint, A. K. F. Dyab, P. D. I. Fletcher, M. Kirkland and C. P. Whitby. Ellipsometric study of monodisperse silica particles at an oil–water interface. *Langmuir,* **2003,** *19,* 8888–8893.

[30] Y. Xiao and M. R. Wiesner. Characterization of surface hydrophobicity of engineered nanoparticles. *J. of Haz. Mat.* **2012,** *215-216,* 146-151.

[31] C. Jouany and P. Chassin, Determination of the surface energy of clay-organic complexes by contact angle measurements. *Colloids Surf.* **1987,** *27,* 289–303.

[32] I. O. Odidi, G. Buckton, and J.M. Newton. The effect of surface treatment on the values of contact angles measured on a compressed powder surface. *Intl. J. of Pharm.* **1991,** *72,* 43-49.

[33] G. Buckton, J.M. Newton. Assessment of the wettability of powders by use of compressed powder disks. *Powder Technology.* **1986,** *46*, 201–208.

[34] L. Forny, K. Saleh, R. Denoyel, and I. Pezron. Contact Angle Assessment of Hydrophobic Silica Nanoparticles Related to the Mechanisms of Dry Water Formation. *Langmuir.* **2010,** *26,* 2333-2338.

[35] N. Yan, Y. Maham, J. H. Masliyah, M. R. Gray, and A. E. Mather. Measurement of Contact Angles for Fumed Silica Nanospheres Using Enthalpy of Immersion Data. *J. of Coll. And Interf. Sci.* **2000,** *228,* 1-6.

[36] P. D. I. Fletcher and B. L. Holt. Controlled Silanization of Silica Nanoparticles to Stabilize Foams, Climbing Films, and Liquid Marbles. *Langmuir.* **2011,** *27,* 12869-12876.

[37] P. Van Der Voort and E. F. Vansant. Silylation of the Silica Surface: A Review. *J. Liq. Chrom. & Rel. Technol.* **1996,** *19,* 2723-2752.

[38] M. L. Hair and C. P. Tripp. Alkylchlorosilane reactions at the silica surface. *Coll. And Surf. A: Physiochem. And Eng. Aspects.* **1995,** *105,* 95-103.

[39] B. P. Binks and C. P. Whitby. Nanoparticle silica-stabilised oil-in-water emulsions, improving emulsion stability. *Coll. And Surf. A: Physiochem. And Eng. Aspects.* **2005,** *253,* 105-115.

[40] E. Tombacz, M. Szekeres, I. Kertesz, and L. Turi. pH-dependent aggregation state of highly dispersed alumina, titania, and silica particles in aqueous medium. *Progr. Colloid Polym. Sci.* **1995,** *98,* 160-168.

[41] B. Neirinck, J. van Deursen, O. van der Biest and J. Vleugels. Wettability assessment of Submicrometer alumina powder using a modified Washburn method. *J. of Amer. Ceram. Soc.* **2010,** *93,* 2515.

[42] J. W. Dove, G. Buckton, and C. Doherty. A comparison of two contact angle measurement methods and inverse gas chromatography to assess the surface energies of theophylline and caffeine. *Intl. J. of Pharmaceutics.* **1996,** *138,* 199-206.

[43] J. Shang, M. Flury, J. B. Harsh, and R. I. Zollars. Comparison of different methods to measure contact angles of soil colloids. *J. of Coll. And Interf. Sci.* **2008,** *328,* 299-307.

[44] B. P. Binks and S. O. Lumsdon. Influence of Particle Wettability on the Type and Stability of Surfactant-Free Emulsions. *Langmuir.* **2000,** *16,* 8622-8631.

[45] G. D. Nadkarni and S. Garoff. An Investigation of Microscopic Aspects of Contact Angle Hysteresis: Pinning of the Contact Line on a Single Defect. *Europhysics Letters.* **1992,** *20,* 523-528.

[46] Brown, G.; Henrich, V.; Casey, W.; Clark, D.; Eggleston, C.; Felmy, .; Goodman, D.; Gratzel, M.; Maciel, G.; McCarthy, M.; Nealson, K.; Sverjensky, D.; Toney, M.; Zachara, Metal Oxide Surfaces and Their Interactions with Aqueous Solutions and Microbial Organisms. *J. Chem. Rev.* **1999**, *99***,** 77-174.

[47] Gun'ko, V.; Zarko, V.; Leboda, R.; Chibowski, E. Aqueous suspension of fumed oxides: particle size distribution and zeta potential. *Adv. In Coll. and Interf. Sci.* **2001**, *91,* 1-112.

[48] Evonik Industries. "Basic characteristics of Aerosil fumed silica", *Technical Bulletin: Fine Particles #11.*

[49] Avendano, C.; Lee, S.; Escalera, G.; Colvin, V. Magnetic Characterisation of Nanoparticles Designed for Use as Contrast Agents for Downhole Measurements. *SPE Nanotechnology Conf. Notes.* **2012**, 1115-1125.

[50] Raghavan, S.; Walls, H.; Khan, S. Rheology of Silica Dispersions in Organic Liquids: New Evidence for Solvation Forces Dictated by Hydrogen Bonding. *Langmuir.* **2000**, *16*, 7920-7930.

[51] Tschapek, M.; Tcheichvili, L.; and Wasowski, C. The Point of Zero Charge Of Kaolinite and SiO_2+Al_2O_3 Mixtures. *Clay Minerals.* **1974**, *10***,** 219-229.

[52]Cao, X.; Cummins, H.; Morris, J. Structural and rheological evolution of silica nanoparticle gels. *Soft Matter.* **2010**, *6,* 5425-5433.

[53] Fisher, M.; Colic, M.; Rao, M.; Lange, F. Effect of Silica Nanoparticle Size on the Stability of Alumina/Silica Suspensions. *J. Am. Ceram. Soc.* **2001**, *84*, 713-718.

[54] Binks, B.; Liu, W.; Rodrigues, J. Novel Stabilization of Emulsions via the Heteroaggregation of Nanoparticles. *Langmuir.* **2008**, *24*, 4443-4446.

[55] Kim, A.; Hauch, K.; Berg, J.; Martin, J.; Anderson, R. Linear chains and chain-like fractals from electrostatic heteroaggregation. *J. of Coll. And Interf. Sci.* **2003,** *260,* 149-159.

[56] Rasa, M.; Philipse, A.; Meeldijk, J. Heteroaggregation, repeptization and stability in mixtures of oppositely charged colloids. *J. of Coll. And Interf. Sci.* **2004,** *278,* 115-125.

[57] Lopez-Lopez, J.; Schmitt, A.; Moncho-Jorda, A.; Hidalgo-Alvarez, R. Electrostatic heteroaggregation regimes in colloidal suspensions. *Adv. In Coll. And Interf. Sci.* **2009,** *147-148,* 186-204.

[58] Hench, L.; West, J. The Sol-Gel Process. *Chemistry Review.* **1990**, *90*, 33-72.

[59] Garcia-Perez, P.; Pagnoux, C.; Pringuet, A.; Videcoq, A.; Baumard, J. Agglomeration of alumina submicronparticles by silica nanoparticles: Application to processing spheres by colloidal route. *J. Colloid and Interface Sci.* **2007**, *313*, 527-536.

[60] Tombacz, E.; Szekeres, M.; Kertesz, I.; Turi, L. pH dependent aggregation state of highly dispersed alumina, titania, and silica particles in aqueous medium. *Progr. Colloid Polym. Sci.* **1995**, *98*, 160-168.

[61] Nallamilli, T.; Mani, E.; Basavaraj, M. A Model for the Prediction of Droplet Size in Pickering Emulsions Stabilized by Oppositely Charged Particles. *Langmuir.* **2014,** *30,* 9336-9345.

[62] Ghezzi, F.; Earnshaw, J.; Finnis, M.; McCluney, M. Pattern Formation in Colloidal Monolayers at the Air–Water Interface. *J. of Coll. And Interf. Sci.* **2001,** *238,* 433-446.

[63] Robinson, D.; Earnshaw, J. Initiation of Aggregation in Colloidal Particle Monolayers. *Langmuir.* **1993,** *9,* 1436-1438.

[64] Negi, A.; Osuji, C. New insights on fumed colloidal rheology—shear thickening and vorticity-aligned structures in flocculating dispersions. *Rheol Acta.* **2009,** *48,* 871-881.

[65] Kim, J.; Fang, J.; Eberle, A.; Castenada-Priego, R.; Wagner, N. Gel Transition in Adhesive Hard-Sphere Colloidal Dispersions: The Role of Gravitational Effects. *Physical Review Letters.* **2013,** *110,* 208302.

[66] Kalman, D. Microstructure and Rheology of Concentrated Suspensions of Near Hard-Sphere Colloids. *University of Delaware.* **2010,** 12-15.

[67] Beaucage, G. Small-Angle Scattering from Polymeric Mass Fractals of Arbitrary Mass-Fractal Dimension. *J. Appl. Cryst.* **1996**, *29*, 134-146.

[68] Schaefer, D.; Rieker, T.; Agamalian, M.; Lin, J.; Fischer, D.; Sukumaran, S.; Chen, C.; Beaucage, G.; Herd, C.; Ivie, J. Multilevel structure of reinforcing silica and carbon. *J. Appl. Cryst.* **2000**, *33*, 587-591.

[69] Schmidt, P. Small-Angle Scattering Studies of Disordered, Porous and Fraetal Systems. *J. Appl. Cryst.* **1991**, *24*, 414-435.

[70] Martin, J.; Hurd, A. Scattering from Fractals. *J. Appl. Cryst.* **1987**, *20*, 61-78.

[71] Dukhin, A.S., Goetz, P.J., *Characterization of Liquids, Nano- and Microparticulates, and Porous Bodies using Ultrasound*, 2ed., Elsevier, New York, **2010**.

[72] Kosmulski M. "Chemical Properties of Material Surfaces", Marcel Dekker. (2001).

[73] Milnor J. *Self-Similarity and Hairiness in the Mandelbrot Set*. "Computers in Geometry and Topology", Marcel Dekker. **1989**.

[74] Tolman, S.; Meakin P. Two, Three and Four-Dimensional Diffusion-limited Aggregation Models. *Physical A.* **1989**, *158*, 801-816.

[75] Cunningham, N. "What is Yield Stress and How is it Measured" Brookfield Engineering **2006.**

[76] Scales, P.; Johnson, S.; Healy, T. Shear Yield Stress Colloidal of Partially Flocculated Suspensions *AIChE J.* **1998**, *44*, 538.

[77] Gun'ko, V.; Zarko, V.; Turov, V.; Leboda, R.; Chibowski, E. Distribution Effect of the Second Phase in Disperse Silica/ X Oxides (X) Al2O3, TiO2, GeO2) on Their Surface Properties. *Langmuir* **1999**, *15.* 5694-5702.

[78] Barthel, H.; Rosch, L.; and Weis, J. "Organosilicon Chemistry II", VCH. **1996**, 761-778.

[79] Parsegian, V.; Zemb, T. Hydration forces: Observations, explanations, expectations, questions. *Curr. Op. in Coll. & Interf. Sci.* **2011**, *16.* 618–624.

[80] M. T. Balhoff and K. E. Thompson. Modeling the steady flow of yield-stress fluids in packed beds. *AIChE Journal.* **2004,** *50,* 3034-3048.

[81] G. Bossis and E. Lemaire. Yield stresses in magnetic suspensions. *J. of Rheol.* **1991,** *35,* 1345-1354.

[82] L. Marshall, C. F. Zukoski, and J. W. Goodwin. Effects of Electric Fields on the Rheology of Non-aqueous Concentrated Suspensions. *J. Chem. Soc., Faraday Trans.* **1989,** *85,* 2785-2795.

[83] G. G. Chase and P. Dachavijit. Incompressible Cake Filtration of a Yield Stress Fluid. *Sep. Sci. and Tech.* **2003,** *38,* 745-766

[84] B. Y. Ahn, E. B. Duoss, M. J. Motala, X. Guo, S.-I. Park, Y. Xiong, J. Yoon, R. G. Nuzzo, J. A. Rogers, and J. A. Lewis. Omnidirectional Printing of Flexible, Stretchable, and Spanning Silver Microelectrodes. *Science.* **2009,** *323,* 1590-1593.

[85] Y. S. Lee, E. D. Wetzel, and N. J. Wagner. The ballistic impact characteristics of Kevlar woven fabrics impregnated with a colloidal shear thickening fluid. *J. of Mat. Sci.* **2003,** *38,* 2825-2833.

[86] J. L. Drury and D. J. Mooney. Hydrogels for tissue engineering: scaffold design variables and applications. *Biomaterials.* **2003,** *24,* 4337-4351.

[87] B. Derakhshandeh, S. G. Hatzikiriakos, and C. P. J. Bennington. The apparent yield stress of pulp fiber suspensions. *J. Rheol.* **2010,** *54,* 1137-1154.

[88] F. Pignon, A. Magnin, J.-M. Piau, B. Cabane, P. Lindner, and O. Diat. Yield stress thixotropic clay suspension: Investigations of structure by light, neutron, and x-ray sattering. *Phys. Rev. E.* **1997,** *56,* 3281-3289.

[89] A. Negi and C. Osuji. New insights on fumed colloidal rheology—shear thickening and vorticity-aligned structures in flocculating dispersions. *Rheol Acta.* **2009,** *48,* 871-881.

[90] V. Gun'ko, V. Zarko, R. Leboda, E. Chibowski. Aqueous suspension of fumed oxides: particle size distribution and zeta potential. *Adv. In Coll. and Interf. Sci.* **2001**, *91,* 1-112.

[91] Evonik Industries. "Basic characteristics of Aerosil fumed silica", *Technical Bulletin: Fine Particles #11.*

[92] J. Jiang, G. Oberdorster, and P. Biswas. Characterization of size, surface charge, and agglomeration state of nanoparticle dispersions for toxicological studies. *J. Nanopart. Res.* **2009,** *11,* 77-89.

[93] R. Wengeler, F. Wolf, N. Dingenouts, and H. Nirschl. Characterizing Dispersion and Fragmentation of Fractal, Pyrogenic Silica Nanoagglomerates by Small-Angle X-ray Scattering. *Langmuir.* **2007,** *23,* 4148-4154.

[94] C. Avendano, S. Lee, G. Escalera, V. Colvin. Magnetic Characterisation of Nanoparticles Designed for Use as Contrast Agents for Downhole Measurements. *SPE Nanotechnology Conf. Notes.* **2012**, 1115-1125.

[95] E. van der Aerschot and J. Mewis. Equilibrium properties of reversibly flocculated dispersions. *Colloids and Surfaces.* **1992,** *69,* 15-22.

[96] N. B. Uriev and I. Y. Ladyzhinsky. Fractal models in rheology of colloidal gels. *Coll. And Surf. A: Phys. And Engin. Aspects.* **1996,** *108,* 1-11.

[97] S. Raghavan, H. Walls, S. Khan. Rheology of Silica Dispersions in Organic Liquids: New Evidence for Solvation Forces Dictated by Hydrogen Bonding. *Langmuir.* **2000**, *16*, 7920-7930.

[98] M. Tschapek, L. Tcheichvili, and C. Wasowski. The Point of Zero Charge Of Kaolinite and SiO_2+Al_2O_3 Mixtures. *Clay Minerals.* **1974**, *10***,** 219-229.

[99] G. Brown, V. Henrich, W. Casey, D. Clark, C. Eggleston, A. Felmy, D. Goodman, M. Gratzel, G. Maciel, M. McCarthy, K. Nealson, D. Sverjensky, M. Toney, J. Zachara. Metal Oxide Surfaces and Their Interactions with Aqueous Solutions and Microbial Organisms. *J. Chem. Rev.* **1999**, *99,* 77-174.

[100] V. I. Zarko, V. M. Gun'ko, E. Chibowski, V. V. Dudnik, and R. Leboda. Study of surface properties of fumed alumina/silica materials. *Coll. And Surf. A: Phys. And Engin. Aspects.* **1997,** *127,* 11-18.

[101] M. L. Hair. Hydroxyl Groups on Silica Surface. *J. of Non-Cryst. Solids.* **1975,** *19,* 299-309.

[102] M. Fisher, M. Colic, M. Rao, and F. Lange. Effect of Silica Nanoparticle Size on the Stability of

Alumina/Silica Suspensions. *J. Am. Ceram. Soc.* **2001**, *84*, 713-718.

[103] A. Kim, K. Hauch, J. Berg, J. Martin, and R. Anderson. Linear chains and chain-like fractals from electrostatic heteroaggregation. *J. of Coll. And Interf. Sci.* **2003,** *260,* 149-159.

[104] Y. Zong, G. Yuan, C. Zhao, and C. C. Han. Differentiating bonding and caging in a charged colloid system through rheological measurements. *J. of Chem. Phys.* **2013,** *138,* 184902.

[105] M. Rasa, A. Philipse, and J. Meeldijk. Heteroaggregation, repeptization and stability in mixtures of oppositely charged colloids. *J. of Coll. And Interf. Sci.* **2004,** *278,* 115-125.

[106] Binks, B.; Liu, W.; Rodrigues, J. Novel Stabilization of Emulsions via the Heteroaggregation of Nanoparticles. *Langmuir.* **2008**, *24*, 4443-4446.

[107] J. Lopez-Lopez, A. Schmitt, A. Moncho-Jorda, and R. Hidalgo-Alvarez. Electrostatic heteroaggregation regimes in colloidal suspensions. *Adv. In Coll. And Interf. Sci.* **2009,** *147-148,* 186-204.

[108] J. S. Weston, D. Venkataramani, C. P. Aichele, B. P. Grady, J. H. Harwell, and D. Resasco. Pseudosolid, Shear-Thinning gel formation in binary dispersions of metal oxide nanoparticles at low volume fractions. *Langmuir.* **2014,** *30,* 14982-14990.

[109] E. Tombacz, M. Szekeres, I. Kertesz, and L. Turi. pH dependent aggregation state of highly dispersed alumina, titania, and silica particles in aqueous medium. *Progr. Colloid Polym. Sci.* **1995**, *98***,** 160-168.

[110] J. Kim, J. Fang, A. Eberle, R. Castenada-Priego, and N. Wagner. Gel Transition in Adhesive Hard-Sphere Colloidal Dispersions: The Role of Gravitational Effects. *Physical Review Letters.* **2013,** *110,* 208302.

[111] D. Kalman. Microstructure and Rheology of Concentrated Suspensions of Near Hard-Sphere Colloids. *University of Delaware.* **2010,** 12-15.

[112] M. Castro, D. W. Giles, C. W. Macosko, and T. Moaddel. Comparison of methods to measure yield stress of soft solids. *J. Rheol.* **2010,** *54,* 81-94.

[113] L. Zhu, N. Sun, K. Papadopoulos, and D. D. Kee. A slotted plate device for measuring static yield stress. *J. Rheol.* **2001,** *45,* 1105-1122.

[114] M. D. Green, M. Eberl, and K. A. Landman. Compressive Yield Stress of Flocculated Suspensions: Determination via Experiment. *AIChE Journal.* **1996,** *42,* 2308-2318.

[115] H. A. Barnes and K. Walters. The yield stress myth? *Rheol. Acta.* **1985,** *24,* 323-326.

[116] D. Bonn and M. M. Denn. Yield Stress Fluids Slowly Yield to Analysis. *Science.* **2009,** *324,* 1401-1402.

[117] T. Hemphill and A. Pilehvari. Yield-power law model more accurately predicts mud rheology. *Oil & Gas Journal.* **1993,** *91,* 45-54.

[118] F. de Larrard, C. F. Ferraris, and T. Sedran. Fresh Concrete: A Herschel-Bulkley Model. *Materials and Structures.* **1998,** *31,* 494-498.

[119] X. Huang and M. H. Garcia. A Herschel-Bulkley model for mud flow down a slope. *J. Fluid Mech.* **1998,** *374,* 305-333.

[120] L. E. Silbert and J. R. Melrose. The rheology and microstructure of concentrated, aggregated colloids. *J. Rheol.* **1999,** *43,* 673-700.

[121] T. S. K. Ng and G. H. McKinley. Power law gels at finite strains: The non-linear rheology of gluten gels. *J. Rheol.* **2008,** *52,* 417-449.

[122] E. Paineau, L. J. Michot, I Bihannic, and C. Baravian. Aqueous Suspensions of Natural Swelling Clay Minerals. 2. Rheological Characterization. *Langmuir.* **2011,** *27,* 7806-7819.

[123] J. C. Baird and J. Y. Walz. The effects of added nanoparticles on aqueous kaolinite suspensions II: Rheological effects. *J. Coll. And Interf. Sci.* **2007,** *306,* 411-420.

[124] V. Grenard, T. Divoux, N. Taberlet, and S. Manneville. Timescales in creep and yielding of attractive gels. *Soft Matter.* **2014,** *10,* 1555-1571.

[125] D. Missirlis, J. a. Hubbell, and N. Tirelli. Thermally-induced glass formation from hydrogel nanoparticles. *Soft Matter.* **2006,** *2,* 1067-1075.

[126] A. P. Deshpande, J. M. Krishan, and P. B. S. Kumar. Rheology of Complex Fluids. Springer, New York, **2010,** 11-16.

[127] L. E. Silbert, J. R. Melrose, and R. C. Ball. The rheology and microstructure of concentrated, aggregated colloids. *J. Rheol.* **1999,** *43,* 673-700.

[128] M. Fraiha, J. D. Biagi, and A. C. Ferraz. Rheological behavior of corn and soy mix as feed ingredients. *Cienc. Tecnol. Aliment.* **2011,** *31,* 129-134.

[129] M. Padmanabhan, and M. Bhattacharya. Flow behavior and exit pressures of corn meal under high-shear-high temperature extrusion conditions using a slit die. *J. Rheol.* **1991,** *35,* 314-342.

[130] M. Benna, N. Kbir-Ariguib, A. Magnin, and F. Bergaya. Effect of pH on Rheological Properties of Purified Sodium Bentonite Suspensions. *J. Coll. And Interf. Sci.* **1999,** *218,* 442-455.

[131] P. J. Scales, S. B. Johnson, T. W. Healy, and P. C. Kapur. Shear Yield Stress of Partially Flocculated Colloidal Suspensions. *AIChE Journal.* **1998,** *44,* 538-544.

[132] L. Hench and J. West. The Sol-Gel Process. *Chemistry Review.* **1990**, *90*, 33-72.

[133] P. Garcia-Perez, C. Pagnoux, A. Pringuet, A. Videcoq, and J. Baumard. Agglomeration of alumina submicronparticles by silica nanoparticles: Application to processing spheres by colloidal route. *J. Colloid and Interface Sci.* **2007**, *313*, 527-536.

[134] T. Ujihara and K. Osamura. Kinetic Analysis of Spinodal decomposition process in Fe-Cr alloys by small angle neutron scattering. *Acta Materialia.* **2000,** *48,* 1629-1637.

[135] P. A. Fitzgerald, T. W. Davey, and G. G. Warr. Micellar Structure in Gemini Nonionic Surfactants from Small-Angle Neutron Scattering. *Langmuir.* **2005,** *21,* 7121-7128.

[136] E. Paineau, I. Bihannic, C. Baravian, A.-M. Philippe, P. Davidson, P. Levitz, S. S. Funari, C. Rochas, and L. J. Michot. Aqueous suspensions of natural swelling clay minerals. 1. Structure and electrostatic interactions. *Langmuir.* **2011,** *27,* 5562-5573.

[137] M. Granite, A. Radulescu, and Y. Cohen. Small-angle neutron scattering from aqueous dispersions of single-walled carbon nanotubes with Pluronic F127 and poly(vinylpyrrolidone). *Langmuir.* **2012,** *28,* 11025-11031.

[138] P. Bernado, E. Mylonas, M. V. Petoukhov, M. Blackledge, and D. I. Svergun. Structural characterization of flexible proteins using small-angle x-ray scattering. *J. Am. Chem. Soc.* **2007,** *129,* 5656-5664.

[139] D. W. Hayward, J. B. Gilroy, P. A. Rupar, L. Chabanne, C. Pizzey, M. A. Winnik, G. R. Whittell, I. Manners, and R. M. Richardson. Liquid Crystalline Phase Behavior of Well-Defined Cylindrical Block Copolymer Micelles Using Synchrotron Small-Angle X-ray Scattering. *Macromolecules.* **2015,** *48,* 1579-1591.

[140] R. Akkal, N. Cohaut, M. Khodja, T. Agmed-Zaid, F. Bergaya. Rheo-SAXS investigation of organoclay water-in-oil emulsions. *Colloids and Surfaces A: Physicochem. Eng. Aspects.* **2013,** *436,* 751-762.

[141] W. G. Lilyestrom, S. Yadav, S. J. Shire, and T. M. Scherer. Monoclonal antibody self-association, cluster formation, and rheology at high concentrations. *J. Phys. Chem. B.* **2013,** *117,* 6373-6384.

[142] E. Tombacz, M. Szekeres, I. Kertesz, and L. Turi. pH dependent aggregation state of highly dispersed alumina, titania, and silica particles in aqueous medium. *Progr. Colloid Polym. Sci.* **1995**, *98***,** 160-168.

[143] J. Kim, J. Fang, A. Eberle, R. Castenada-Priego, and N. Wagner. Gel Transition in Adhesive Hard-Sphere Colloidal Dispersions: The Role of Gravitational Effects. *Physical Review Letters.* **2013,** *110,* 208302.

[144] D. Kalman. Microstructure and Rheology of Concentrated Suspensions of Near Hard-Sphere Colloids. *University of Delaware.* **2010,** 12-15.

[145] C. J. Glinka, J. G. Barker, B. Hammouda, S. Krueger, J. J. Moyer, and W. J. Orts. The 30 m Small-Angle Neutron Scattering Instruments at the National Institute of Standards and Technology. *J. Appl. Cryst.* **1998,** *31,* 430-445.

[146] J. K. Zhao, C. Y. Gao, and D. Liu. The extended Q-range small-angle neutron scattering diffractometer at the SNS. *J. Appl. Cryst.* **2010,** *43,* 1068-1077.

[147] J. K. Zhao. Neutron optics optimization for the SNS EQ-SANS diffractometer. *Nuc. Instr. And Met. In Phys. Res. A.* **2012,** *668,* 59-63.

[148] S. R. Kline. Reduction and Analysis of SANS and USANS Data using Igor Pro. *J. Appl. Cryst.* **2006,** *39,* 895.

[149] J. K. Zhao. Data processing for the SNS EQ-SANS diffreactometer. *Nuc. Instr. And Met. In Phys. Res. A.* **2011,** *647,* 107-111.

[150] G. Alina, P. Butler, J. Cho, M. Doucet, and P. Kienzle. *SANS analysis software.* Developed using DANSE software under NSF award DMR-0520547.

[151] G. Beaucage. Small-Angle Scattering from Polymeric Mass Fractals of Arbitrary Mass-Fractal Dimension. *J. Appl. Cryst.* **1996,** *29,* 134-146.

[152] G. Beaucage, T. A. Ulibarri, E. P. Black, and D. W. Schaefer. Multiple Size Scale Structures in Silica—Siloxane Composites Studied by Small-Angle Scattering. *Hybrid Organic-Inorganic Composites.* **1995,** *Ch. 9,* 97-111.

[153] S. Tisue and U. Wilensky. NetLogo: Design and implementation of a multi-agent modeling environment. *Proc. Of Agent Conf. on Social Dynamics: Interaction, Reflexivity and Emergence.* **2004,** Chicago, IL

[154] M. Wozniak, F. R. A. Onofri, S. Barbosa, J. Yon, and J. Mroczka. Comparison of methods to derive morphological parameters of mult-fractal samples of particle aggregates from TEM images. *J. of Aerosol Sci.* **2012,** *47,* 12-26.

[155] K. Momma and F. Izumi. VESTA 3 for three-dimensional visualization of crystal, volumetric and morphology data. *J. Appl. Crystallogr.* **2011,** *44,* 1272-1276.

[156] R. Wengeler, F. Wolf, N. Dingenouts, and H. Nirschl. Characterizing Dispersion and Fragmentation of Fractal, Pyrogenic Silica Nanoagglomerates by Small-Angle X-ray Scattering. *Langmuir.* **2007,** *23,* 4148-4154.

[157] H. K. Kammler, G. Beaucage, R. Mueller, and S. E. Pratsinis. Structure of Flame-Made Silica Nanoparticles by Ultra-Small-Angle X-ray Scattering. *Langmuir.* **2004,** *20,* 1915-1921.

[158] V. S. Nguyen, D. Rouxel, R. Hadji, B. Vincent, and Y. Fort. Effect of ultrasonication and dispersion stability on the cluster size of alumina nanoscale particles in aqueous solutions. *Ultrasonics Sonochemistry.* **2011,** *18,* 382-388.

[159] L. Martínez, R. Andrade, E. G. Birgin, J. M. Martínez. Packmol: A package for building initial configurations for molecular dynamics simulations. *J. of Comput. Chem.* **2009,** *30,* 2157-2164.

[160] J. Baldyga, L. Makowski, W. Orciuch, C. Sauter, and H. P. Schuchmann. Deagglomeration processes in high-shear devices. *Chem. Eng. Res. And Des.* **2008,** *86,* 1369-1381.

[161] N. G. Ozcan-Taskin, G. Padron, and A. Voelkel. Effect of particle type on the mechanisms of break-up of nanoscale particle clusters. *Chem. Eng. Res. And Des.* **2009,** *87,* 468-473.

[162] C. Schilde, C. Mages-Sauter, A. Kwade, H. P. Schuchmann. Efficiency of different dispersing devices for dispersing nanosized silica and alumina. *Powder Tech.* **2011,** *207,* 353-361.

[163] V. Gun'ko, V. Zarko, R. Leboda, E. Chibowski. Aqueous suspension of fumed oxides: particle size distribution and zeta potential. *Adv. In Coll. and Interf. Sci.* **2001**, *91,* 1-112.

[164] D. W. Schaefer, T. Rieker, M. Agamalian, J. S. Lin, D. Fischer, S. Sukumaran, C. Chen, G. Beaucage, C. Herd, and J. Ivie. Multilevel structure of reinforcing silica and carbon. *J. Appl. Cryst.* **2000,** *33,* 587-591.

[165] F. Pignon, A. Magnin, J.-M. Piau, B. Cabane, P. Lindner, and O. Diat. Yield Stress thixotropic clay suspension: Investigations of structure by light, neutron, and x-ray scattering. *Phys. Rev. E.* **1997,** *56,* 3281-3289.

APPENDIX I: GEL CENTRIFUGATION STUDIES

The stability of colloidal dispersions is an important parameter during industrial implementation since it has a strong effect on important parameters like shelf life, shipping time, preparation location, etc. The sedimentation behavior of the studied nanoparticle gel mixtures were tested using a series of centrifugation experiments at a variety of centrifuge speeds. Silica/alumina gel samples were prepared in test tubes at a variety of total particle concentrations and particle ratios. The samples were then placed into an IEC Clinical Centrifuge and subjected to a particular rotational speed for ten minutes. The samples were then removed from the centrifuge and the height of the opaque gel phase and clear supernatant phase were recorded, as shown in Figure 27. These height values were then used to calculate the total particle concentration remaining in the gel phase under the assumption that no particles remained in the clear supernatant. The sample was then redispersed using vortex mixing and sonication prior to testing at the next centrifuge speed. Figure 28 shows the final particle concentration in the gel phase as a function of effective gravitational acceleration for a variety of Aerosil

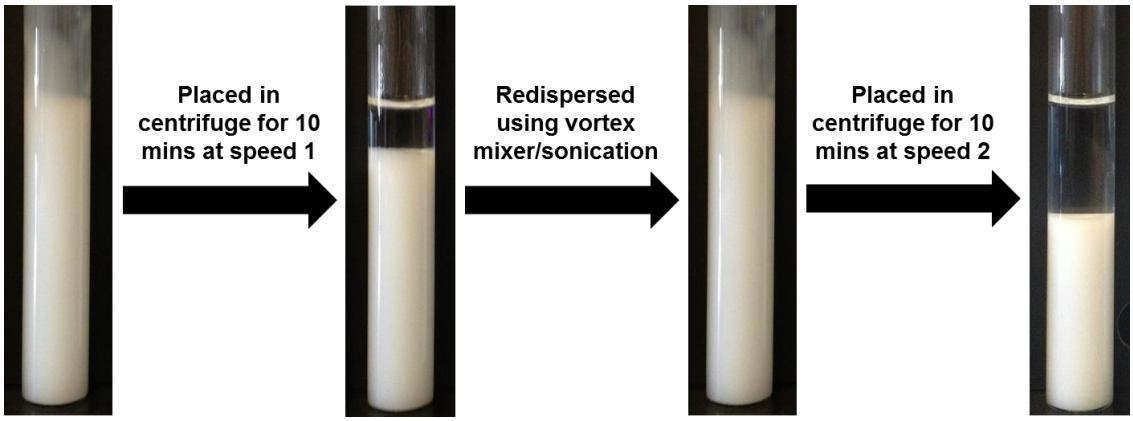


Figure 27. Method used to study gel stability against sedimentation

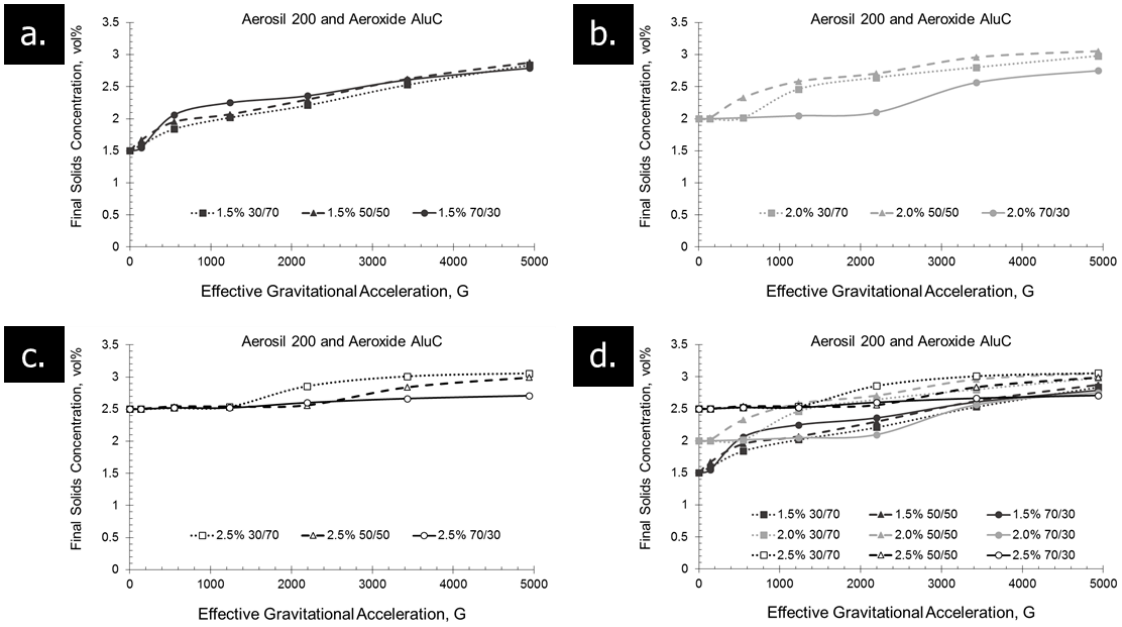


Figure 28. Centrifuge stability results for Aerosil 200:Aeroxide AluC gels at 1.5 vol% (a.), 2.0 vol% (b.), and 2.5 vol% (c.) total particle concentrations at three different silica/alumina ratios. A combined plot containing all of the data is also shown (d.). All %'s reflect vol%.

200: Aeroxide AluC gel mixtures. The gels exhibited a very strong resistance to sedimentation considering the relatively low initial concentrations of the suspended nanoparticles and similar behavior to that shown in the yield stress results can be seen in terms of particle ratio, with the 70/30 silica/alumina samples having the greatest resistance to sedimentation or network collapse when compared to the 50/50 and 30/70 samples, though this trend is less obvious at low particle concentrations. The combined plot of all of the data (d.) appears to show an interesting convergence of the final particle concentration in the gel phase at very high effective accelerations. This seems to imply that there may be some 'critical' concentration where the gel network becomes significantly harder to collapse via compressive acceleration forces. This 'critical' concentration appears to occur somewhere between 3.0% and 4.0% solids, which is still a relatively low solids fraction compared to other nanoparticle slurries that can experience sedimentation problems, such as inks. Additionally, the gels have experienced no noticeable sedimentation issues under standard gravitational

acceleration over the time span of these investigations (~2 years), though if the dispersions are moved outside of the gelation pH region, sedimentation does appear to become an issue. Additional centrifuge stability results are shown in Figure 29 for gel mixtures consisting of Aerosil 150:Aeroxide AluC (a.) and Aerosil 200:Aeroxide Alu130 (b.). These gels exhibit similar behavior, alluding the possibility of a 'critical' particle concentration, effect of particle ratio on initial network collapse, and relative stability against catastrophic sedimentation/collapse.

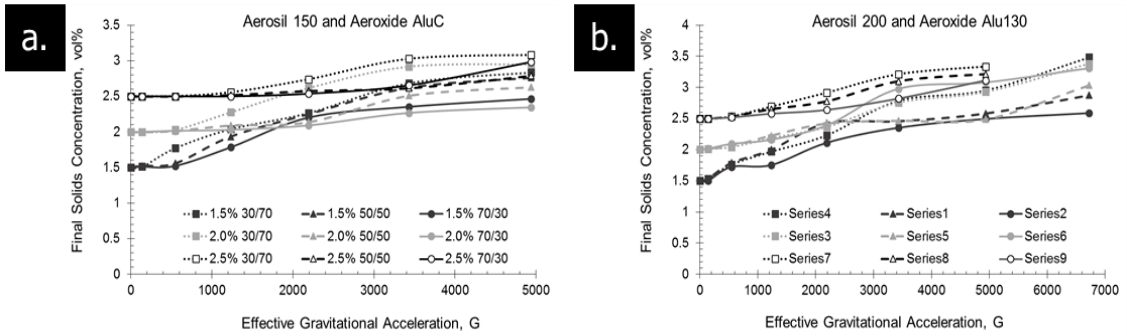


Figure 29. Centrifuge stability results for gels consisting of Aerosil 150:Aeroxide AluC (a.) and Aerosil 200:Aeroxide Alu130 (b.) mixtures.

APPENDIX II: TOTAL SYSTEM CHARGE AND GELATION

As alluded to in previous chapters, the strongest gelation phenomenon appears at particle ratios where the number of positive surface charges is roughly balanced by the number of negative surface charges in the gel mixture. Tombacz measured values of specific surface charge (Coulombs/nm^2) which were used to calculate the total surface charge (TSC) using equation 6. The total surface charge is a measure of how many +/-

$$TSC = (m_1 * SA_1 * SC_1 + m_2 * SA_2 * SC_2)/NPC \qquad \text{(Eqn. 6)}$$

TSC – Total Surface Charge (C/vol% np's)

m_i – mass of np *i* (grams)

SA_i – Surface Area of np *i* (m^2/g)

SC_i – Surface Charge of np *i* at pH (C/m^2)

NPC – nanoparticle concentration (vol %)

surface charge pairings are present, with a TSC of 0 indicating that there are equal numbers of positively and negatively charged surface groups present in the dispersion. Figure 30 illustrates how the total surface charge changes as a function of pH for a variety of Aerosil 200:Aeroxide AluC ratios. The curves show that the exact pH where the mixture contains an eqal number of positive and negative surface charge sites varies slightly with solution pH, with increasing silica fractions requiring lower pH values to be at a balance. If one zooms in on the region of the graph near to the cross-over point for all of the curves and compare it to the Aerosil 200:Aeroxide AluC phase behavior diagram from Chapter 2, as shown in Figure 31, it can be seen that the total surface charge and the gelation region correspond well to one another. Specifically, the gelation

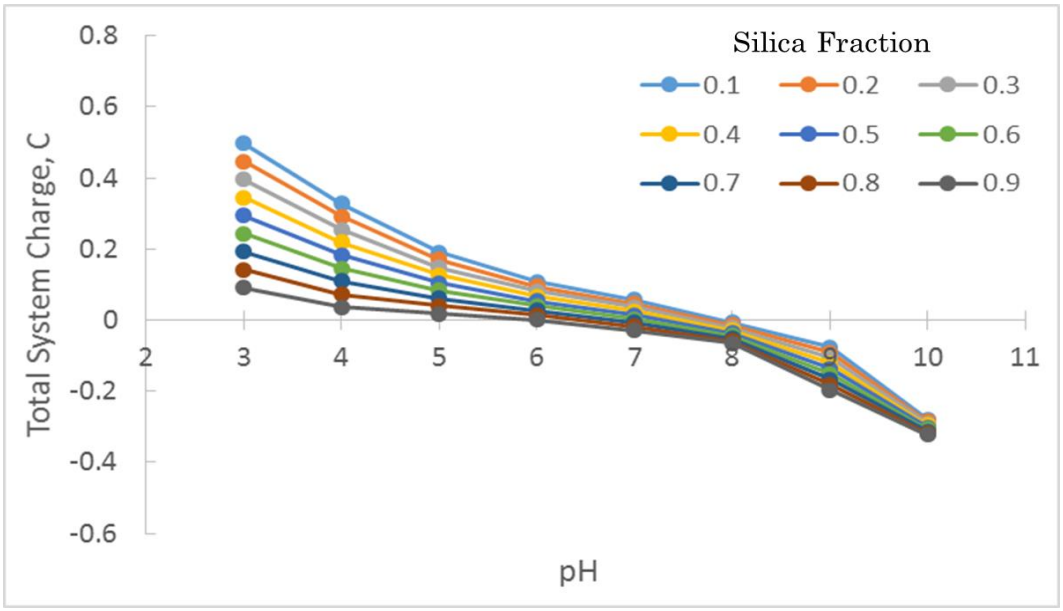


Figure 30. Total surface charge curves for Aerosil 200:Aeroxide AluC mixtures at various particle ratios and solution pHs.

window in both the experimental and calculated graphs (assumed to be the region where TSC is close to zero in the latter case) shifts to higher pHs as the silica fraction decreases, further affirming that this gelation mechanism is affected by the ratio of positive and negative surface charges in the mixture.

Experimental Phase Behavior

Si200/Alu C														
	1.75 vol% total													
	pH													
%Silica	1	2	3	4	5	6	7	8	9	10	11	12	13	14
100%	0	0	0	0	0	0	0	0	0	0	0	0	0	0
90%	0	0	0	X	X	X	X	0	0	0	0	0	0	0
80%	0	0	0	X	X	X	X	X	0	0	0	0	0	0
70%	0	0	0	X	X	X	X	X	0	0	0	0	0	0
60%	0	0	0	0	X	X	X	\	0	0	0	0	0	0
50%	0	0	0	0	X	X	X	X	X	0	0	0	0	0
40%	0	0	0	0	0	X	X	X	X	0	0	0	0	0
30%	0	0	0	0	0	0	X	X	X	\	0	0	0	0
20%	0	0	0	0	0	0	X	X	X	X	0	0	0	0
10%	0	0	0	0	0	0	X	X	X	X	0	0	0	0
0%	0	0	0	0	0	0	0	0	0	0	0	0	0	0

Calculated Total Surface Charge

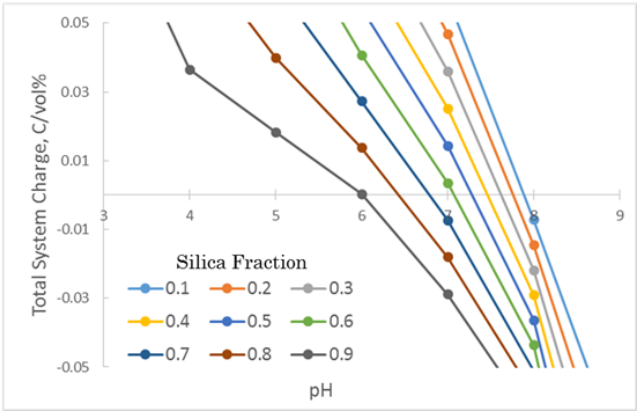


Figure 31. Comparison of experimentally determined phase behavior diagram for Aerosil 200:Aeroxide AluC gel mixtures and a magnified view of the TSC chart shown in Figure 30.